

Investigating brain-wide neural mechanisms using fMRI and novel tools

by

Sarah Jean Bricault

B.A. with honors, Biophysics

Swarthmore College

B.A., English Literature

Swarthmore College

Department of Biology
DOCTOR OF PHILOSOPHY

at the

Massachusetts Institute of Technology

© MIT 2020

February 2020

Signature of Author: **Signature redacted**

Department of Biology

January 24, 2020

Certified by: **Signature redacted**

Alan Jasanoff

Bioengineering Department

Brain and Cognitive Sciences

Nuclear Science and Engineering

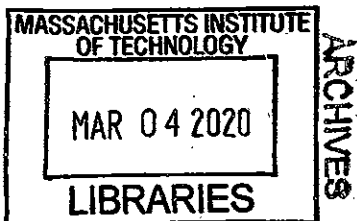
Thesis Supervisor

Accepted by: **Signature redacted**

Mary Gehring

Department of Biology

Graduate Committee Chair



Abstract

Defining the neural mechanisms that coordinate behavior requires characterizing the activity dynamics of diverse brain regions and neural circuit elements. My thesis explores such dynamics to help understand brain-wide processing of rewarding and aversive stimuli relevant to decision making. My primary experimental tool is functional magnetic resonance (fMRI), applied in anesthetized and awake rats, and I introduce methodologically significant innovations along with my scientific work. In the first part of my thesis, I investigate the neural bases of responses to intracranial rewarding and aversive stimuli. Comparison of psychometric and fMRI-based measurements identifies a putative site for reward integration in the nucleus accumbens (NAc), and targeted pharmacological inactivation of this region correspondingly distorts the evaluation of reward magnitudes in an operant task. My results dissociate processing of stimuli of opposite valence, by combining rewarding and aversive stimuli in a decision-making task and demonstrating that the two stimuli are processed independently. A limitation of these imaging studies is that they are performed in sedated animals. I therefore introduce a protocol for investigation of brain-wide neural dynamics in awake, paralyzed rats. I characterize intrinsic dynamics of brain function in this preparation, and argue that it constitutes a promising basis for further investigations of behaviorally relevant neural function. In the final part of my thesis, I describe a new tool for perturbation of brain dynamics using image-guided pharmacological interventions. The tool is a conjugate of the inhibitory drug muscimol to a paramagnetic contrast agent. I show that this reagent allows neurophysiological consequences of local inhibition to be characterized in spatial and temporal dimensions, creating a facile basis for assessing the contributions of drug-targeted structures. My work thus establishes a platform for hypothesis-driven investigation of distributed neural mechanisms involved in a broad range of contexts.

Acknowledgments

First and foremost, I want to thank my advisor, Professor Alan Jasanoff, for making this thesis possible. The Jasanoff lab is a wonderful place and I am honored to be a part of it.

I'd also like to thank Professor Troy Littleton, for always having time to speak with me about my science and my journey, and for guiding my work as a member of my thesis committee.

I give my thanks as well to Professors Matt Wilson and Nancy Kanwisher for being part of my thesis committee.

I owe a debt of gratitude to so many of my labmates, who have made graduate school an unforgettable experience. Thanks to Dr. Mitul Desai and Tehya Johnson for showing me the ropes when I joined lab and for their collaboration on the project described in Chapter 3. I also have Mitul to thank for introducing me to AFNI and for working with me on developing the prep described in Chapter 4. Thanks to Dr. Ali Barandov for his scientific advice and experimental assistance, especially in regards to the paper included as Chapter 5. Thanks to Dr. Benjamin Bartelle, Dr. Nan Li, Dr. Souparno Ghosh and Dr. Aviad Hai for their advice and feedback on my projects over the years. Thanks to Dr. Robert Ohlendorf and Jacob Simon for general advice as well as feedback on some of the text of this thesis. Thanks to Dr. Agata Wisniowska for her wonderful advice and friendship.

No page of acknowledgements would be complete without mention of the amazing undergrads who worked with me. Thanks to Jiyoung Lee, for being an amazing scientist and friend- your undergraduate thesis work was extraordinary. Thanks to Elizabeth DeTienne, for your friendship and all your hard work on Chapter 5 and elsewhere. Thanks to Cortni Dick, Hermoon Worku, and Jean Chow for your dedication to behavioral analysis, surgical techniques, and data analysis. Mentoring you all was one of my favorite parts of graduate school.

To my friends and family- thank you for bearing with me. For providing the kind of support that made it possible to face each new challenge. Not necessarily with a smile, but always with determination and the knowledge that you have my back, no matter what. For encouraging me, commiserating with me, advising me, consoling me, and most importantly loving me.

To my parents, Ray and Janet Bricault, I thank you for helping build the bedrock of my life. Your love and support from the beginning have meant everything to me, and if I stand tall today it's because you showed me how. To Nathan Bricault, I thank you for being not only a brother but also a cherished friend.

To Jean Dahlquist, for weathering the storms of undergrad by my side- and continuing to be a source of support and advice. To Span Spanbauer, for being my rock and for being a source of unlimited encouragement. To Chandra Kratzer, for being my friend in third grade- and every year since. To Alcor Hilliard, for including me in your stories and providing a much-needed creative outlet. To Krue Krueger, for hugs and for making our apartment an introvert nest. To Meghan Reedy, for all the advice and geeky company. To Lemur Rowlands, for so much friendship and support. To Ariel Segall, for helping me when things looked darkest.

Thank you all- I wouldn't have been able to do this without you.

Table of Contents

Chapter 1: Introduction	6
Characterizing brain-wide dynamics using fMRI	7
Towards an understanding of motivation and decision-related behaviors	11
Towards hypothesis-driven fMRI studies in awake animals	14
Summary	17
References	17
Chapter 2: Reward magnitude tracking by neurons in the ventral striatum	20
Abstract	21
Abbreviations	21
Keywords	21
Introduction	22
Methods	25
Results	38
Discussion	47
Author contributions	53
Acknowledgements	53
Figures	53
Supplementary material	62
References	75
Chapter 3: Dissociable processing of rewarding and aversive stimuli in rats	79
Abstract	81
Significance statement	81
Introduction	82
Materials and Methods	84
Results	92
Discussion	95
References	98
Figures	102
Chapter 4: Brain-wide functional imaging in awake rodents	107
Abstract	108
Introduction	109
Methods	110
Results and discussion	116
References	118
Figures	120
Chapter 5: Image-guided neural activity manipulation with a paramagnetic drug	121
Abstract	124
Introduction	124
Results	125
Discussion	128
Methods	129
Acknowledgements	138
References	138

Figures	140
Supplementary Figures	144
Supplementary Methods	148
Chapter 6: Summary and Future Directions	156
Summary	157
<i>Motivated behavior & decision making</i>	157
<i>Technique & tool development</i>	159
Future Directions	162
<i>Decision-making behavioral studies</i>	162
<i>Unanesthetized paralysis technique</i>	162
<i>Contrast agent conjugates</i>	163
<i>Towards real-time behavioral experiments during fMRI</i>	164

Chapter 1

Introduction

The contents of this chapter were written by Sarah Bricault with feedback from Alan Jasanoff.

Humans and other animals are constantly making decisions, and the study of decision-making is of fundamental importance to the field of neurobiology. In this thesis, I define the neural mechanisms that coordinate several such behaviors through the use of behavioral tests and functional magnetic resonance imaging (fMRI). Additionally, I describe two innovations that will facilitate similar studies in the future.

Characterizing brain-wide dynamics using fMRI

It is important to study behaviors using unbiased, whole-brain techniques. Many neurobiological techniques are spatially restricted and require that a hypothesis identify one or a small number of potentially relevant brain regions to examine. Although such techniques can indisputably provide valuable information, they also exhibit a limitation wherein they can only find results in the brain regions studied. It is essential to also employ techniques that are able to identify relevant brain regions over a wider area, or critical components of neural pathways may be overlooked.

A comparison of different high brain coverage techniques

There are a number of techniques that provide high coverage of the brain, and fMRI is the optimal choice for functional studies related to decision-making. Several other options include positron emission tomography (PET), electroencephalography (EEG), and magnetoencephalography (MEG). The best spatial and temporal resolution that can be achieved with each of these techniques is found in Table 1.

Technique	Best spatial resolution	Best temporal resolution
PET	~2.48 mm with oxygen (Moses, 2011)	~minutes (Kameyama et al., 2016)
fMRI	~1mm (Vu et al., 2017)	~0.5 seconds (Petrov et al., 2017)
MEG / EEG	~lobe of the brain (Kameyama et al., 2016)	~milliseconds (Kameyama et al., 2016)

Table 1: Best spatial and temporal resolution that can be achieved by several techniques that provide high coverage of the brain.

PET scans involve the delivery of a radioactive isotope, which gets incorporated into molecules involved in a process of interest, and decay of that isotope is measured (Heurling et al., 2017). PET has been increasingly used for functional, neurobiological applications in recent years. For example, there are PET tracers that target neurotransmitter receptors and transporters (Heurling et al., 2017). Although this molecular information is highly valuable, the need to wait for radioactive decay to see a result puts the maximum temporal resolution on the order of minutes (Kameyama et al., 2016). Notably, the neural processes underlying decision-making behaviors operate on the order of seconds or milliseconds.

EEG measures voltage fluctuations in the brain using electrodes, typically placed on the scalp. The number of sensors does affect the spatial resolution somewhat, with arrays of ~19 scalp electrodes being common and providing 6-9 cm spatial resolution in humans (Babiloni et al., 2001). Although a pure increase in the number of electrodes is insufficient to substantially improve the spatial resolution, mathematical and computational techniques in combination with larger sensor arrays can improve the spatial resolution to 2-3 cm (Babiloni et al., 2001). Notably, an entire rat brain is approximately 2.5 cm in length (Paxinos atlas), making EEG of limited utility in small animal studies. However, EEG is both the most affordable of the techniques discussed here and the least sensitive to subject motion (Gross, 2019).

MEG measures magnetic fields produced by electric currents in the brain and, like EEG, is measured from the scalp. The spatial resolution for MEG is in the centimeter range (Gross, 2019). Although MEG machines are not as expensive as MRI machines, they are still pricy and immobile, especially in comparison to EEG setups (Gross, 2019). Both EEG and MEG are only able to measure signals from brain regions near the surface, since that is where the measurements take place.

One final method for measuring brain activity in an unbiased fashion is fMRI, the technique that we chose to use to collect the data in this thesis, and one that provides both good spatial and acceptable temporal resolution, while also being completely noninvasive (Gross, 2019; Vu et al., 2017).

The most common method of measuring brain activity with fMRI is through measurement of the blood oxygen level dependent (BOLD) signal throughout the brain every few seconds. Although the exact relationship between the BOLD signal and neural activity is a topic of active investigation, the BOLD response is correlated with neural activity. In particular, local field potentials are predictive of the BOLD response (Logothetis et al, 2001).

The BOLD signal is derived from the fact that neurons use oxygen when they are active. The body responds by sending so much oxygen-laden blood into active regions of the brain that there is, in essence, an overcompensation that causes blood oxygenation levels to rise above baseline (Jezzard, Matthews, and Smith, 2001). Therefore, neural activity causes a time-delayed change in the BOLD signal. Although there is substantial research into coupling between the BOLD signal (which we can see using fMRI) and neural activity (which we can measure with techniques such as electrophysiology), this simple model is sufficient for our purposes here (Logothetis et al., 2001).

An overview of fMRI data analysis

In fMRI experiments, BOLD responses to a stimulus are analyzed. The stimulus can be active or passive. Active stimuli are mostly employed in non-human primate and human studies, and might include instructing the subject to perform a motor action (e.g. Nam and Kim, 2017). Passive stimuli, on the other hand, can be administered without requiring the explicit cooperation of the subject and are thus suitable for application in non-primate species. Such stimuli might include electrical stimulation of the forepaw of a rat (e.g. Bricault and Barandov et al., 2020) or visual stimulation of a mouse (e.g. Nahavandi et al., 2017). Typically, each voxel in the brain is examined for changes in the BOLD signal that occur several seconds after the application of the stimulus.

An example of a passive fMRI experiment is shown in Figure 1 (adapted from Bricault and Barandov et al., 2020 with permission). This is a forepaw stimulation experiment, where current is passed directly into a rat's forepaw, the left one in this case (Fig 1*a*). During forepaw stimulation, fMRI data is collected. Once preprocessed, the data can be displayed as shown in panels b and c. Panel c shows the percent signal change in all relevant voxels over time, with blue bars representing the stimulus application blocks. Note that the signal is clearly visible even in a single animal as shown here. One can also view this data as a map, where correlated and anti-correlated voxels are displayed as a color overlay and the grayscale coronal image of the rat brain forms the underlay (Fig 1*b*). Note that all responsive voxels are located within the forepaw region of the somatosensory cortex (S1FL), on the side of the brain opposite the stimulated forepaw.

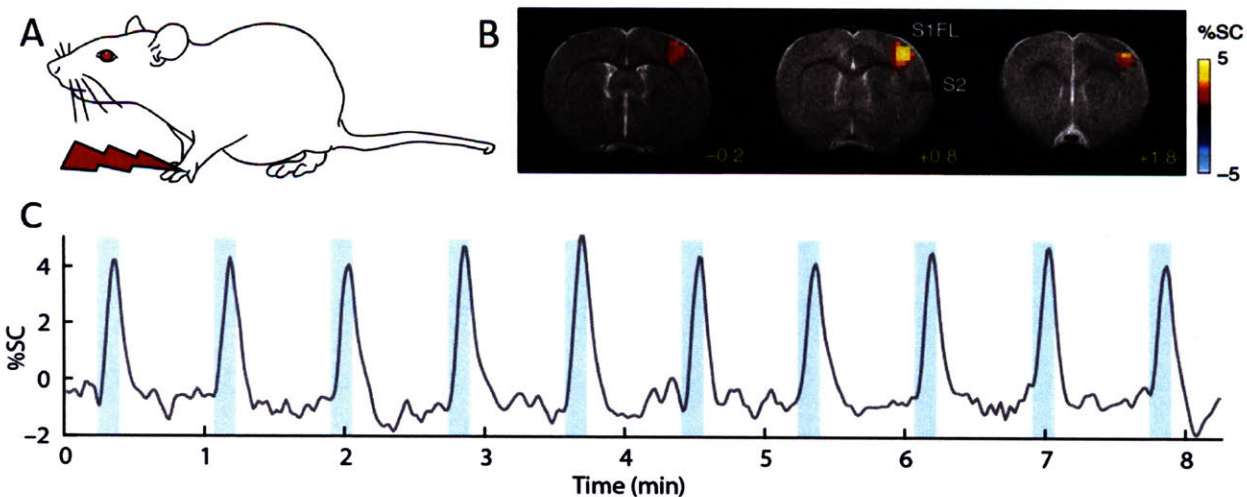


Figure 1: A typical task-based fMRI experiment in rats. (a) A rat is stimulated on the left forepaw using direct application of current. (b) A map of voxels whose activity is associated with the stimulus application ($n = 1$ rat). (c) The average timecourse from all voxels that showed activity correlating with the stimulus application. Blue bars denote stimulus application times. SC, signal change; S1, primary somatosensory cortex; S2, secondary somatosensory cortex; FL, forelimb.

fMRI is especially useful for studying neural pathways that are understood on a behavioral level. One can deliver behaviorally relevant stimuli and thereby gain insight into the neural circuitry that underlies aspects of the behavior (Fiallos et al., 2017).

Towards an understanding of motivation and decision-related behaviors

Motivation and decision-related behaviors can be readily studied in both humans and other animal species and, notably, many such study designs lend themselves well to fMRI experiments. For instance, the same stimuli that generate interesting behavioral responses (e.g. rewarding intracranial stimulation in rats) can be applied to subjects in the MRI scanner (Fiallos et al., 2017). This allows behavioral data to be correlated to whole-brain functional data, facilitating a deeper understanding of the underlying neural structures.

fMRI and reward processing

In canonical reward-seeking behavioral experiments, animals will perform an action or complete a task (such as pushing a lever) to receive a reward. A broad network of reward-related structures has been delineated that is involved in the processing of such behaviors. Perhaps the most notable of these are part of the mesolimbic dopamine system, which includes the ventral tegmental area (VTA), the nucleus accumbens (NAc), and the bundle of fibers that connects them known as the medial forebrain bundle (MFB) (Kandel and Mack, 2014). Furthermore, electrical stimulation of the MFB has been shown to mimic the effects of natural reward (Kandel and Mack, 2014).

Evaluation of the magnitudes of intrinsically rewarding stimuli is essential for assigning value and guiding behavior. For example, a rat faced with a choice between a small reward (e.g. low value food) and a large reward (e.g. high value food) will, in the absence of other factors, choose the large reward (Fiallos et al., 2017). However, in the case of intracranial stimulation of the MFB, this is only true up to a point. If the magnitude of the reward (i.e. frequency or amplitude of the stimulus) is sufficiently high, animals don't prefer rewards of even higher magnitudes (Fiallos et al., 2017; Gallistel and Leon, 1991).

In Chapter 2, we combine parametric manipulation of MFB microstimulation with fMRI in rats, and delineate a broad network of structures activated by behaviorally characterized levels of rewarding stimulation. We specifically looked for regions whose activity profile correlated with the subjective magnitude of the reward that was delivered behaviorally, as opposed to the objective value (i.e. frequency) of the stimulus. The largest and most reliable focus of reward magnitude tracking was observed in the shell region of the nucleus accumbens (NAc) (Fiallos et al., 2017).

Although the nonlinear nature of neurovascular coupling complicates interpretation of fMRI findings in precise neurophysiological terms, reward magnitude tracking was not observed in vascular compartments and could not be explained by saturation of region-specific hemodynamic responses. In addition, local pharmacological inactivation of NAc changed the profile of animals' responses to rewards of different magnitudes without altering mean reward response rates (Fiallos et al., 2017), further supporting a hypothesis that neural population activity in this region contributes to assessment of reward magnitudes.

fMRI and decision-making behavior

Deciding whether or not to perform an action depends both on the value of rewards associated with the action and also on potential costs. To model the interaction of rewarding and aversive stimuli associated with decision-making, we combined MFB stimulation with stimulation of the dorsolateral periaqueductal gray (dlPAG), a brain region that is an important component of the descending pain modulatory pathway.

Stimulation of the dlPAG is well known to be aversive. Rats will readily press a lever to terminate electrical or chemical stimulation of the dlPAG (Sander and Karli, 1987), and will actively avoid contexts which are associated with stimulation of the dlPAG (Zanoveli and Brandão, 2008; Roberts and Cox, 1987). Stimulation of the dlPAG at high levels induces a dramatic increase in stress hormone (corticosterone) levels in the blood (Lim et al., 2011), and the PAG is activated in response to threatening (Wendt et al., 2017), painful (Buhle et al., 2012), and negative emotional (Buhle et al., 2012) stimuli.

We used behavioral measures to compare the effects of MFB and dlPAG stimulation, delivered separately or together, on reward-seeking and on freezing. Surprisingly, the

experiments revealed that these rewarding and aversive stimuli had independent effects on the two behaviors (Chapter 3). Concurrent MFB stimulation did not affect dlPAG-induced active avoidance behaviors, and concurrent dlPAG stimulation did not affect MFB-driven reward-seeking behaviors (Chapter 3).

Towards hypothesis-driven fMRI studies in awake animals

A novel prep for fMRI data collection

When performing rodent fMRI, one common concern is how to best mimic the brain state of the awake, behaving animal. Recent advances have made minimal restraint awake fMRI possible in rodents (Chang et al., 2016), with one recent study successfully collecting fMRI data during a behavioral task in headfixed mice (Han et al., 2019). Despite these advances, however, it is largely infeasible to have an awake, behaving rodent voluntarily remain within the scanner. This is particularly true for rats, who can damage themselves or the experimental setup if not completely immobilized during imaging. Furthermore, the minute, involuntary movements of an otherwise stationary rodent are enough to create motion artifacts in fMRI data.

One common solution to this problem is to anesthetize and paralyze rodents during scanning procedures. Notably, this approach was used in the studies described above and in Chapters 2 and 3 of this thesis. This eliminates the problem of motion artifacts, but introduces questions about the relevance of the data. Perhaps unsurprisingly, it has been demonstrated that anesthesia has profound impacts on the BOLD signal (Paasonen et al., 2018). Some types of anesthesia are better than others in terms of the degree of impact, but the question of relevance remains.

An alternate solution is to image in an awake but physically restrained rodent. Typically, such rodents undergo many days of training so that they are acclimated to the restraints before the imaging occurs (Chang et al., 2016). However, motion artifacts remain a problem even in the most thoroughly restrained animals (see Chapter 4). Given that the animals are not visibly struggling, such artifacts are largely the result of minute muscle movements in the facial region, for example whicker twitching and blinking.

In Chapter 4, I present a solution to this problem. Here, I image animals that are unanesthetized but also paralyzed using pancuronium bromide. The applicability to the awake brain remains high, as the animals are not under the effects of anesthesia, and motion artifacts remain minimal since the animals are paralyzed. Furthermore, I demonstrate that following acclimation animals exhibit a stress hormone response that is no greater than that observed during physical restraint. This technique underlies many current experiments in the Jasanoff lab, and we hope that it will continue to facilitate imaging studies in our lab and others.

Development of a novel contrast agent for fMRI

One of the primary research aims of the Jasanoff lab and others is to develop novel contrast agents for fMRI. Some of these agents are designed to provide new functions, for example facilitating imaging of specific molecules. In one 2018 paper from the lab, Satoshi Okada et al. showed that it is possible to image endogenous calcium in the brain using a family of novel, magnetic nanoparticles termed MaCaReNas (Okada et al., 2018).

Other agents do not add new functionality per se, but rather tie the visualization capability inherent in contrast agents to useful molecules commonly used to perturb brain

function. In Chapter 5 of this thesis I demonstrate the development and validation of **paramagnetic muscimol (ParaMus)** (Bricault and Barandov et al., 2020).

One molecule commonly used to perturb brain function is muscimol. Muscimol is a reversible agonist for the γ -Aminobutyric acid (GABA) A receptor (Allen, 2008; Martin, 1991). When injected directly into brain tissue, it results in local inhibition and has been applied in a wide range of neurobiological studies.

Visualizing the spread of muscimol has remained a problem. Prior to 2008, it was necessary to euthanize animals and stain for the presence of the agonist before it was washed out of the tissue. 2008 saw the advent of fluorescent muscimol, which improved the situation but still requires euthanasia and brain sectioning to identify the spread of the agent (Allen, 2008). There are substantial drawbacks to this situation, including the requirement that the animal be euthanized and distortions to the tissue during sectioning preventing an accurate assessment of the spread of the agent. Two common failure modes associated with brain-sectioning-based visualization can be seen in Figure 2. Panel a shows a successful histological sample. In panel b, one can see a curving line anterior to the injection, indicating tissue distortion. In panel c, the staining was minimal. This could mean that the injection was unsuccessful, or it could mean that the fluorescent muscimol was not well fixed in the tissue during perfusion.



Figure 2: Difficulties in visualizing injected agents. Fluorescent muscimol (Allen, 2008) was injected into three rat brains. The animals were then euthanized, perfused, and their brains sectioned to view the spread of the agent. (a) A successful injection. (b) An injection displaying substantial warping of the tissue during sectioning. (c) An unsuccessful injection or one where the muscimol did not fix properly in the tissue.

By bonding the GABA-A agonist muscimol to the well-known T1 contrast agent gadolinium, we produced a GABA-A agonist whose injection profile can be observed in real-time during the acquisition of T1-weighted MRI images. Importantly, ParaMus retains the inactivating properties of muscimol as assessed using both *in vitro* and *in vivo* techniques. As with standard muscimol, ParaMus does wash out and is thus suitable for use in both rodent and monkey fMRI experiments.

In addition to serving as a useful tool in its own right, ParaMus can also serve as a template for future agents that combine pharmacological activity with MRI visibility.

Summary

In the following data chapters of this thesis, I will present my work on the topics described above. Chapters 2 and 3 contain behavioral and imaging data that provide insights into the processing of rewarding and aversive stimuli. Chapter 4 details a preparation we developed to facilitate the acquisition of high-quality fMRI data from unanesthetized animals. In Chapter 5, I discuss a novel tool we developed that allows for real-time visualization of reversible brain inactivation. Finally, in Chapter 6 I summarize the core findings, note major limitations of the studies discussed, and provide thoughts on avenues for future study.

References

Allen, Timothy A., et al. "Imaging the spread of reversible brain inactivations using fluorescent muscimol." *Journal of neuroscience methods* 171.1 (2008): 30-38.

- Babiloni, Fabio, et al. "Spatial enhancement of EEG data by surface Laplacian estimation: the use of magnetic resonance imaging-based head models." *Clinical Neurophysiology* (2001): 724-727.
- Bricault, Sarah and Ali Barandov et al. "Image-guided neural activity manipulation with a paramagnetic drug." *Nature Communications* 11.1 (2020): 1-6.
- Buhle, Jason T., et al. "Common representation of pain and negative emotion in the midbrain periaqueductal gray." *Social cognitive and affective neuroscience* 8.6 (2012): 609-616.
- Chang, Pei-Ching, et al. "Novel method for functional brain imaging in awake minimally restrained rats." *Journal of neurophysiology* 116.1 (2016): 61-80.
- Fiallos, Ana M. and Sarah Bricault et al. "Reward magnitude tracking by neural populations in ventral striatum." *NeuroImage* 146 (2017): 1003-1015.
- Gallistel, C. R., and Matthew Leon. "Measuring the subjective magnitude of brain stimulation reward by titration with rate of reward." *Behavioral neuroscience* 105.6 (1991): 913.
- Gross, Joachim. "Magnetoencephalography in Cognitive Neuroscience: A Primer." *Neuron* 104.2 (2019): 189-204.
- Han, Zhe, et al. "Awake and behaving mouse fMRI during Go/No-Go task." *Neuroimage* 188 (2019): 733-742.
- Heurling, Kerstin, et al. "Quantitative positron emission tomography in brain research." *Brain research* 1670 (2017): 220-234.
- Jezzard, Peter, Paul M. Matthews, and Stephen M. Smith, eds. *Functional MRI: an introduction to methods*. Vol. 61. Oxford: Oxford university press, 2001.
- Kameyama, Masashi, Koji Murakami, and Masahiro Jinzaki. "Comparison of [15O] H₂O positron emission tomography and functional magnetic resonance imaging in activation studies." *World journal of nuclear medicine* 15.1 (2016): 3.
- Kandel, Eric R., and Sarah Mack. *Principles of Neural Science*. McGraw-Hill Medical, 2014.
- Lim, Lee Wei, et al. "Increased plasma corticosterone levels after periaqueductal gray stimulation-induced escape reaction or panic attacks in rats." *Behavioural brain research* 218.2 (2011): 301-307.
- Logothetis, Nikos K., et al. "Neurophysiological investigation of the basis of the fMRI signal." *Nature* 412.6843 (2001): 150.

- Martin, John H. "Autoradiographic estimation of the extent of reversible inactivation produced by microinjection of lidocaine and muscimol in the rat." *Neuroscience letters* 127.2 (1991): 160-164.
- Moses, William W. "Fundamental limits of spatial resolution in PET." *Nuclear Instruments and Methods in Physics Research Section A: Accelerators, Spectrometers, Detectors and Associated Equipment* 648 (2011): S236-S240.
- Nahavandi, Payam, et al. "fMRI of Visual Stimuli in a Tau Model of Alzheimer's Disease." *Alzheimer's & Dementia: The Journal of the Alzheimer's Association* 13.7 (2017): P142.
- Nam, Seungkyu, and Dae-Shik Kim. "Reconstruction of Arm Movement Directions from Human Motor Cortex Using fMRI." *Frontiers in neuroscience* 11 (2017): 434.
- Okada, Satoshi, et al. "Calcium-dependent molecular fMRI using a magnetic nanosensor." *Nature nanotechnology* 13.6 (2018): 473.
- Paasonen, Jaakko, et al. "Functional connectivity under six anesthesia protocols and the awake condition in rat brain." *Neuroimage* 172 (2018): 9-20.
- Petrov, Andrii Y., Michael Herbst, and V. Andrew Stenger. "Improving temporal resolution in fMRI using a 3D spiral acquisition and low rank plus sparse (L+ S) reconstruction." *NeuroImage* 157 (2017): 660-674.
- Roberts, Vicki J., and Verne C. Cox. "Active avoidance conditioning with dorsal central gray stimulation in a place preference paradigm." *Psychobiology* 15.2 (1987): 167-170.
- Sandner, G., P. Schmitt, and P. Karli. "Mapping of jumping, rearing, squealing and switch-off behaviors elicited by periaqueductal gray stimulation in the rat." *Physiology & behavior* 39.3 (1987): 333-339.
- Vu, An T., et al. "Tradeoffs in pushing the spatial resolution of fMRI for the 7T Human Connectome Project." *Neuroimage* 154 (2017): 23-32.
- Wendt, Julia, et al. "Active avoidance and attentive freezing in the face of approaching threat." *NeuroImage* 158 (2017): 196-204.
- Zanoveli, Janaina M., and Marcus L. Brandão. "The dorsal periaqueductal and basolateral amygdala are necessary for the expression of conditioned place avoidance induced by semicarbazide stimulation of the dorsal periaqueductal region." *Progress in Neuro-Psychopharmacology and Biological Psychiatry* 32.7 (2008): 1715-1721.

Chapter 2

Reward magnitude tracking by neurons in the ventral striatum

The contents of this chapter were taken from the 2017 NeuroImage paper of the same name. The text was written by Ana Fiallos and Alan Jasanoff. My contribution to this paper was the collection and analysis of the imaging and behavioral data presented in Figures 6, S11, and S12.

Fiallos, Ana M., et al. "Reward magnitude tracking by neural populations in ventral striatum." *NeuroImage* 146 (2017): 1003-1015.

Abstract

Evaluation of the magnitudes of intrinsically rewarding stimuli is essential for assigning value and guiding behavior. By combining parametric manipulation of a primary reward, medial forebrain bundle (MFB) microstimulation, with functional magnetic imaging (fMRI) in rodents, we delineated a broad network of structures activated by behaviorally characterized levels of rewarding stimulation. Correlation of psychometric behavioral measurements with fMRI response magnitudes revealed regions whose activity corresponded closely to the subjective magnitude of rewards. The largest and most reliable focus of reward magnitude tracking was observed in the shell region of the nucleus accumbens (NAc). Although the nonlinear nature of neurovascular coupling complicates interpretation of fMRI findings in precise neurophysiological terms, reward magnitude tracking was not observed in vascular compartments and could not be explained by saturation of region-specific hemodynamic responses. In addition, local pharmacological inactivation of NAc changed the profile of animals' responses to rewards of different magnitudes without altering mean reward response rates, further supporting a hypothesis that neural population activity in this region contributes to assessment of reward magnitudes.

Abbreviations

Amyg, amygdala; AmygAM, anteromedial amygdala; AmygPL, posterolateral amygdala; BOLD, blood oxygenation-level dependent; CPu, caudate-putamen; CgCx, cingulate cortex; DpMe, deep mesencephalic nuclei; DTI, diffusion tensor imaging; fMRI, functional magnetic resonance imaging; EPI, echo planar imaging; GLM, general linear model; GP, globus pallidus; Hippo, hippocampus; LH, lateral hypothalamus; LS, lateral septal nucleus; MFB, medial forebrain bundle; NAc, nucleus accumbens; NAcC, nucleus accumbens core; NAcS, nucleus accumbens shell; Tu, olfactory tubercle; OCx, orbital cortex; PiCx, piriform cortex; PO, preoptic area; ROI, region of interest; SCx, somatosensory cortex; SI, substantia innominate; SN, substantia nigra; Thal, thalamus; VP, ventral pallidum; vSub, ventral subiculum; VTA, ventral tegmental area

Keywords

Reward; BOLD fMRI; Microstimulation; Nucleus accumbens

Introduction

Animals enact behavioral strategies largely based on the amount of positive reinforcement or reward they expect to receive from competing courses of action (Doya, 2008, Kringelbach and Berridge, 2009). Rewards come to be associated with actions, as well as with environmental stimuli, and give rise to their perceived values. Associations are learned and values adjusted by comparing earned and expected rewards in each behavioral context (Sutton and Barto, 1981). When choosing from a set of options, animals will often allocate their decisions in direct proportion to the reward magnitude associated with each option; two equally rewarding options will be chosen with equal probability, and more rewarding options will be chosen more frequently (Herrnstein, 1970). A requirement in most types of reward-related behavior is therefore that animals have a way to assess rewards in at least semi-quantitative fashion. Most fundamentally, animals must be able to evaluate the magnitudes of intrinsically rewarding stimuli (primary rewards) in much the same way they evaluate sensory variables such as luminance, texture, and tone.

Neurons with firing rates dependent on reward magnitudes have been identified in the prefrontal cortex, striatum, amygdala, and dopaminergic midbrain (Schultz, 2015). Some of these neurons fire in absolute proportion to reward magnitude, immediately after delivery, but most have more complex dependence on behavioral variables, including the range of reward magnitudes presented in a task and the presence of stimuli predictive of rewards (Schultz, 2000). Dopaminergic fibers that project to the nucleus accumbens (NAc) have often been considered essential to reward processing, and are among those that signal when rewards are anticipated as well as experienced (Saddoris et al., 2015). The functional relationships among reward-responsive neurons in different brain regions and their relationship to broader neuronal networks

remain a topic of intense interest. Because studies of reward are typically performed using electrophysiology or electrochemistry in awake, behaving animals, it is hard to isolate low-level neuronal events involved in integrating rewarding stimulus inputs from higher-level processes that presumably relate reward magnitudes to other stimuli or task components; it is also difficult to compare different brain regions or cell populations to assemble a comprehensive picture of neural tuning to rewards, analogous to maps of functional architecture obtained in sensory systems.

Neural stimulation methods permit the dissociation of reward delivery from other aspects of behavior, and could be particularly useful in defining mechanisms of reward magnitude computation. A robust, clinically-relevant, and empirically well-characterized technique involves electrical microstimulation of various brain regions, most prominently including the medial forebrain bundle (MFB) (Olds and Milner, 1954). The trade-off between the stimulation strength and duration of pulse trains required to support any given level of operant responding for MFB stimulation has led to the suggestion that action potentials triggered by the stimulation are summed by a neural integrator closely associated with the animal's assessment of reward magnitude and consequent behavioral performance (Gallistel, 1978, Gallistel et al., 1981, Somnenschein et al., 2003). Importantly, MFB stimulation-mediated reward has been shown to substitute for sucrose solutions in behavioral tasks (Conover and Shizgal, 1994), implying that the circuitry activated by MFB stimulation coincides in functionally relevant ways with the neural pathways required for processing naturalistic rewards. Unlike many naturalistic rewards, however, MFB stimulation reward is easily combined with high resolution noninvasive brain imaging, and has been used by ourselves and others in recent MRI studies (Krautwald et al., 2013, Lee et al., 2014).

In an effort to discern essential components of reward magnitude processing at a whole-brain level, we combined MFB stimulation reward with behavioral psychophysics, local pharmacological inactivation, and functional magnetic resonance imaging (fMRI) in rats. This combined approach allowed us to manipulate the reward system and record quantitative neurophysiological information from distributed neural populations. We were able to survey the entire brain for foci of reward magnitude tracking—areas whose fMRI signals track psychometric reward magnitude measurements—which could then be probed with targeted brain inactivation to test whether spatially-distinct neural populations play a role in reward magnitude integration.

Methods

Implantation of stimulation electrodes and cannulae

All surgical and animal handling procedures were performed in accordance with federal and institutional guidelines, and were approved by the MIT Committee on Animal Care. Adult male Lewis rats (250–300 g) were implanted with stimulation electrodes in the medial forebrain bundle (MFB) at the level of the lateral hypothalamus (LH). Monopolar stimulating electrodes were fabricated from 0.063 mm-diameter teflon-coated silver wire (A-M Systems, Sequim, WA), cut to lengths of approximately one centimeter. These electrodes were comparable to monopolar electrodes used in previous MFB stimulation studies most relevant to our experiments, and the use of silver wire, compared with alternative materials, minimized the MRI artifact associated with magnetic susceptibility of the electrode. Approximately 0.5 mm of the insulation was stripped from one end of each electrode to form a tip. The length of the wire (63.5 mm) was threaded through 0.762/1.587 mm inner/outer (ID/OD) diameter polyetheretherketone (PEEK) tubing (McMaster-Carr, Robbinsville, NJ) and connected to one pin of a two-pin connector (Digi-Key, Thief River Falls, MN). The second pin was connected to a bare silver reference wire of 63.5 mm length and 0.125 mm diameter.

Animals were anesthetized and underwent surgery to introduce craniotomies for electrode insertion, 2.2 mm, 2.0 mm or 1.2 mm posterior to bregma and 1.7 mm left of the midline suture. Electrodes were lowered through the craniotomy to a depth of 8.6 mm below the skull surface. An additional hole was drilled through the skull for introduction of a conducting, beryllium copper screw (Antrin Enterprises, Ojai, CA); the stimulating electrode ground wire was wound around this screw and attached with silver paint. Some animals were further implanted with a 2.0 or 7.5 mm long 22 GA PEEK guide cannula (Plastics One, Roanoke, VA) for the infusion of

lidocaine into NAc. Guide cannulae were fitted with a Nylon dummy cap with a stylet that protruded 0.5 mm beyond the end of the guide to prevent blockage of the cannulae. A custom-made polyetherimide head post, tapped to accept two nylon screws from the MRI coil mounting head gear, was cemented to the dorsal surface of the skull anterior to the stimulating electrode for animals undergoing fMRI. Dental cement was applied to the entire skull surface area to hold the implants rigidly in place. Electrode and cannula positions were confirmed using MRI data and histologically confirmed in a subset of rats. For several animals, electrode impedances were measured before each behavioral session using an FHC Impedance Conditioning Module (FHC Inc., Bowdoin, ME); all measured animals displayed stable electrode impedances in the range from 4.9–6.6 k Ω .

Behavioral techniques

Electrode-implanted animals underwent behavioral shaping and measurement procedures. All behavioral experiments were performed in a plexiglass operant chamber (28×21×21 cm; Lafayette Instruments, Lafayette, IN), placed in a lighted sound-proof cabinet (Med Associates, St. Albans, VT). Two infrared nose poke sensors (Med Associates) were positioned at one end of the operant chamber, 5 cm from the floor, and a light emitting diode (LED) indicator was positioned near the top of the chamber above the sensors. Input from the nose poke sensors was monitored by a laptop computer via a digital input/output interface (National Instruments, Austin, TX). A custom-written computer program was used to time output stimuli dependent on the detected nose pokes. Output pulses from the computer were used to trigger cathodal stimulus pulses (0.2 ms) delivered at frequencies from 44–386 Hz by a constant current isolated stimulator (World Precision Instruments Isostim A320R, Sarasota, FL). The applied frequencies are in the standard range used to evoke MFB stimulation reward-related behavioral effects in

animals, and are also comparable to clinically relevant deep brain electrical stimulation frequencies, which are typically delivered at over 100 Hz. Poles of the stimulator were shorted to one another in between stimulus pulses to prevent charge buildup on the electrodes, and pulses were visualized on an oscilloscope to verify consistent amplitude and pulse shape.

Animals were initially shaped to perform nose pokes to elicit MFB stimulation. In a typical experiment, an animal was rewarded for each nose poke with a one second 150 Hz train of 0.2 ms pulses, delivered at the maximum stimulus current (0.3–0.9 mA) for which no overt motor artifact was observed. The minimum interstimulus interval was 0.5 s. Shaping sessions lasted 30 min to one hour, once per day, for 2–10 days. Animals that displayed fewer than ~20 nose pokes per minute were eliminated from the study. Following shaping, psychometric “reward titration” curves were measured using a two choice operant task. The experimental procedure was based on studies of Gallistel and others (Gallistel and Leon, 1991, Mark and Gallistel, 1993, Simmons and Gallistel, 1994), who have shown that rats prefer rewarding stimuli of increasing intensity, up to a saturation point beyond which more intense stimulation is indistinguishable from the saturating reward.

Rats destined for imaging experiments were placed in an operant chamber with two nose poke sensors, and their behavior was monitored over a series of five-minute trials. Triggering of either sensor during a trial elicited a 1 s pulse train (0.2 ms pulses) of MFB stimulation, delivered with currents determined as described above and minimum inter-train interval of 0.5 s. Poking into one sensor elicited stimulation at a fixed “reference” frequency of 150 Hz, found to be above the saturation frequency for all eight individuals included in our initial reward titration analysis. Poking into the other sensor elicited stimulation at a second, varied “comparison” frequency. The comparison stimulus was delivered at 44, 53, 64, 77, 93, 111, 134, 161, 193, or

231 Hz. For all animals, at the start of each behavioral session, a dummy trial was conducted to reshape animals to the task. Then ten trials were performed, in each of which an animal compared one of the 10 comparison stimuli to the fixed reference stimulus. Trials using the ten different comparison frequencies were performed in random order to eliminate the potential for systematic frequency-dependent performance changes over the duration of the session. To encourage exploration of both nose poke holes, the mapping between the two nose poke sensors and associated stimulation frequencies was reversed electronically in mid-trial. The initial assignment of the two frequencies to the two sensors was also randomized among the trials. Trials were separated by 30 s inter-trial intervals and the LED indicator in the operant box was on during, but not in between the trials.

In house software controlled task variables and kept track of the rats' choices and the number of rewards earned at reference and comparison frequencies during the sequence of trials. Reward titration curves were computed as the fraction of rewards harvested at the comparison frequency, as a function of the comparison frequency setting. Median filtering over a moving window of three consecutive frequencies was performed to remove outliers. Rats were required to generate an asymptotic titration curve on at least two sessions for inclusion in the data set, and to progress to the fMRI phase of the experiment. With the range of stimulus currents used, the titration curves typically saturated in a narrow range of frequencies near 137 Hz. Behavioral data processing was performed using Excel (Microsoft Corp, Redmond WA) and Matlab (Mathworks, Natick, MA); error bars denote the standard error of the mean across multiple measurements from individual animals or across multiple animals.

Magnetic resonance imaging

Animals that performed the task effectively (>20 responses per minute; n=10) were anesthetized with isoflurane and tracheotomized in preparation for functional magnetic resonance imaging (fMRI). Luer-fitted teflon endotracheal tubes (14 gage; McMaster-Carr, Santa Fe Springs, CA) were surgically inserted and fixed in place with dental floss (Walgreens, Cambridge, MA) and Vetbond (3M, St. Paul, MN). Ear canals were filled with toothpaste to avoid magnetic susceptibility-induced distortions in the images. Tracheotomized animals were paralyzed by intraperitoneal injection of a 1 mg/kg bolus of pancuronium bromide (Sigma-Aldrich, St. Louis, MO), followed by continuous 1 mg/kg/hr infusion throughout the course of subsequent experiments. Mechanical ventilation was performed using an Inspira ventilator from Harvard Apparatus (Holliston, MA), operated at 70 beats per minute and 5 mL per stroke. Heart rate and blood oxygenation were continuously monitored using an MRI-compatible noninvasive infrared sensor and pulse oximeter (Nonin Medical, Plymouth, MN), and isoflurane anesthetic concentration was initialized to 1% and adjusted within the range from 1.00% to 1.25% to keep physiological parameters within 10% of baseline values. Animals were wrapped in a heated circulating water blanket (Gaymar, Orchard Park, NY), and core body temperature was monitored by means of a rectal thermometer. They were then transferred to a positioning device (Ekam Imaging, Shrewsbury, MA) and inserted into an MRI scanner for imaging.

MRI scans were obtained using a 4.7 T 40 cm horizontal-bore magnet interfaced to a Bruker (Billerica, MA) Avance console and equipped with a 12 cm gradient set (26 G/cm). A transmit-only 10 cm inner diameter volume coil and a customized ~2 cm diameter receive-only surface coil (Ekam Imaging), both integrated into the animal positioning device, were used for excitation and detection. Pulse sequences were controlled through the Paravision 3.0 software (Bruker). For functional imaging with blood oxygenation level dependent (BOLD) contrast, a

single-shot gradient echo planar imaging (EPI) pulse sequence was used with an echo time (TE) of 20 ms, recycle time (TR) of 2 s, slice thickness of 1 mm (14–16 slices centered over bregma), in-plane field of view 3.2×2.4 cm, and matrix size 64×48 points. Standard gradient echo BOLD was chosen because of its relative sensitivity compared with cerebral blood flow or spin echo-based measurement methods (Norris, 2012). High resolution anatomical images including electrode and cannula implantation sites were acquired using a conventional gradient echo pulse sequence with TE/TR=15/2000 ms, slice thickness 1 mm, 3×3 cm FOV, and 256×256 matrix size. Diffusion tensor imaging (DTI) was performed after fMRI using a pulsed gradient spin echo sequence with EPI readout parameters matching those used for BOLD data acquisition. Data were obtained with 16-fold averaging and diffusion weighting parameter $b=0$ and 1000 s/mm²; 15 gradient directions were applied. The pulsed gradient duration and diffusion time were 5 and 15 ms, respectively. An angiography dataset was acquired with a time-of-flight angiography pulse sequence with TE/TR of 5/30 ms.

Functional imaging experiments were performed in conjunction with MFB stimulation. Stimulating electrodes were connected to a constant current stimulator (World Precision Instruments) located outside of the scanner. Stimulation currents, pulse widths, and frequencies were individually matched for each animal to those used for behavioral experiments performed prior to imaging, and cable lengths were the same for imaging and behavior. To minimize potential radiofrequency artifacts, the stimulator cable was filtered with a 1.9 MHz low-pass filter (Mini-Circuits BLP-1.9, Brooklyn, NY) before entering the MRI enclosure. Stimulus pulses were monitored continuously on an oscilloscope (Tektronix TDS-210, Beaverton, OR) to verify consistency throughout scanning experiments. During fMRI data acquisition, stimuli were delivered in 40 s blocks of eight equally-spaced one-second long trains pulse trains, each at a

specified frequency, separated by blocks of 60 s without stimulation. MFB stimuli of different frequency (10 frequencies) were delivered in pseudorandom order, and each sequence of stimuli was repeated three times for a total of 30 blocks of stimulation per fMRI experiment.

The average heart rate during imaging sessions was 428.7 beats per minute (bpm) with a standard deviation of 36.6 bpm. Heart rates were stable over the duration of each imaging experiment, with drift between start and end of a session ranging from -3.6% to 6.7% , and an average stimulus-induced change of 1.1% . Average heart rate changes to each stimulation frequency are shown in Supplementary Fig. S1, and remained under 2% in all cases. These stimulus-induced heart rate changes were small compared with changes of up to 5% reported in response to commonly used forepaw stimulation methods in rats (Liu et al., 2004) or changes of over 15% in human resting state studies (Chang et al., 2009, Shmueli et al., 2007).

Data analysis

Raw MRI data from all experiments were initially preprocessed using custom routines running in Matlab (Mathworks). All data were Fourier transformed with a spatial smoothing kernel of 1.5 voxels full-width at half maximum. EPI data were ghost-corrected using a published algorithm implemented in Matlab (Buonocore and Gao, 1997). Fractional anisotropy and directionality maps were computed from transformed DTI data using routines from the Matlab suite BEAR (University of Paris, France). Segmentation of brain from non-brain voxels was also performed in Matlab. Further preprocessing of functional imaging data was accomplished using the AFNI software package (National Institute of Mental Health, Bethesda, MD). Steps included slice timing correction, motion correction using a least squares rigid-body volume registration algorithm, voxel-wise intensity normalization, and segmentation of brain from non-brain voxels.

After motion correction, fMRI time series data from individual animals were coregistered onto a reference data set using a least squares affine alignment of fractional anisotropy maps (Supplementary Fig. S2a). Alignment of rodent fMRI datasets is more conventionally performed by registering each animal's echo planar images to anatomical scans, and then registering between animals using the anatomical data. These are “information poor” procedures, since standard T1 and T2-weighted imaging do not offer many landmarks for coregistration in rodent brains. Use of the DTI maps for alignment guaranteed that spatial features throughout the brain were available to guide the registration. Because the DTI data were acquired using the same EPI readout parameters as the functional scans, DTI-based alignment also eliminated the need for within-animal alignment of functional with anatomical scans. Further, because subsequent region of interest (ROI)-based analyses were performed using regions defined by comparison of DTI and histological data, coregistration based on DTI guaranteed that the correspondence between individual animals' EPI time series and anatomical regions remained relatively constant from animal to animal. Visual inspection of aligned fractional anisotropy data from multiple animals confirmed that individual features were effectively coregistered by our procedure. Time series data were smoothed with a Gaussian spatial kernel of 1 mm full width at half-maximum prior to statistical analysis.

Statistical analysis of preprocessed EPI time courses was performed using the general linear modeling (GLM) approach, implemented in AFNI (Cox, 1996). Regression vectors for calculation of activation maps were computed by convolving MFB stimulus times with a hemodynamic response model consisting of a single gamma function with Cohen parameters $b=6$ and $c=0.8$. Six motion correction parameters from each animal were included as nuisance regressors, along with a linear baseline term. Outlier scans detected by median deviation from

time series trends in each data set were censored from the analysis. Stimulation frequency-independent average responses were determined by using a single regressor to model MFB stimulation at all delivered frequencies. Frequency-dependent responses were determined in a separate calculation, by using individual regressors for each stimulation frequency.

Response amplitudes (regression coefficients) determined for each voxel by the GLM analyses were used as input for further numerical analyses performed in Matlab. These included computation of ROI-averaged responses and correlation of fMRI responses with behavioral data. For ROI analyses, anatomically-defined regions were delineated by comparing DTI fractional anisotropy data and high-resolution anatomical scans with a standard brain atlas. Distinct landmarks recognizable by diffusion anisotropy, including fiber tracts such as the corpus callosum, anterior commissure, internal capsule, and cerebral peduncle, were used to relate an average of the coregistered DTI scans to individual images from a standard brain atlas (Paxinos and Watson, 1998). After assigning each DTI slice to the corresponding Horsley-Clarke A-P plane, atlas images were imported into Matlab and appropriately scaled to match the DTI images and high-resolution anatomical scans. ROIs were manually drawn over the DTI images, again making use of landmarks visible in each slice in either the DTI or anatomical image (Supplementary Fig. S2b). ROI names correspond to standard usage (Paxinos and Watson, 1998) in most cases, with the following additional notes: AmygAM and AmygPL include anteromedial and posterolateral amygdalar regions, respectively; CgCx includes cingulate cortex and adjacent limbic cortical regions; DpMe is broadly defined to include reticular and tegmental structures dorsal to VTA and SN and ventral to superior colliculus; Hippo includes standard divisions of the hippocampus; NAcC and NAcS correspond to core and shell regions of NAc; OCx includes ventral and lateral orbital cortex, plus immediately adjacent anterior insular cortical regions; Thal

denotes the thalamus, without subdivisions; vSub includes ventral subiculum plus adjacent parasubicular and presubicular regions; VTA includes parabrachial, parainterfacial, and paranigral nuclei of the ventral tegmentum. The number of EPI voxels in each defined ROI is presented in Supplementary Table S1.

ROIs and statistical maps included all voxels in unbiased fashion, excepting areas identified as dominated by BOLD signals from large draining veins or signal drop out from electrode or cannula implants (Supplementary Fig. S3). The macrovascular compartments were taken to comprise areas that displayed strongly hysteretic responses to MFB stimulation (Lee et al., 1995). These were defined by comparing the amplitude for the final two stimulus trains and the initial two stimulation trains in each 8-train (40 s) stimulation block, as computed from a group of 10 animals. Voxels that showed 0.4% or greater average response to the last two stimulus trains vs. the first two were defined as predominantly macrovascular, and were excluded from statistical calculations and ROI averages. The voxel counts for each ROI in Supplementary Table S1 reflect this exclusion. For tests of the dependence of vascular ROI results on the precise definition of vascular regions, alternative vascular ROIs were delineated by thresholding a T1-weighted angiography image, or by smoothing a map of internal edges detected using the Sobel method, implemented in Matlab with stringency parameters 10–25, applied to T2*-weighted anatomical maps (Supplementary Fig. S4). The first alternative approach proved most sensitive to major arteries, while the second method overlapped heavily with the hysteresis detection method, and was probably most sensitive to larger veins.

Unless otherwise noted throughout the paper, error bars reported for fMRI data denote the standard error of the mean values observed across multiple animals. Error estimates for ROI-averaged fMRI response amplitudes and stimulation frequency-dependent profiles were

computed using jackknife resampling of the fMRI data from multiple animals, in conjunction with GLM analyses of the resampled group data. These analysis methods were implemented in AFNI and Matlab.

Assessment of reward tracking vs. frequency tracking by fMRI signals was performed by fitting voxel or ROI-averaged BOLD amplitudes at each MFB stimulation frequency to a GLM including a constant term and two regressors (Fig. 3a), one rising linearly from 0 to 1 in proportion to stimulation frequency (frequency tracking), and the other rising from 0 to 1 over the interval from 0 to 135 Hz and then remaining flat for frequencies over 135 Hz (reward tracking). The reward tracking regressor represents an idealized form of the reward titration curve of Fig. 2b, in which the rewarding value of a stimulus is assumed to be proportional to stimulation frequency up to the saturation point. All stimulation frequency-dependent data were smoothed by averaging over a moving window of three frequencies prior to GLM analysis or presentation in the figure panels. End points were not modified. Beta coefficients for the two regressors (i.e. estimated contributions of frequency and reward tracking models to the signal) were used to generate the red/green color coding of Fig. 3 or combined into the saturation index= $\beta R/(\beta R+\beta F)$ of Fig. 4a, where βR and βF are the reward and frequency tracking coefficients, respectively.

Amperometric measurement of dopamine

Four rats were implanted with stimulation electrodes, shaped to perform operant responses, and trained for 3–5 days according to methods described above. Prior to amperometry, animals were anesthetized with 2% isoflurane, warmed on a heating pad and placed in a stereotax. A carbon fiber recording electrode was implanted in NAc, 1.6 mm anterior to bregma, 1.5 mm left of midline and 8.4 mm below the skull surface. An Ag/AgCl

reference electrode was implanted at identical coordinates contralateral to the carbon fiber electrode. The recording and reference electrode were connected to a Picostat and e-Corder system (eDAQ Inc., Colorado Springs, CO), which applied a fixed potential of 0.8 V to the recording electrode and continuously monitored the oxidation current with 10 kHz sampling. Once a stable baseline was achieved, MFB stimulation was delivered as above in blocks of eight 1 s pulse trains (0.2 ms pulse width), with 4 s inter-train interval and 60 s separation between stimulation blocks. Stimuli were applied with pulse frequencies of 44–231 (n=1) or 44–400 Hz (n=3), delivered twice each in pseudo-random order. The paradigm was repeated with a control applied potential of 0.1 V to verify specificity of the measurements to the oxidation potential of dopamine. Following recording, carbon fiber electrodes were calibrated in a custom-made flow cell, using dopamine concentrations of 0–10 μM in the presence of 600 μM ascorbic acid. Calibration constants of 0.6 ± 0.2 nA/ μM dopamine (mean \pm s.d.) were obtained.

Targeted pharmacological inactivation

Six rats were implanted with monopolar electrodes in the MFB and cannulas over the ipsilateral NAc. The surgical procedures and coordinates were the same as those described above. The rats were then trained to perform reward-seeking behavior also as described above, except that the number of comparison frequencies was reduced to four (50, 90, 150, and 202 Hz) to limit the length of the experiment and thus the total infusion volume. The day after the rats achieved a stable titration curve the inactivation experiment was performed. Rats were first anesthetized with 1% isoflurane to facilitate the placement of an internal cannula into the NAc. Injection cannulae were inserted into NAc through the preimplanted guide cannulae, such that the injection tip position was -1.7 mm anterior and 0.8 mm lateral to bregma and 7.5 mm below the skull. Cannulae were then fixed in place with dental cement to prevent dislodgement during

the behavioral task. Animals were allowed to recover in the behavioral box, and infusion began once they started to move around. The first (dummy) trial commenced five minutes later, followed by the four test trials delivered in pseudo-random order. All trials were five minutes long. Infusion of 2% lidocaine continued throughout the experiment at a rate of 0.1 $\mu\text{L}/\text{min}$. The total infusion volume thus ranged from 1 μL (at the start of trial 1) to 3 μL (at the end of trial 4). This continuous infusion model was utilized to prevent any lidocaine washout during the experiment. The next day the normal behavioral task was repeated to verify that any observed results were not the result of cannula placement or tissue damage from the infusion. These procedures were also applied to an additional five rats with infusion cannulae implanted over ipsilateral VTA rather than NAcS. In each case, the electrode and cannula placements were verified for each animal with anatomical MRI scans on a 7T Bruker system.

Results

MFB stimulation activates mesolimbic and nigrostriatal pathways

We first used fMRI to study the spread of MFB stimulation-evoked activity from the electrode site in behaviorally characterized rats. Rats were chronically implanted with stimulating electrodes in the MFB at the level of the lateral hypothalamus (LH), and were trained in an operant task to perform nose-pokes in response to rewarding stimuli of varying frequency (44–231 Hz). Animals that performed the task effectively (n=10) were investigated using blood oxygenation-level dependent (BOLD) fMRI in a 4.7T scanner. Imaging experiments were performed under 1–1.25% isoflurane, and stimuli delivered in the scanner matched those used for behavioral experiments. Representative time courses from individual regions displayed modulation as a function of varying microstimulation frequency (Fig. 1a) and temporal microstructure reflecting individual stimulus pulse trains (Fig. 1b), indicating stimulus specificity of the observed MRI signal changes. Mean time courses averaged in unbiased fashion over anatomically-defined regions in multiple animals showed similar modulation (Supplementary Fig. S5).

A map of the average BOLD signal amplitudes observed in response to MFB stimulation is presented in Fig. 1c. Response amplitudes averaged over 21 anatomically-defined ROIs per hemisphere were computed and are presented in Fig. 1d, and corresponding unmasked images and statistical maps are shown in Supplementary Fig. S6. Substantial responses were measured in cortical and subcortical brain areas, in total accounting for over 50% of brain voxels. Response amplitudes averaged over the full range of stimulation frequencies (Fig. 1d) were lower on average than responses to some of the higher individual frequencies, but similar relative amplitudes were observed among the ROIs (Supplementary Fig. S7a). Response amplitudes

varied somewhat among animals, but few outliers were observed (Supplementary Fig. S7b). Response magnitudes were also similar between groups of animals stimulated with higher vs. lower currents (see Methods and Supplementary Fig. S8). The regions most strongly activated by ipsilateral MFB stimulation included structures commonly associated with reward, such as LH ($0.83\pm 0.22\%$ signal change), the nucleus accumbens shell (NAcS, $0.65\pm 0.16\%$), preoptic area (PO, $1.45\pm 0.54\%$), olfactory tubercle (Tu, $0.68\pm 0.17\%$), and the VTA ($0.89\pm 0.20\%$). Motor control areas were also modulated, with pronounced BOLD signal observed in the substantia nigra (SN, $0.77\pm 0.14\%$), and robust activation also in the thalamus (Thal, $0.48\pm 0.08\%$) and caudate-putamen (CPu, $0.36\pm 0.06\%$). Regions contralateral to the stimulation electrode were activated by the stimulus as well (Fig. 1d inset). The two most pronounced foci of BOLD signal on the contralateral side were observed around Tu ($0.90\pm 0.45\%$) and VTA ($0.72\pm 0.21\%$), suggesting that one or both of these areas might receive relatively direct input via structures activated by MFB stimulation on the side ipsilateral to the electrode.

BOLD responses in specific brain areas track psychometric reward measurements

Brain regions showing fMRI-detectable responses to MFB stimulation may or may not participate in mediating rewarding effects of the stimulus. Moreover, among areas that are required for brain stimulation reward, only a subset might be required for computing or representing reward magnitudes. We hypothesized that the neural populations that encode results of behaviorally-relevant reward magnitude evaluation, if they exist, would show BOLD fMRI signal change amplitudes most closely correlated with a psychometric indicator of subjective reward magnitude. Neural activity induced by the stimulus but prior to or uninvolved with reward integration would be more likely simply to follow the intensity of the stimulus itself.

Similarly, neural activity associated with fibers adventitiously activated by the stimulus but not involved with rewarding effects might also be more likely to track the stimulus intensity, rather than its apparent reward value.

A psychophysical measurement of reward magnitude can be obtained by determining operant response rates as a function of MFB stimulation frequency (Gallistel and Leon, 1991). Such “reward titration curves” have been shown to display a characteristic asymptotic shape, in which response rates rise with increasing frequency up to a “saturation point,” above which larger stimulation frequencies produce roughly constant responses (Mark and Gallistel, 1993, Simmons and Gallistel, 1994). The asymptotic shape of the reward titration curve as a function of MFB stimulation frequency is thought to arise from distributed network properties, rather than from frequency following failure at or near the site of stimulation (Solomon et al., 2015). According to our hypothesis, a brain region or voxel that contains neurons most closely associated with an animal's subjective assessment of reward magnitude in the MFB stimulation paradigm would therefore show BOLD activation amplitudes that correlate with the reward saturation curve, as opposed to the stimulus intensity *per se*.

Emulating earlier studies (Gallistel and Leon, 1991, Mark and Gallistel, 1993, Simmons and Gallistel, 1994), we measured reward titration curves using a matching task in which animals compared two MFB stimuli of differing intensity, each associated with a nose-poke sensor (Fig. 2a). Across multiple trials, one stimulus was fixed at or above the reward saturation frequency for each animal, and the second stimulus was varied over a frequency range around the saturation point. Measuring reward titration curves in this way controlled for factors that could degrade operant performance without specific dependence on stimulation frequency. Eight of the ten animals included in the fMRI analysis of Fig. 1 reached stable performance in this titration

procedure for two consecutive daily sessions prior to scanning. Group average behavioral data from these animals are presented in Fig. 2b. The reward saturation frequency, defined as the lowest MFB stimulation frequency that elicited $\geq 45\%$ of the operant responses, compared with a reference operant associated with 150 Hz stimulation, averaged 137 ± 3 Hz across the group; all individual animals in the group exhibited reward titration curves that reached saturation at 134 or 161 Hz and averaged between 47% and 59% for MFB stimulation frequencies above 134 Hz.

BOLD response amplitudes were measured from these same eight animals as a function of MFB stimulation frequency for the ten frequencies (44–231 Hz) used in behavioral testing. Curves of BOLD amplitude vs. frequency were then subjected to a regression analysis to determine the extent to which fMRI signals paralleled the behavioral results of Fig. 2b. The regression analysis involved fitting the fMRI data from each voxel to a linear combination of two idealized model functions (Fig. 3a), one simulating the saturating behavioral reward titration curve (“reward tracking”) and the second varying linearly with stimulation frequency (“frequency tracking”), plus a constant. Reward tracking and frequency tracking regression coefficients, β_R and β_F , respectively, indicated the fraction of fMRI response amplitudes that could be explained by each of the two models. A map of β_R (red) and β_F (green) values over the brain (Fig. 3b and Supplementary Fig. S9a), scaled by response amplitudes, reveals two pronounced foci of reward tracking signal in NAcS and near the electrode site, adjacent to the amygdala in an area approximately corresponding to the substantia innominata (SI). In these two regions, BOLD responses of up to approximately 2% were fully accounted for by the reward tracking model. Individual voxels showing significantly more reward tracking than frequency tracking character were identified by a t-test of β values obtained over multiple animals. Among regions with strong reward-tracking character, the largest focus of voxels that reached

uncorrected statistical significance ($p < 0.05$) in the t-test was found in NAcS (Fig. 3c and Supplementary Fig. S9b), indicating that BOLD signal in this region most strongly reflects the psychophysical variable required to explain the reward titration behavior of Fig. 2b.

Reward vs. frequency tracking behavior was also assessed for anatomically-defined ROIs. Mean responses to each stimulus frequency are plotted in Fig. 3d for several regions ipsilateral to the electrode placement site; analysis of additional regions is summarized in Table 1. Data from brain areas including NAcS, NAcC, and AmygAM showed responses that appeared to correspond closely to the behavioral data, increasing for low frequencies and then reaching a plateau around the saturation frequency of 137 Hz. Other areas, such as the VTA and Hippo showed monotonically increasing responses, approximately proportional to the MFB stimulation frequency. Each of these ROI-specific curves was normalized and then fit to a regression model incorporating reward and frequency-tracking vectors. Across ROIs, the fraction of variance accounted for by the reward tracking models was anticorrelated with the variance accounted for by the frequency tracking model ($R \leq -0.82$, $p < 10^{-4}$, $n = 21$ for both hemispheres), indicating that the two models tend to be mutually exclusive.

The brain areas with average BOLD signal most strongly correlated with the reward magnitude tracking model ($\beta_R \sim 1$ and $\beta_F \sim 0$) were the NAcS, NAcC, AmygPL, and AmygAM. Data from NAcS, NAcC, and AmygPL only could be explained solely using the reward tracking regressor (F-test $p \leq 0.02$ for reward tracking, $p \geq 0.3$ for frequency tracking). Of these three regions, NAcS displayed the greatest tendency for reward tracking, with $\beta_R = 1.1$ and $\beta_F = 0.0$, as well as the greatest BOLD response to maximal MFB stimulation, $1.02 \pm 0.22\%$, vs. $0.89 \pm 0.16\%$ for NAcC, and a much lower $0.28 \pm 0.10\%$ signal change for AmygPL. Interestingly, contralateral NAcS was one of the most highly reward tracking structures in the hemisphere opposite the

microstimulation electrode, as was contralateral AmygPL (Table 1), but the latter again with much lower amplitude. Results from the behavior vs. frequency tracking model analysis are probably determined by differences in the relative amplitudes of responses to stimulation frequencies above the saturation frequency of 150 Hz. In keeping with this idea, a straightforward evaluation of the mean slope of response amplitudes as a function of stimulation frequency above 150 Hz confirmed that NAcC and NAcS displayed the lowest, most plateau-like slopes (Supplementary Fig. S10). These results together indicate that NAc activity, particularly in the shell, most closely tracks the psychometric reward value recorded in the behavioral test, and that NAcS responses are the most reliable indicator of MFB stimulation reward value in the brain.

Stimulus tracking responses do not result from nonlinear neurovascular coupling

Reward magnitude tracking voxels in NAcS and elsewhere exhibited BOLD response amplitudes that reached asymptotic maximal signal changes at MFB stimulation frequencies near the behaviorally-determined reward saturation frequency. Although a likely interpretation of the results is that these brain regions contain neural populations that specifically encode reward magnitudes, a possible confound could arise from nonlinear behavior of the BOLD signal itself (Logothetis, 2002; Logothetis et al., 2001)—perhaps apparent saturation of the fMRI responses with increasing stimulation frequency results from limited dynamic range of the neurovascular coupling relationship itself, as opposed to the underlying neuronal activity. If nonlinear neurovascular coupling were the explanation for apparent reward magnitude tracking fMRI signals, the saturation effect would likely be most prominent in voxels with the largest BOLD response magnitudes.

To test this explanation, we compared the peak fMRI signal changes in each ROI with an index of reward magnitude tracking given by $\beta R/(\beta R+\beta F)$ (Fig. 4a); index values close to one indicate a greater relative contribution of the saturating reward tracking model to BOLD response variation as a function of stimulation frequency. We found little correlation between $\beta R/(\beta R+\beta F)$ and maximal signal changes ($R=0.17$, $p=0.47$), and even less correlation between maximal signal changes and βR values ($R=0.04$, $p=0.85$). We also compared the peak BOLD signal changes with $\beta R/(\beta R+\beta F)$ for individual voxels in three of the most strongly reward tracking ROIs, NAcS, NAcC, and AmygAM (inset). AmygAM ($R=0.21$, $p=0.32$) and NAcS ($R=0.15$, $p=0.39$) showed no significant correlation, whereas NAcC showed a modest anticorrelation ($R=-0.55$, $p=0.015$) that cannot easily be explained by the hypothesis that nonlinearity of regional BOLD responses favors reward-tracking.

As a further test, we examined whether MRI signal changes observed in an identified macrovascular ROI (Fig. 4b) exhibited apparent reward magnitude tracking as a function of MFB stimulation frequency (Fig. 4c). The macrovascular ROI was defined by the observation of hysteretic responses to stimulation (Lee et al., 1995), and was consistent with known venous distributions in the rat brain (Paxinos, 2004) and hypointense regions in our anatomical scans (Supplementary Fig. S4), rather than with brain areas most susceptible to global physiological changes in rodents (Schroeter et al., 2014). Stimulus-associated signal changes observed in the macrovascular regions were also lateralized toward the brain hemisphere that received direct MFB electrode stimulation (Supplementary Fig. S6), and probably therefore reflect drainage of deoxygenated blood from stimulated tissue. We found that the majority of the macrovascular signal variation was explained by the frequency tracking model ($\beta F=0.63$ vs. $\beta R=0.50$). Although this ROI showed one of the largest average BOLD signal amplitudes, it did not display

a particularly high saturation index (black data point in Fig. 4a). Similar results were obtained under alternative definitions of the vascular ROI (Supplementary Fig. S4). These findings again suggest that reward-tracking asymptotic behavior of some of the regional BOLD signal amplitudes is not a general consequence of nonlinear neurovascular coupling or brain-wide hemodynamic artifacts.

Neither VTA activity nor ventral striatal dopamine release tracks reward value

Given the prominent role of VTA input to NAcS, it was notable that VTA neural activity measured by BOLD fMRI failed to correspond closely to psychometrically determined reward values in the fMRI experiments. To further probe the correspondence between VTA activity and observed responses, we measured VTA-dependent dopamine release amplitudes in NAcS using fixed potential amperometric detection in four rats trained to perform operant responses to MFB stimulation. These experiments applied stimulation conditions similar to those used in our behavioral and imaging experiments in rats anesthetized without paralytic by 2% isoflurane. All animals showed monotonically increasing electrochemical responses to MFB stimulation with a current of 0.35 mA and increasing frequency ranging from 44 to 231 Hz. In three animals tested over an extended stimulation frequency range up to 400 Hz, continually increasing responses were observed for frequencies up to 315 ± 32 Hz (mean \pm s.d.; Fig. 5). This is significantly higher than saturation frequencies of 158 ± 35 Hz observed for each of six rats trained with stimulation currents (0.3–0.4 mA) comparable to those used in the electrochemistry experiments (t-test $p=0.0003$). The dopamine amperometry results are therefore similar to fMRI responses in VTA, which also followed reward stimulation frequency but not the behaviorally measured subjective reward magnitude. These results indicate that the reward-tracking fMRI signals observed in ventral striatum do not arise solely from dopaminergic VTA input.

Targeted silencing of NAcS distorts the reward titration curve

The correspondence between psychometrically determined reward magnitudes and BOLD signal profiles in the NAcS suggests that neural population activity in NAcS may play a role in calculating or storing information about reward value during behavior. To test this hypothesis, we performed transient local inactivation of NAcS during operant behavior. Six additional rats were each implanted with a guide cannula placed above the medial NAcS (Fig. 6a), ipsilateral to an MFB stimulation electrode. These animals were trained on a reduced version of the matching task of Fig. 2, in which their preference between four randomly presented frequencies vs. 150 Hz stimulation was measured in the double nose-poke task. Reward titration curves were recorded after establishment of stable performance. On the subsequent day, the curves were remeasured during infusion of 2% lidocaine via an injection cannula lowered into NAcS. Absolute operant response rates were barely affected by the treatment, with averages of 33 ± 2 and 35 ± 2 rewards/minute harvested prior to and during lidocaine infusion, respectively (t-test $p=0.40$). This indicates that the shift in the reward titration curve produced by lidocaine infusion into NAc cannot be explained simply as the result of a decrease in the rewarding value of MFB stimulation delivered at each frequency.

Reward titration curves obtained in the presence of NAcS-targeted inhibition showed a notable change with respect to baseline behavior however, appearing more linear and less saturating when compared with pre-lidocaine reward titration curves (Fig. 6b). When the same animals were remeasured again after washout of the lidocaine, the curves regained their saturating profile, ruling out nonspecific effects of cannula implantation and fluid infusion on the behavioral results. The changes in reward titration curve could be quantified by applying the regression analysis of Fig. 3 to the behavioral data (Fig. 6c). β_R and β_F values before lidocaine

treatment were 1.3 ± 0.1 and 0.04 ± 0.19 , respectively (significant with $p=0.00015$). βR and βF values during inhibition were 0.5 ± 0.4 and 0.7 ± 0.4 (not significant with $p=0.8$), but after recovery the significant difference ($p=0.005$) was restored with $\beta R=1.7 \pm 0.4$ and $\beta F=-0.5 \pm 0.5$. The fact that NAcS-targeted inactivation perturbed reward titration behavior without attenuating operant response rates per se is consistent with the fMRI analysis in indicating the importance of NAc for evaluation of subjective reward magnitudes.

Reward titration curves were also obtained in the presence of analogous targeted inhibition of VTA (Supplementary Fig. S11). Infusion of 2% lidocaine into VTA also perturbed reward titration behavior. In this case, βR and βF values before lidocaine treatment were 1.3 ± 0.3 and 0.02 ± 0.29 , respectively (significant with $p=0.014$, $n=5$). βR and βF values during VTA inhibition were 0.13 ± 0.56 and 1.0 ± 0.5 (not significant with $p=0.26$). Return of the behavior to pre-treatment values following the procedure was incomplete, indicating the possibility that VTA cannula placement or infusion caused minor damage. In contrast to the slight increase in operant response rate associated with lidocaine infusion into NAc, targeted infusion into VTA produced a modest decrease in the number of operant responses per minute (Supplementary Fig. S12), from 35.0 ± 0.6 to 30.5 ± 2.2 (t-test $p=0.07$). These results are consistent with the well-established importance of VTA as a component of reward circuitry and source of input to NAc, as well as with evidence that VTA activity is less specifically involved in reward magnitude processing.

Discussion

Using a combination of fMRI, electrical microstimulation, and quantitative behavioral measurements in rats, we have demonstrated that the psychometric magnitude of brain stimulation rewards delivered to LH is most consistently tracked by hemodynamic population

activity signals in the shell of the nucleus accumbens. Of 42 other ROIs surveyed across the brain in our study, only a subregion of the amygdala exhibits reward-correlated behavior comparable to NAc. Although the nonlinear nature of neurovascular coupling complicates interpretation of fMRI findings in neurophysiological terms, reward magnitude tracking was not observed in macrovascular compartments and did not seem to arise from saturation of ROI-specific hemodynamic responses. In addition, we found that targeted inactivation in NAc, ipsilateral to rewarding stimulation, correspondingly distorts the reward titration curve in awake, behaving rats without substantially altering their overall willingness to work for reward. These results together suggest therefore that a behaviorally-relevant quantitative measure of brain stimulation reward magnitude is indeed encoded by neural population activity in NAc. Because of the evolutionary conservation of neuroanatomical substrates thought to mediate reward processing, this finding is relevant to the understanding of reward integration and mesolimbic function in both animals and humans.

Our experiments made use of a well-characterized artificial reward, electrical stimulation of the MFB (Olds and Milner, 1954), in place of natural primary rewards such as juice or sucrose solutions. Despite its unphysiological origin, the reward sensation produced by MFB stimulation elicits naturalistic behavioral responses (Olds and Milner, 1954), and can both substitute for (Green and Rachlin, 1991) or compete with (Conover and Shizgal, 1994) natural rewards. Another unphysiological aspect of our experiments was the fact that fMRI brain activity mapping was performed in lightly anesthetized rats, as opposed to the awake, behaving condition used for psychophysical measurements to determine MFB stimulation reward magnitude. This approach is justified in part by previous results showing that fMRI measures of functional connectivity in rats are relatively unperturbed by the isoflurane level used (Wang et al., 2011),

and also by the fact that similar levels of MFB stimulation-evoked dopamine release have been observed in anesthetized vs. awake animals (Tepper et al., 1991); dopamine release also appears relatively independent of isoflurane levels up to 3% (Brodnik and Espana, 2015). The comparison of experimental results across differing physiological conditions is also validated by the fact that NAcS reward tracking in fMRI was shown to be consistent with the targeted inactivation studies we subsequently performed in awake animals.

Some of the conclusions of this study are based on the assumption that the BOLD fMRI amplitudes are an approximately linear measure of neural population activity levels. BOLD responses have been shown to arise primarily from synaptic activity (Logothetis et al., 2001, Rauch et al., 2008), which induces functional hyperemia through parallel chemical signaling pathways involving both neurons and glia (Iadecola and Nedergaard, 2007). The roughly linear relationship between local synaptic activity and hemodynamic responses is known to be violated under conditions of prolonged or intense activity (Logothetis, 2002), so we performed internal controls to assess whether the apparent psychometric reward tracking saturation of BOLD responses we observed resulted from nonlinear neurovascular coupling (Fig. 4 and Supplementary Fig. S4). We found that voxels and ROIs with larger BOLD responses did not systematically display more saturating behavior than those with lower BOLD responses; we also found that macrovascular fMRI signals did not show saturating responses with increasing MFB stimulation frequency. Further, the frequency at which BOLD responses approached their asymptotic value matched the saturation frequency observed in behavioral reward titration experiments (~137 Hz), and took place at stimulation frequencies that in a parametric study of cortical fMRI activation did not induce saturation of hemodynamic responses (Logothetis et al., 2010). Thus, while we cannot rule out that nonlinearities in neurovascular coupling may have

influenced the stimulus intensity-dependent signal amplitudes we report, they do not explain the observed correlations with psychometric reward measurements. In the future, electrophysiological measurements could be made to further characterize the relationship between fMRI signals we recorded and underlying neural activity patterns at the cellular level.

It was a hypothesis of our study that foci of neural population activity correlated with psychometric reward titration curves could be identified from fMRI data; we in fact discovered such foci in NAc and, less robustly, near AmygAM (red in Fig. 3). In addition to these hot spots of reward magnitude tracking, we found multiple areas where BOLD signal correlated roughly linearly with rewarding stimulation frequency (green in Fig. 3). Neural population activity averages in these frequency tracking regions cannot predominantly reflect subjective assessments of reward magnitude because they do not exhibit the saturating profile required to explain behavioral performance in the matching tests we performed. Frequency tracking areas probably include both “first stage” reward-related fibers (Gallistel et al., 1981) that transmit MFB stimuli to sites of integration and behavioral control, and also areas not naturally involved in reward processing. While fractional reward magnitude tracking behavior was observed in several ROIs (indicated by βR values between 0 and 1; Table 1), these regions were modulated to a lesser extent or less reliably than hemodynamic signals in NAcS. Because BOLD responses reflect gross population-averaged activity, it is likely that individual cells both outside and inside NAcS respond to MFB stimuli with characteristics that differ substantially from the mesoscale fMRI readouts. It is possible that cells in distal structures contribute to saturating BOLD response profiles in NAc (as suggested also by the effect of VTA inhibition on reward titration behavior), and it is also possible the balance of reward vs. frequency tracking in some structures might shift if different rewarding stimuli were used. Assuming approximate linearity of BOLD signaling,

our results do however rule out the possibility that a single well-resolved neural population outside NAc robustly signals reward magnitudes under all conditions, since we only observed strong reward magnitude tracking activity in NAc.

Although the mechanisms by which reward tracking activity is established in NAcS may be complex, two pieces of evidence suggest that factors other than VTA input and striatal dopamine release may be involved. First, caudal ROIs including VTA did not show strong reward tracking BOLD signal in the stimulus titration analysis. Second, electrochemistry experiments dissociated dopamine release from fMRI signals in NAc and from behavioral performance in the reward titration tests, a result consistent with previously reported neurochemical measurements (Cossette et al., 2015, Garris et al., 1999, Kilpatrick et al., 2000, Miliaressis et al., 1991). Thus, despite evidence that stimulation of dopamine neurons is sufficient for behavioral reinforcement (Kim et al., 2012, Witten et al., 2011), and that VTA inactivation perturbs reward titration behavior (Supplementary Fig. S11), our results suggest that NAc activity ipsilateral to MFB stimulation reward relies at least to some extent on non-dopaminergic inputs to NAc (Britt et al., 2012). Further mechanistic analysis of the population-level responses we observe, in terms of contributions from specific neural projections or neurotransmitter-dependent systems, must be performed using more targeted and invasive techniques.

These results are relevant to the interpretation of BOLD responses in human fMRI studies of the reward system. Earlier reports have associated NAc BOLD signals with dopamine release and argued that these signals correspond to activity of VTA dopaminergic neurons as measured in nonhuman primates (McClure et al., 2003, O'Doherty et al., 2003). Two of our results—the fact that NAc and VTA fMRI signals do not similarly correspond to reward

magnitudes, and the finding that amperometric dopamine recordings fail to parallel fMRI activation measured under similar conditions—suggest that NAc BOLD signals are not a faithful indicator of dopaminergic signaling. Also relevant to human fMRI findings is our failure to discern reward magnitude tracking in OCx, an area that includes orbitofrontal regions shown to signal reward values in associative tasks (Murray et al., 2007), and to which human studies have attributed reward magnitude sensitivity (Kringelbach, 2005). Relatively weak responses we observed in OCx and in cortical areas more generally suggest that the MFB stimulation paradigm most effectively engages evolutionarily primitive components of reward processing circuitry, and that these circuit elements are also most directly involved in reward magnitude computations.

Our analysis of reward magnitude-related neural population activity in rats supports several existing lines of evidence that point to a particularly important role for NAc neuronal activity in signaling reward magnitudes (Carlezon and Thomas, 2009). Pharmacological (Ikemoto and Wise, 2004) and optogenetic (Nieh et al., 2013) manipulation of NAc activity influences operant responding or consummatory behavior in rewarded tasks. Injection of μ -opioids into NAcS is especially effective at promoting feeding and affective indications of pleasure (Smith et al., 2011). NAcS lesions impede association of reward magnitudes with environmental cues (Albertin et al., 2000). Numerous electrophysiological studies have recorded the dependence of activity on expected reward value or reward receipt in NAc in rodents (Ambroggi et al., 2011, Nicola et al., 2004, Roitman et al., 2005, Setlow et al., 2003, Taha and Fields, 2005). Human fMRI studies have repeatedly implicated ventral striatum as one of a number of areas involved in processing rewards (Doya, 2008). A particularly close association of striatal activity with reward delivery events is suggested by evidence that this area signals

immediate but not delayed ingested (McClure et al., 2007) or monetary (Hariri et al., 2006, McClure et al., 2004) rewards. Functional imaging in both humans and animals has also revealed strong NAc responses to injection of drugs of abuse (Knutson and Gibbs, 2007). Our results go beyond the earlier findings by singling NAc out, from an unbiased whole-brain study, as a locus where activity evoked directly by reward delivery correlates with a behavioral measure of subjective reward magnitude. This suggests in turn that neural population activity in NAc, more so than activity in distal input or projection fields, is particularly closely associated with hedonic aspects of reward.

Author contributions

AMF, SJB, MTC, and AJ designed the experiments; AMF and SJB collected MRI and behavioral data; LXC performed electrochemistry experiments; HAW assisted with behavioral experiments; GWG contributed analytical methods; AMF and AJ analyzed the data and wrote the paper.

Acknowledgements

The authors thank Peter Shizgal for suggesting the reward titration approach and for advice regarding behavioral methods, Sonal Jhaveri for consultation regarding neuroanatomy, and Itamar Ronen and George Dai for assistance in implementing diffusion tensor imaging methods. Ki Goosens, Ann Graybiel, Joe Mandeville, James Schummers, and Mriganka Sur are thanked for their advice on aspects of the study. Charles Blaha is thanked for extensive consultation regarding electrochemistry and Mark Howe and Ann Graybiel are thanked for help with pilot measurements. Ki Goosens, Peter Shizgal, Mitul Desai, and Taekwan Lee are also thanked for comments on the manuscript. This work was supported by grants from the Dana Foundation, the Raymond and Beverley Sackler Foundation, DARPA (W911NF-10-0059), and the NIH (R01-DA028299, R01-DA038642).

Figures

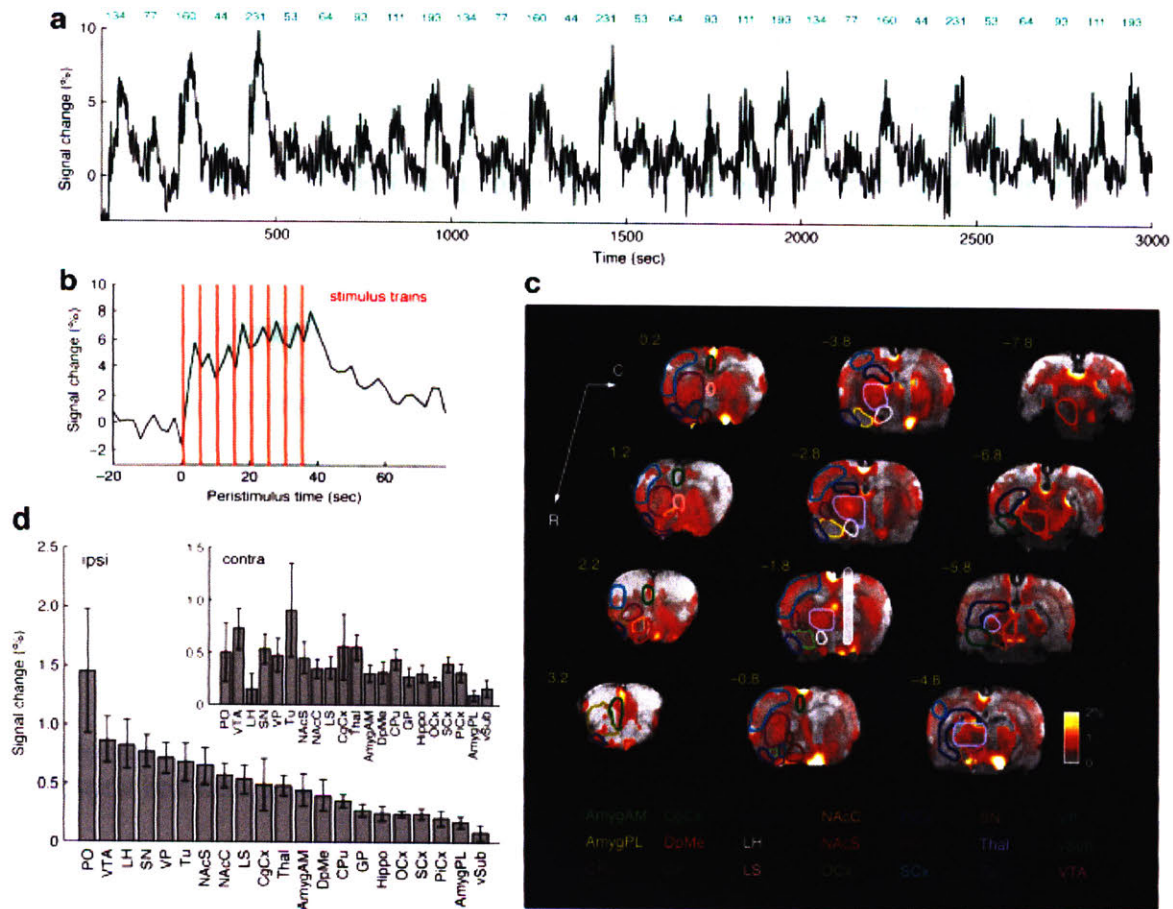


Fig. 1. BOLD fMRI responses to MFB reward stimulation. (a) Representative blood oxygenation level dependent (BOLD) fMRI response to electrical stimulation of the medial forebrain bundle (MFB), averaged over all voxels in the lateral hypothalamus (LH) ipsilateral to the stimulation electrode in a single rat. Ten stimulation frequencies (green labels, in Hz) were presented in pseudo-random order and the stimulation sequence was repeated three times over the duration of the scan session. Each green rectangle corresponds to one stimulation block. (b) Average LH response to a 40 s block of eight MFB stimulation trains delivered at 231 Hz, showing peaks in the response profile following each 1 s train (vertical red lines). The gray shading indicates standard error of the mean (s.e.m.) over three stimulus presentations in a single animal, at time points with respect to the stimulus onset at $t=0$ seconds. (c) Map of average fMRI responses to MFB stimulation over stimulation frequencies from 44 to 231 Hz in a group of ten animals. Data are displayed as an array of 1 mm slices from rostral to caudal, beginning with the most rostral slice at the lower left (coordinates with respect to bregma displayed to the top left of each slice, in yellow). Background images are T2-weighted anatomical images. Color overlays in red-yellow depict the BOLD amplitude as % signal change, according to the color bar (lower right). Colored outlines depict boundaries of 21 regions of interest (ROIs); only ROIs contralateral to the electrode (white shaded bar, -1.8 from bregma) are drawn. Color-coded ROI labels at bottom correspond to the ROI

outlines. Data were thresholded for statistically significant activation with partial Bonferroni correction ($p \leq 0.0001$). (d) ROI-averaged mean BOLD signal modulations elicited by 44–231 Hz MFB stimulation, arranged from maximum to minimum amplitude for ROIs ipsilateral to the stimulation electrode. Contralateral response amplitudes are shown in the inset. Error bars denote s.e.m. over animals ($n=10$). Signal change calculations included all voxels in each ROI, excepting regions of signal drop out due to implants and areas dominated by macrovascular responses, which were excluded from ROI averages. (For interpretation of the references to color in this figure legend, the reader is referred to the web version of this article.)

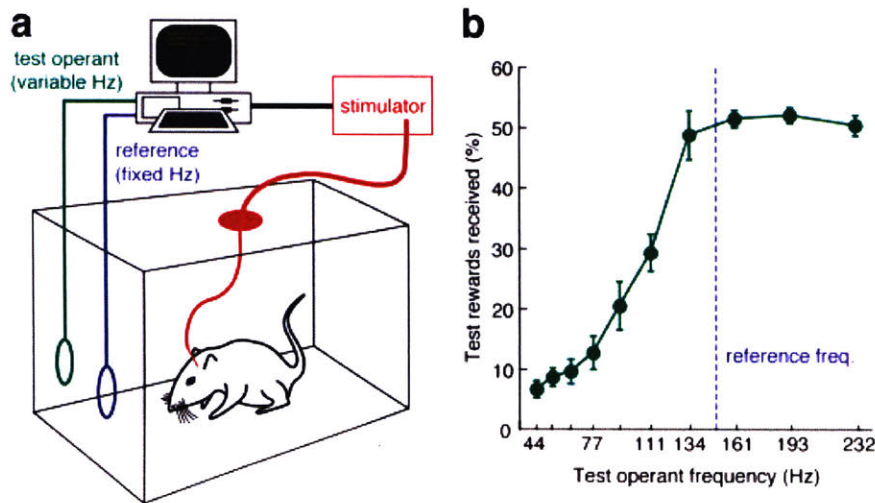


Fig. 2. Reward titration analysis and behavioral results. (a) Diagram of the apparatus for measuring reward titration curves. Rats implanted with an MFB stimulation electrode and connected to a constant current stimulator (red) were placed into an operant chamber with two nose poke holes. One hole was associated with a stimulation reward delivered at a fixed reference frequency (blue) while the second hole was associated with a test stimulation frequency that varied from trial to trial (green). Timing of the trials and stimuli was automated by custom software running on a computer. (b) The percentage of test operant actions is plotted as a function of test frequency for a range of frequencies, offered in the two-choice test against a reference frequency of 150 Hz. Stimulation frequencies below 134 Hz are increasingly rewarding and are chosen with increasing probability as they approach the reference. Frequencies above 134 Hz are virtually indistinguishable from 150 Hz stimulation, giving rise to the flat response profile at high frequency that characterizes the reward saturation phenomenon. The graph shows mean and s.e.m. for 8 rats. (For interpretation of the references to color in this figure legend, the reader is referred to the web version of this article.)

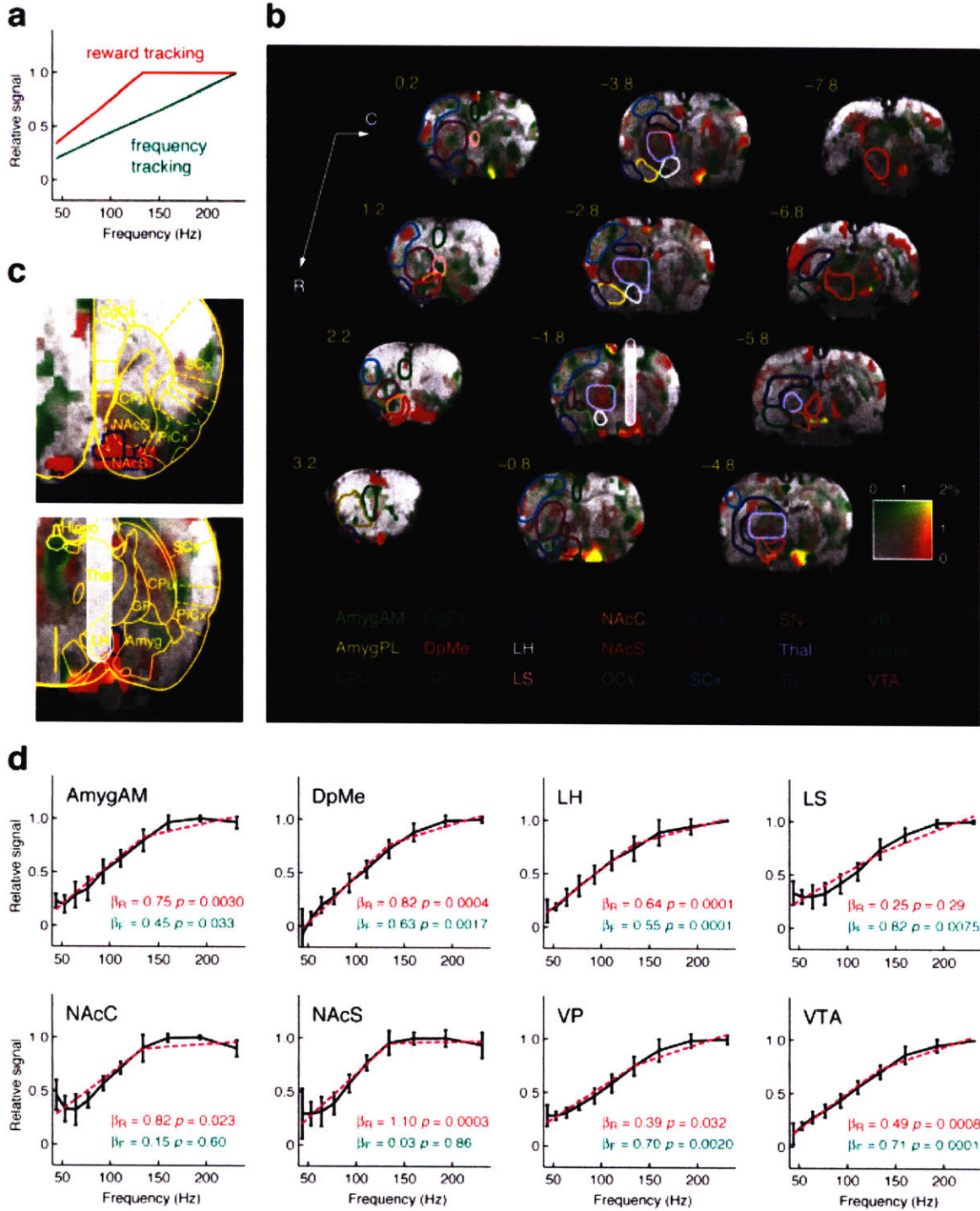


Fig. 3. Brain region-specific tracking of psychometric reward magnitude. (a) Frequency tracking (green) and reward tracking (red) models used for regression analysis of stimulation frequency-dependent BOLD response amplitudes. The frequency tracking model predicts responses linearly proportional to the stimulation frequency, whereas the reward tracking model idealizes the saturation effect seen in the behavioral reward titration analysis, with an asymptotic saturation frequency equal to the experimentally

observed value in Fig. 2b. (b) Voxel-level characterization of frequency vs. reward tracking by BOLD signal amplitudes in a group analysis of 8 rats. Amplitudes as a function of frequency were analyzed using a GLM incorporating frequency and reward tracking regressors from panel A. The amount of fMRI signal change (%) ascribed to frequency and reward tracking models is color coded such that pure frequency tracking appears green, pure reward tracking appears red, and an equal mixture appears yellow (color code shown bottom right). Maps are overlaid on a T2-weighted anatomical scan, and ROIs and labels are shown as in Fig. 1c. (c) Close up of the two most pronounced foci of reward tracking near nucleus accumbens shell (NAcS, top) and adjacent to the amygdala (Amyg) near the stimulation electrode site (bottom). A standard histological map (Paxinos and Watson, 1998) is superimposed over the data. Voxels that showed statistically significantly (t-test $p < 0.05$) greater reward tracking than frequency tracking are outlined in blue; NAcS contains the largest cluster of significantly reward tracking voxels. (d) Plots of normalized mean BOLD amplitudes vs. stimulation frequency for several ROIs (mean \pm s.e.m. shown for each in black, $n=8$). Relative contributions of the two models to the BOLD signal from each ROI were expressed as coefficients β_R and β_F for reward and frequency tracking regressors, respectively. Corresponding p values for F-tests of the significance of each regressor's contribution are noted. Pink dotted lines indicate the best fit regression curve in each case. Among the ROIs shown, NAcS and NAcC were the only regions that showed significant contribution of the reward tracking model, but not the frequency tracking model. Corresponding β_R values indicated that over 80% of the fMRI signal variation could be explained by the reward tracking model in both NAcC and NAcS. (For interpretation of the references to color in this figure legend, the reader is referred to the web version of this article.)

ROI ^a	Ipsilateral				Contralateral			
	β_R	<i>p</i>	β_F	<i>p</i>	β_R	<i>p</i>	β_F	<i>p</i>
AmygAM	0.75	0.0030	0.45	0.033	0.16	0.57	0.91	0.011
AmygPL	1.14	0.0016	0.24	0.33	1.48	0.012	0.16	0.72
CPu	0.16	0.57	0.82	0.019	0.30	0.078	0.61	0.0038
CgCx	0.13	0.65	0.60	0.074	0.34	0.054	0.40	0.030
DpMe	0.82	0.0004	0.63	0.0017	0.76	0.0007	0.61	0.0024
GP	0.22	0.42	0.75	0.022	0.69	0.0015	0.40	0.023
Hippo	0.40	0.011	0.89	0.0001	0.89	<10 ⁻⁴	0.44	0.0006
LH	0.64	0.0001	0.55	0.0001	-0.86	0.14	1.61	0.017
LS	0.25	0.29	0.82	0.0075	0.01	0.98	1.14	0.013
NAcC	0.82	0.023	0.15	0.60	-0.02	0.96	0.97	0.032
NAcS	1.10	0.0003	0.03	0.86	0.89	0.029	-0.02	0.94
OCx	-0.01	0.98	1.23	0.014	0.20	0.39	0.72	0.012
PO	0.53	0.0001	0.69	<10 ⁻⁴	0.68	0.0041	0.76	0.0023
PiCx	0.05	0.84	1.04	0.0024	0.40	0.016	0.69	0.0009
SCx	0.50	0.10	0.80	0.020	0.59	<10 ⁻⁴	0.56	<10 ⁻⁴
SN	0.68	0.0093	0.59	0.018	0.64	0.0009	0.36	0.019
Thal	0.42	0.0009	0.54	0.0002	0.59	<10 ⁻⁴	0.39	0.0003
Tu	0.58	0.0008	0.46	0.0030	0.13	0.078	0.78	<10 ⁻⁴
VP	0.39	0.032	0.70	0.0020	0.50	0.0050	0.66	0.0011
vSub	-0.03	0.95	1.80	0.015	0.76	0.17	0.65	0.23
VTA	0.49	0.0008	0.71	0.0001	0.52	0.0016	0.69	0.0003

Table 1. Reward vs. frequency tracking in 42 ROIs

Region of interest (ROI) definitions and data analysis were performed as described in the main text. β_R and β_F denote relative contributions of reward tracking and frequency tracking models, respectively, to BOLD amplitudes recorded as a function of MFB stimulation frequency. Reported *p* values reflect *F*-test results for the corresponding regressors. Data for ROIs both ipsilateral and contralateral to the MFB electrode are provided. See text and Fig. 3 for further details. The number of voxels in each ROI is listed in Table S1.

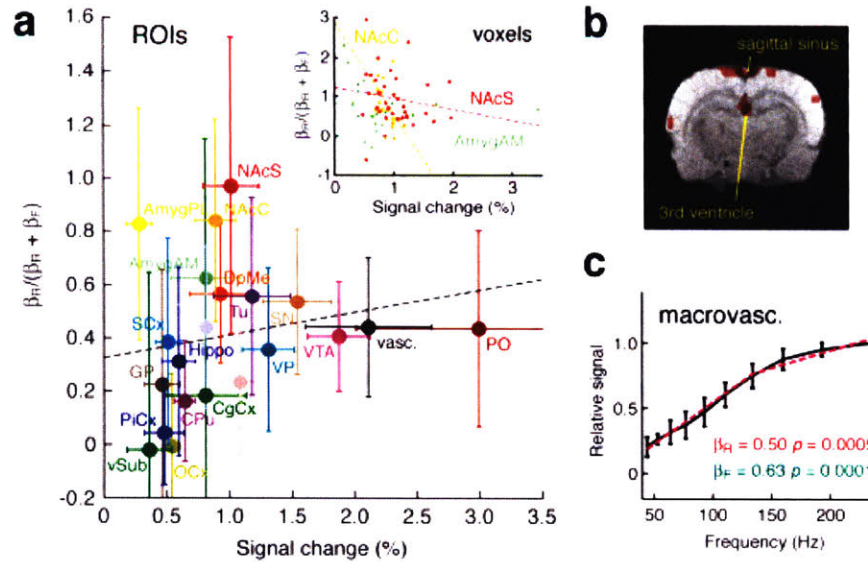


Fig. 4. Vascular contributions do not explain saturating fMRI profiles. (a) BOLD amplitudes observed at the maximal stimulation frequency (horizontal axis) were plotted vs. an index of response saturation, equal to $\beta_R/(\beta_R + \beta_F)$, where β_R and β_F are regression coefficients for reward and frequency tracking models (see text and Fig. 3). Mean and s.e.m. values are shown across animals ($n=8$) for each ROI, and for a vascular compartment (black). Dotted line shows best linear fit to the data ($R=0.17$, $p=0.47$). Inset shows correspondence between BOLD amplitudes to 231 Hz stimulation and saturation index for individual voxels, with linear regression fits in three ROIs: NAcS (red; $R=0.15$, $p=0.39$), NAcC (orange; $R=0.55$, $p=0.015$), and AmygAM (light green; $R=0.21$, $p=0.32$). NAcC showed statistically significant anti-correlation, and other regions were uncorrelated, failing to support the hypothesis that reward tracking BOLD responses result from saturation of neurovascular coupling. (b) Representative macrovascular regions identified on the basis of hysteretic responses to MFB stimulation (see Methods). Sagittal sinus and vessels near the third ventricle shown in slice -2.8 mm from bregma. (c) Macrovascular BOLD response amplitudes as a function of MFB stimulation frequency. Regression analysis with reward tracking and frequency tracking models are shown as in Fig. 3d, with corresponding β and F-test p values noted. The frequency tracking model accounted for the majority of variance. (For interpretation of the references to color in this figure legend, the reader is referred to the web version of this article.)

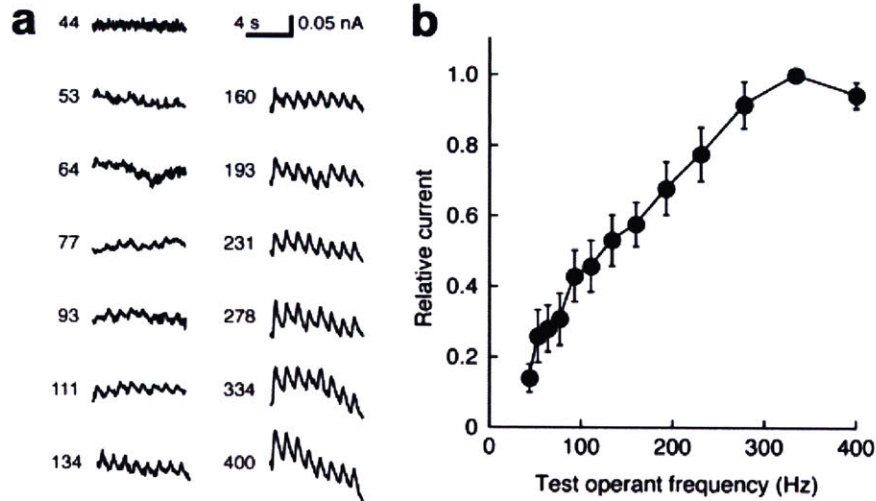


Fig. 5. NAc dopamine signals saturate only at very high frequency. (a) Dopamine oxidation detected by fixed potential (0.8 V) amperometry during MFB stimulation in a representative animal under conditions similar to the fMRI experiments. Each trace shows responses to a series of eight pulse trains delivered with the stimulation frequency indicated. (b) Normalized average amperometric responses ($n=3$) measured over a range of frequencies including those used for behavioral and MRI experiments. Saturation is observed only at frequencies of 315 ± 32 Hz (mean \pm s.d.).

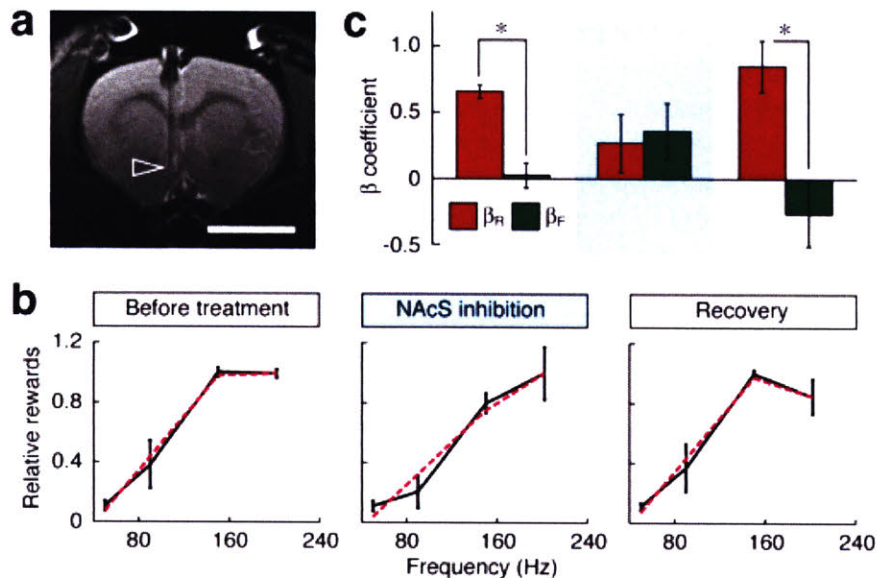


Fig. 6. Targeted inactivation of NAcS perturbs reward titration behavior. (a) Cannulae were implanted in the medial NAcS of rats, ipsilateral to MFB stimulation electrodes; correct placement was verified by MRI at 7 T. Arrowhead denotes cannula tip in a representative animal. Scale bar=5 mm. (b) Reward titration curves were measured using methods analogous to those of Fig. 2, but with a reference stimulation frequency of 150 Hz and four comparison frequencies of 50, 90, 150, and 202 Hz. Data were obtained from six animals that had reached stable performance on the task, and graphs represent the relative number of rewards harvested from the nosepoke hole associated with the

titrated stimulation frequency the day before treatment (left), during infusion of 0.1 $\mu\text{L}/\text{min}$ of 2% lidocaine into NAcS (middle), and on the day after the perturbation (right). Black curves denote measured values with error bars over six animals; dashed magenta lines are best fit from a regression model including linear and saturating components as in Fig. 3a. (c) Average regression coefficients for linear and saturating models (β_L and β_R , respectively) fit to individual animal reward titration curves obtained before, during, and after NAcS inactivation, showing that inactivation abolishes the saturating profile with $\beta_R > \beta_L$ ($p \leq 0.005$) observed both before and after lidocaine treatment.

Supplementary material

ROI*	<i>ipsilateral</i>	<i>contralateral</i>
AmygAM	25	25
AmygPL	37	34
CPu	170	173
CgCx	53	52
DpMe	97	99
GP	7	13
Hippo	105	123
LH	23	36
LS	16	16
NAcC	19	19
NAcS	34	34
OCx	47	43
PO	26	26
PiCx	77	83
SCx	277	286
SN	25	22
Thal	111	158
Tu	20	20
VP	19	19
vSub	32	40
VTA	16	16

Table S1. Number of voxels included in 42 ROIs

* Region of interest (ROI) definitions were established as described in the text.

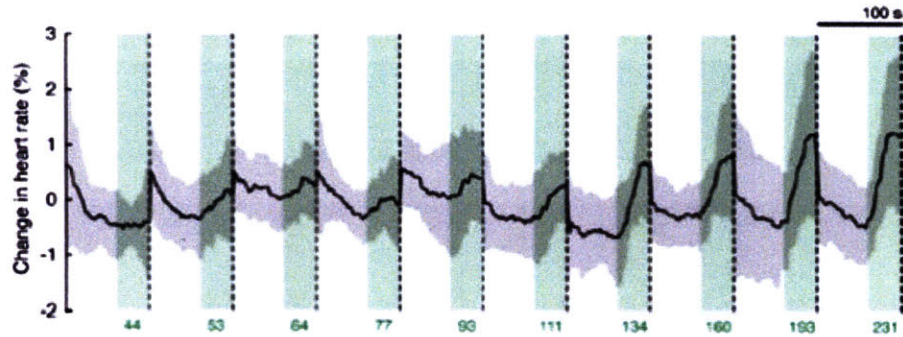


Fig. S1. Heart rate time courses during imaging. Mean heart rate changes observed in response to MFB stimulation during fMRI experiments, at ten frequencies in Hz indicated in green on the horizontal axis, each applied during the 40 s period indicated by green shading. Each trace represents a mean across the ten animals included in the analysis of Fig. 1, with three stimulations per animal, and standard deviations across animals indicated in gray shading. The average absolute heart rate was 428 ± 37 (s.d.) beats per minute.

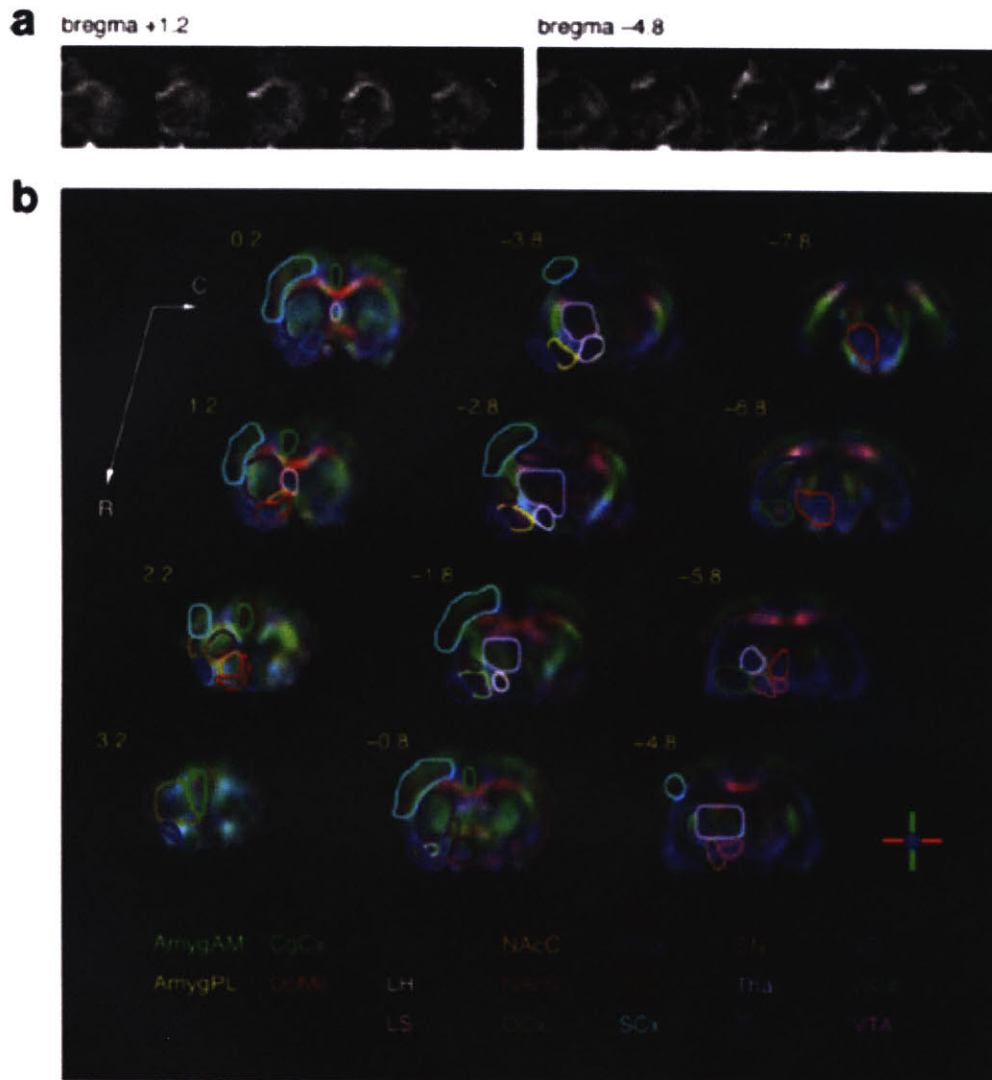


Fig. S2. ROI definition facilitated by diffusion tensor data. (a) Diffusion tensor (DTI) images were acquired from each animal and used as the basis for coregistering brains into a common coordinate space. Fractional anisotropy maps from individual animals were aligned using 3D affine transformations. This procedure minimized the number of alignment steps required for each animal, and ensured that the basis for alignments was well matched to ROI definitions. Results from five rats are presented here, at one rostral and one caudal coordinate (right hemispheres shown). (b) Features defined by the mean fractional anisotropy image (color underlay) were used along with anatomical markers to define regions of interest (ROIs) corresponding to 21 brain structures in each hemisphere. Color coded ROI outlines correspond to atlas abbreviations listed at the bottom of the figure. The directionality of diffusion (i.e. likely fiber orientation) in the DTI scan is defined by the key at the bottom right, where green denotes dorsal-ventral, red denotes left-right, and blue denotes rostral-caudal axes.

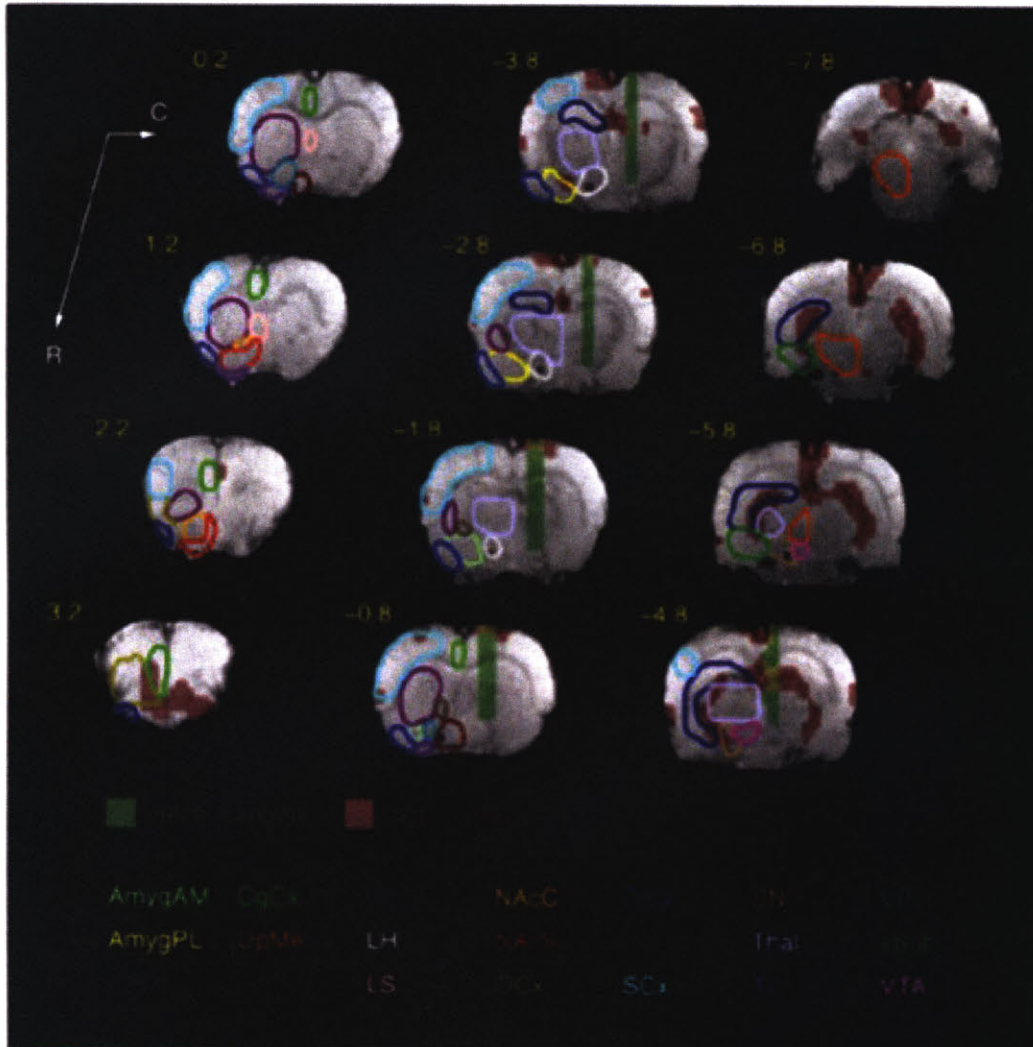


Fig. S3. Regions excluded from fMRI analyses. Masks were defined by signal drop out due to electrode and infusion cannula placement (semitransparent green) and hysteretic responses to MFB stimulation (semitransparent red), assumed to arise from macrovascular components. These regions were excluded from GLM analyses and evaluation of ROI average responses. Masks are shown here overlaid on a T2*-weighted image, again with ROI outlines superimposed in color-coded outlines on the left hemisphere.

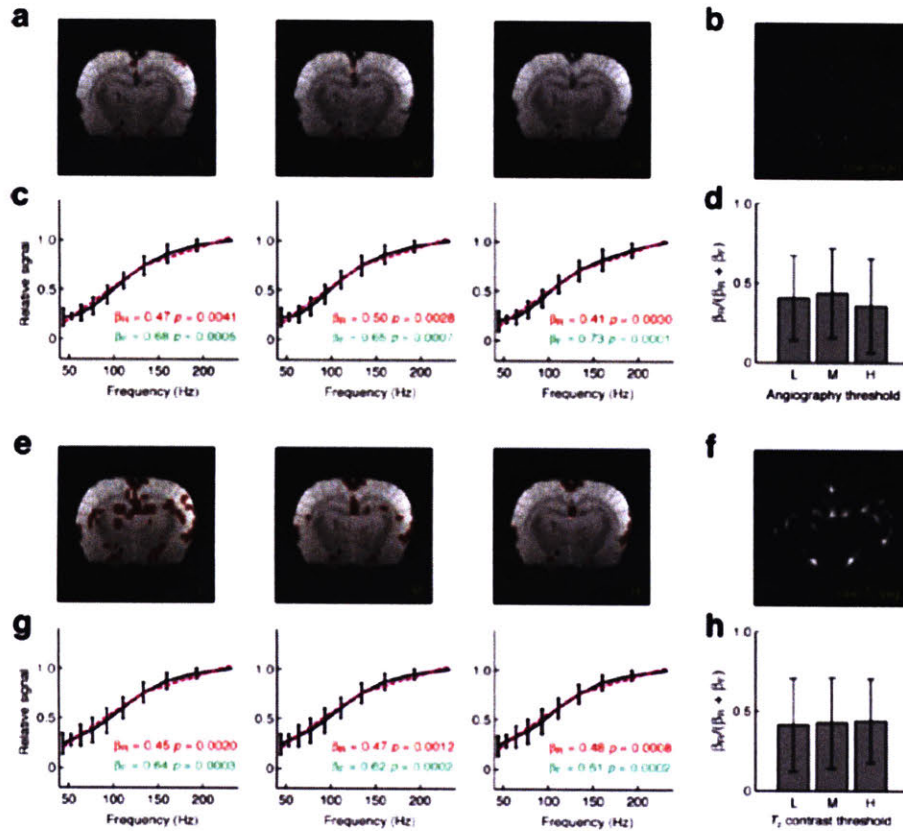


Fig. S4. Reward magnitude tracking by alternative vascular ROIs. (a) Candidate vascular ROIs defined by thresholding an angiography image acquired with geometry identical to the anatomical scans used throughout the paper (shown for bregma -2.8 mm only). Stringency of the thresholding was set to low (L), medium (M), and high (H) levels to define progressively more restrictive ROIs, indicated by transparent red overlaying the anatomical scans in each subpanel. (b) An image slice showing raw angiography data used for the segmentation in panel (a). (c) Titration curves showing fMRI signal change amplitudes determined as a function of stimulus frequency for ROIs as shown in panel (a). Insets show regression coefficients for psychometric reward tracking (β_R) and stimulus frequency tracking (β_F), as in Figs. 4-5. Black curves show data values, and dashed magenta lines indicate the best-fit regression model. See main text for further details. (d) Saturation indices, as defined in the main text by $\beta_R/(\beta_R + \beta_F)$ for the three angiography-based ROIs shown in (a). (e) Candidate vascular ROIs defined by performing interior edge detection on T2*-weighted anatomical MRI slices. Low (L), medium (M), and high (H) stringency maps were obtained using Sobel parameters 15, 20, and 25, respectively, followed by down-sampling to the resolution of the EPI scans used for functional imaging. (f) Results of edge detection performed with Sobel parameter 15 on the anatomical scan underlay in (e). (g) Regression analysis equivalent to panel (c), performed using the vascular ROIs depicted in (e). (h) Saturation indices obtained using the candidate vascular ROIs in (e).

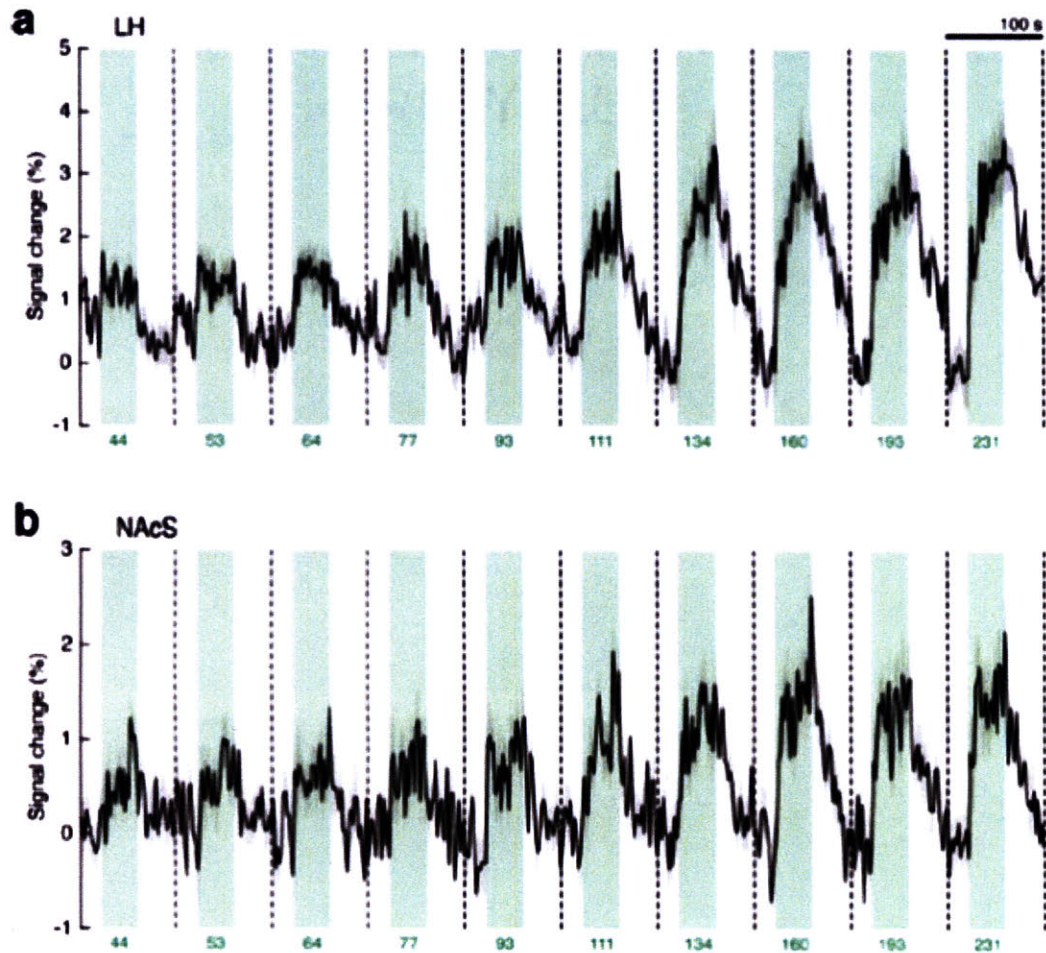


Fig. S5. Average responses to MFB stimuli of varying frequency. Mean ROI-averaged fMRI time courses recorded from ten rats in response to MFB stimuli at each of the frequencies shown, with other stimulation and imaging parameters as described in the text. Results shown for (a) LH and (b) NAcS ROIs were obtained by averaging over all stimulus presentations and all voxels in each ROI, with gray shaded areas depicting the s.e.m. across animals. Green shaded rectangles denote the duration of stimulation during 100 s windows for each stimulation condition.

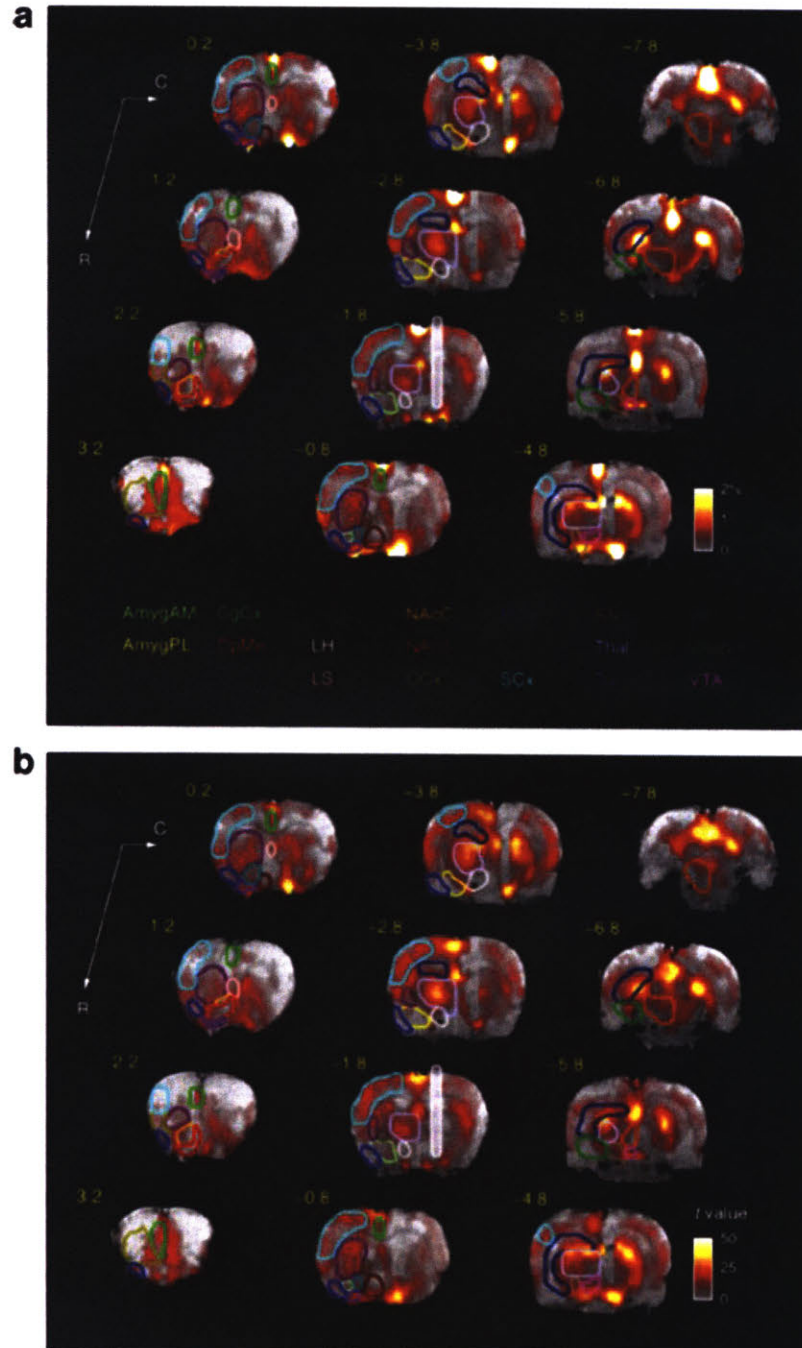


Fig. S6. MFB stimulus response maps including vascular regions. (a) A map of average fMRI responses to MFB stimulation in a group of ten animals, as in Fig. 1a, but with responses in the vascular ROI included as well. Color coded ROI outlines are shown contralateral to the stimulation site. (b) A map corresponding to panel (a), showing t-test statistics for rejecting the null hypothesis of no significant stimulus response. Given 2.3×10^4 voxels included in the analysis, the threshold for elimination of false positives with a confidence of $p < 0.05$ following full Bonferroni correction is $t = 4.7$.

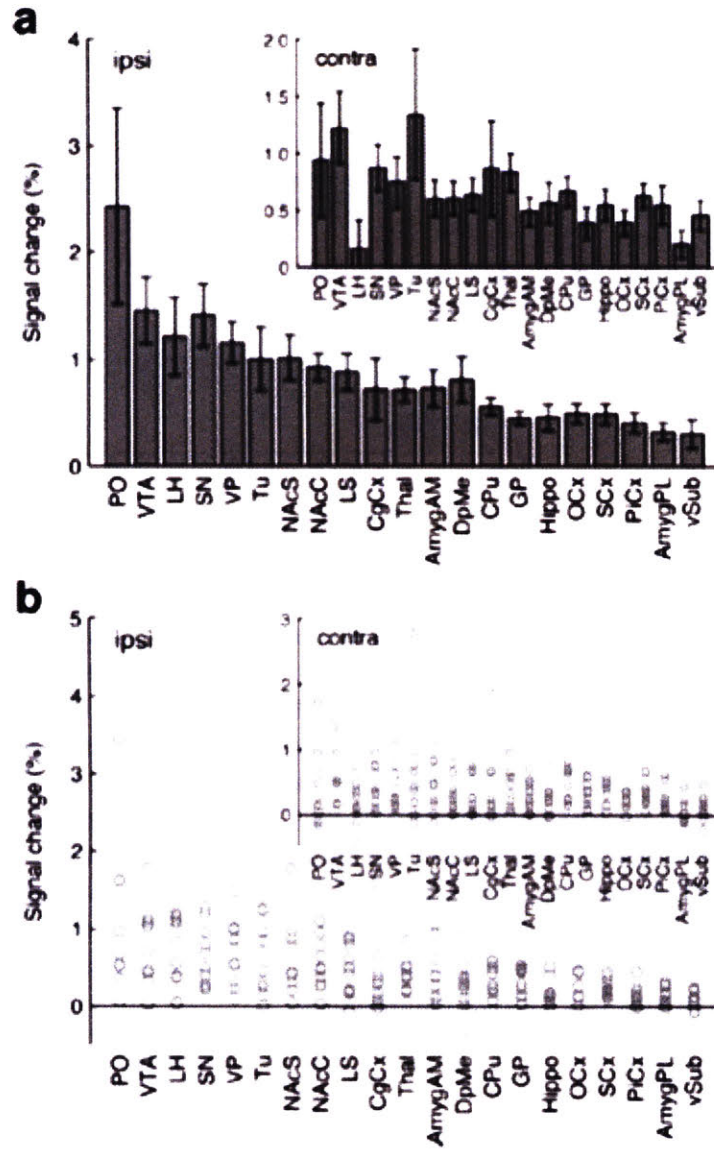


Fig. S7. Individual response amplitudes. (a) BOLD responses to 160 Hz from the experiments of Fig. 1 (n = 10). (b) Average BOLD responses in response to stimulation over the full 44-231 Hz range, measured from the ten individual animals of Fig. 1. Insets denote measurements from ROIs contralateral to the stimulation electrode.

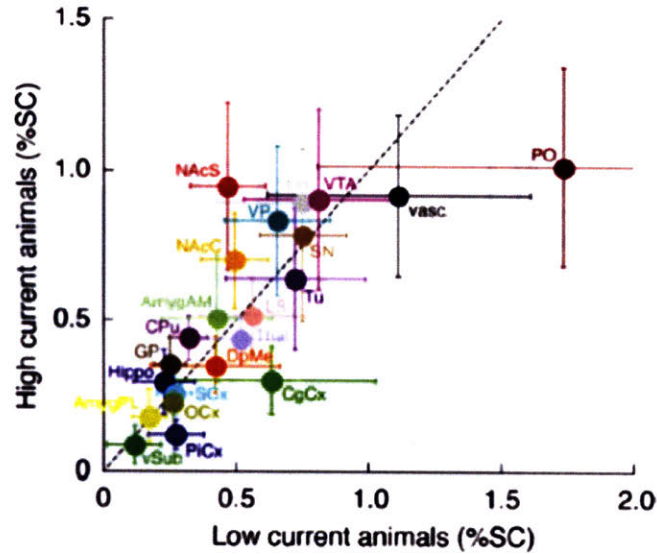


Fig. S8. Response amplitudes to low vs. high stimulation current. The ten rats that contributed to the data of Fig. 1 were divided into two groups (both $n = 5$) based on the stimulation currents used with each animal. The low current animals received stimulation with currents of 0.3-0.6 mA, while the high current animals received stimulation with currents of 0.7-0.9 mA. Mean response amplitudes and s.e.m. values were calculated in units of percent signal change (%SC) for each group from each ROI, as in Fig. 1d. Results plotted for low current animals vs. high current animals show that each ROI falls within error of the dotted line corresponding to equal responses in the two groups. This indicates that the procedure of choosing the maximum stimulation currents that avoid motion effects on a per animal basis results in stimuli that produce approximately equivalent neurophysiological responses in the two sets of animals, despite the differences in absolute current magnitudes.

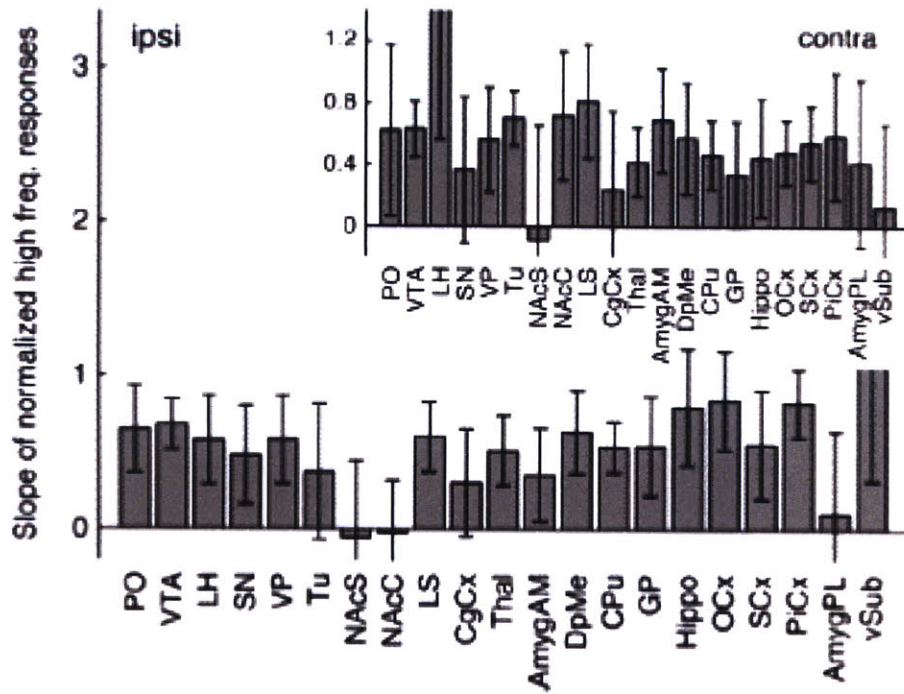


Fig. S10. Slopes of BOLD amplitudes above the saturation frequency. Slopes of BOLD amplitudes measured as a function of stimulation frequency for frequencies above the saturating stimulus intensity of 150 Hz, for the experiments of Fig. 3. Inset denotes measurements from ROIs contralateral to the stimulation electrode. Two values are cut off: ipsilateral vSub (1.17 ± 0.85) and contralateral LH (1.49 ± 0.93).

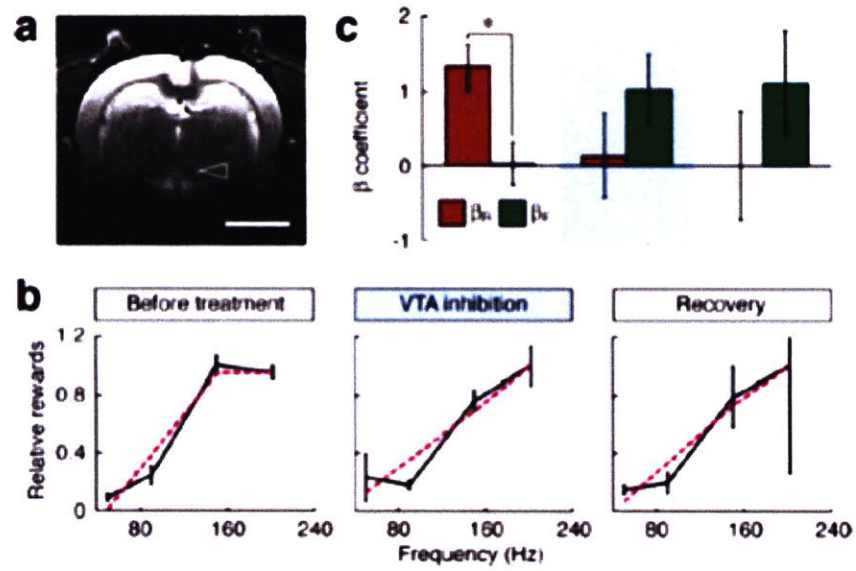


Fig. S11. Targeted inactivation of VTA perturbs reward titration behavior. (a)

Cannulae were targeted toward the VTA of rats, ipsilateral to MFB stimulation electrodes; correct placement was verified by MRI at 7 T. Arrowhead denotes cannula tip in a representative animal. Scale bar = 5 mm. (b) Reward titration curves were measured using the methods of Fig. 6, with a reference stimulation frequency of 150 Hz and four comparison frequencies of 50, 90, 150, and 202 Hz. Data were obtained from five animals that had reached stable performance on the task, and graphs represent the relative number of rewards harvested from the nosepoke hole associated with the titrated stimulation frequency the day before treatment (left), during infusion of 0.1 μ L/min of 2% lidocaine into VTA (middle), and on the day after the perturbation (right). Black curves denote measured values with error bars over six animals; dashed magenta lines are best fit from a regression model including linear and saturating components as in Fig. 6. (c) Average regression coefficients for linear and saturating models (β_L and β_R , respectively) fit to individual animal reward titration curves obtained before, during, and after VTA inactivation, showing that inactivation abolishes the saturating profile with $\beta_R > \beta_L$ ($p = 0.014$) observed before lidocaine infusion. Recovery is incomplete and may reflect residual effects of the treatment, including damage from infusion or cannula placement. The small size of VTA relative to NAc may have made it more susceptible to damage than NAc, for which full recovery was observed following lidocaine treatment (Fig. 6).

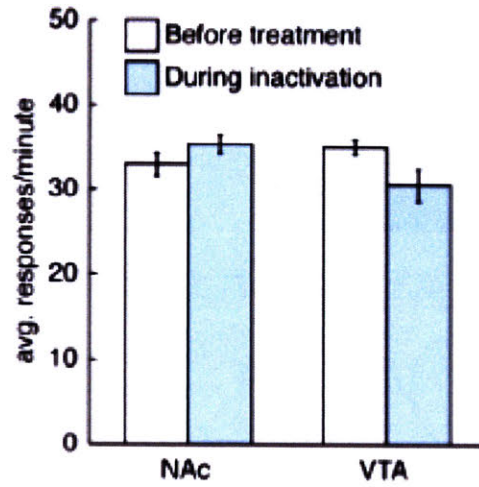


Fig. S12. Local inactivation minimally affects mean response rates. Mean operant response rates (nospokes per minute) were recorded from rats before or during infusion of 0.1 $\mu\text{L}/\text{min}$ of 2% lidocaine into medial NAcS ($n = 6$) or VTA ($n = 5$). Lidocaine infusion at neither site produced a significant change in operant response rate.

References

- Albertin, S.V., Mulder, A.B., Tabuchi, E., Zugaro, M.B., and Wiener, S.I. (2000) Lesions of the medial shell of the nucleus accumbens impair rats in finding larger rewards, but spare reward-seeking behavior. *Behav Brain Res* 117:173-183.
- Ambroggi, F., Ghazizadeh, A., Nicola, S.M., and Fields, H.L. (2011) Roles of nucleus accumbens core and shell in incentive-cue responding and behavioral inhibition. *J Neurosci* 31:6820-6830.
- Britt, J.P., Benaliouad, F., McDevitt, R.A., Stuber, G.D., Wise, R.A., and Bonci, A. (2012) Synaptic and behavioral profile of multiple glutamatergic inputs to the nucleus accumbens. *Neuron* 76:790-803.
- Brodnik, Z.D., and Espana, R.A. (2015) Dopamine uptake dynamics are preserved under isoflurane anesthesia. *Neurosci Lett* 606:129-134.
- Carlezon, W.A., Jr., and Thomas, M.J. (2009) Biological substrates of reward and aversion: a nucleus accumbens activity hypothesis. *Neuropharmacology* 56 Suppl 1:122-132.
- Conover, K.L., and Shizgal, P. (1994) Competition and summation between rewarding effects of sucrose and lateral hypothalamic stimulation in the rat. *Behav Neurosci* 108:537-548.
- Cossette, M.P., Conover, K., and Shizgal, P. (2015) The neural substrates for the rewarding and dopamine-releasing effects of medial forebrain bundle stimulation have partially discrepant frequency responses. *Behav Brain Res*.
- Cox, R.W. (1996) AFNI: software for analysis and visualization of functional magnetic resonance neuroimages. *Comput Biomed Res* 29:162-173.
- Doya, K. (2008) Modulators of decision making. *Nat Neurosci* 11:410-416.
- Gallistel, C.R. (1978) Self-stimulation in the rat: quantitative characteristics of the reward pathway. *J Comp Physiol Psychol* 92:977-998.
- Gallistel, C.R., and Leon, M. (1991) Measuring the subjective magnitude of brain stimulation reward by titration with rate of reward. *Behav Neurosci* 105:913-925.
- Gallistel, C.R., Shizgal, P., and Yeomans, J.S. (1981) A portrait of the substrate for self-stimulation. *Psychol Rev* 88:228-273.
- Garris, P.A., Kilpatrick, M., Bunin, M.A., Michael, D., Walker, Q.D., and Wightman, R.M. (1999) Dissociation of dopamine release in the nucleus accumbens from intracranial self-stimulation. *Nature* 398:67-69.

- Green, L., and Rachlin, H. (1991) Economic substitutability of electrical brain stimulation, food, and water. *J Exp Anal Behav* 55:133-143.
- Hariri, A.R., Brown, S.M., Williamson, D.E., Flory, J.D., de Wit, H., and Manuck, S.B. (2006) Preference for immediate over delayed rewards is associated with magnitude of ventral striatal activity. *J Neurosci* 26:13213-13217.
- Herrnstein, R.J. (1970) On the law of effect. *J Exp Anal Behav* 13:243-266.
- Ikemoto, S., and Wise, R.A. (2004) Mapping of chemical trigger zones for reward. *Neuropharmacology* 47 Suppl 1:190-201.
- Kilpatrick, M.R., Rooney, M.B., Michael, D.J., and Wightman, R.M. (2000) Extracellular dopamine dynamics in rat caudate-putamen during experimenter-delivered and intracranial self-stimulation. *Neuroscience* 96:697-706.
- Kim, K.M., Baratta, M.V., Yang, A., Lee, D., Boyden, E.S., and Fiorillo, C.D. (2012) Optogenetic mimicry of the transient activation of dopamine neurons by natural reward is sufficient for operant reinforcement. *PLoS One* 7:e33612.
- Knutson, B., and Gibbs, S.E. (2007) Linking nucleus accumbens dopamine and blood oxygenation. *Psychopharmacology (Berl)* 191:813-822.
- Krautwald, K., Min, H.K., Lee, K.H., and Angenstein, F. (2013) Synchronized electrical stimulation of the rat medial forebrain bundle and perforant pathway generates an additive BOLD response in the nucleus accumbens and prefrontal cortex. *Neuroimage* 77:14-25.
- Kringelbach, M.L. (2005) The human orbitofrontal cortex: linking reward to hedonic experience. *Nat Rev Neurosci* 6:691-702.
- Kringelbach, M.L., and Berridge, K.C. (2009) Towards a functional neuroanatomy of pleasure and happiness. *Trends Cogn Sci* 13:479-487.
- Lee, A.T., Glover, G.H., and Meyer, C.H. (1995) Discrimination of large venous vessels in time-course spiral blood-oxygen-level-dependent magnetic-resonance functional neuroimaging. *Magn Reson Med* 33:745-754.
- Lee, T., Cai, L.X., Lelyveld, V.S., Hai, A., and Jasanoff, A. (2014) Molecular-level functional magnetic resonance imaging of dopaminergic signaling. *Science* 344:533-535.
- Logothetis, N.K. (2002) The neural basis of the blood-oxygen-level-dependent functional magnetic resonance imaging signal. *Philos Trans R Soc Lond B Biol Sci* 357:1003-1037.
- Logothetis, N.K., Pauls, J., Augath, M., Trinath, T., and Oeltermann, A. (2001) Neurophysiological investigation of the basis of the fMRI signal. *Nature* 412:150-157.

- Mark, T.A., and Gallistel, C.R. (1993) Subjective reward magnitude of medial forebrain stimulation as a function of train duration and pulse frequency. *Behav Neurosci* 107:389-401.
- McClure, S.M., Berns, G.S., and Montague, P.R. (2003) Temporal prediction errors in a passive learning task activate human striatum. *Neuron* 38:339-346.
- McClure, S.M., Ericson, K.M., Laibson, D.I., Loewenstein, G., and Cohen, J.D. (2007) Time discounting for primary rewards. *J Neurosci* 27:5796-5804.
- McClure, S.M., Laibson, D.I., Loewenstein, G., and Cohen, J.D. (2004) Separate neural systems value immediate and delayed monetary rewards. *Science* 306:503-507.
- Miliaressis, E., Emond, C., and Merali, Z. (1991) Re-evaluation of the role of dopamine in intracranial self-stimulation using in vivo microdialysis. *Behav Brain Res* 46:43-48.
- Murray, E.A., O'Doherty, J.P., and Schoenbaum, G. (2007) What we know and do not know about the functions of the orbitofrontal cortex after 20 years of cross-species studies. *J Neurosci* 27:8166-8169.
- Nicola, S.M., Yun, I.A., Wakabayashi, K.T., and Fields, H.L. (2004) Firing of nucleus accumbens neurons during the consummatory phase of a discriminative stimulus task depends on previous reward predictive cues. *J Neurophysiol* 91:1866-1882.
- Nieh, E.H., Kim, S.Y., Namburi, P., and Tye, K.M. (2013) Optogenetic dissection of neural circuits underlying emotional valence and motivated behaviors. *Brain Res* 1511:73-92.
- Norris, D.G. (2012) Spin-echo fMRI: The poor relation? *Neuroimage*.
- O'Doherty, J.P., Dayan, P., Friston, K., Critchley, H., and Dolan, R.J. (2003) Temporal difference models and reward-related learning in the human brain. *Neuron* 38:329-337.
- Olds, J., and Milner, P. (1954) Positive reinforcement produced by electrical stimulation of septal area and other regions of rat brain. *J Comp Physiol Psychol* 47:419-427.
- Paxinos, G. (2004) *The Rat Nervous System*, 3 edn (New York: Academic Press).
- Paxinos, G., and Watson, C. (1998) *The Rat Brain in Stereotaxic Coordinates*, 4th edn (New York: Academic Press).
- Roitman, M.F., Wheeler, R.A., and Carelli, R.M. (2005) Nucleus accumbens neurons are innately tuned for rewarding and aversive taste stimuli, encode their predictors, and are linked to motor output. *Neuron* 45:587-597.
- Saddoris, M.P., Cacciapaglia, F., Wightman, R.M., and Carelli, R.M. (2015) Differential Dopamine Release Dynamics in the Nucleus Accumbens Core and Shell Reveal

- Complementary Signals for Error Prediction and Incentive Motivation. *J Neurosci* 35:11572-11582.
- Schultz, W. (2000) Multiple reward signals in the brain. *Nat Rev Neurosci* 1:199-207.
- Schultz, W. (2015) Neuronal Reward and Decision Signals: From Theories to Data. *Physiol Rev* 95:853-951.
- Setlow, B., Schoenbaum, G., and Gallagher, M. (2003) Neural encoding in ventral striatum during olfactory discrimination learning. *Neuron* 38:625-636.
- Simmons, J.M., and Gallistel, C.R. (1994) Saturation of subjective reward magnitude as a function of current and pulse frequency. *Behav Neurosci* 108:151-160.
- Smith, K.S., Berridge, K.C., and Aldridge, J.W. (2011) Disentangling pleasure from incentive salience and learning signals in brain reward circuitry. *Proc Natl Acad Sci U S A* 108:E255-264.
- Sonnenschein, B., Conover, K., and Shizgal, P. (2003) Growth of brain stimulation reward as a function of duration and stimulation strength. *Behav Neurosci* 117:978-994.
- Sutton, R.S., and Barto, A.G. (1981) Toward a modern theory of adaptive networks: expectation and prediction. *Psychol Rev* 88:135-170.
- Taha, S.A., and Fields, H.L. (2005) Encoding of palatability and appetitive behaviors by distinct neuronal populations in the nucleus accumbens. *J Neurosci* 25:1193-1202.
- Tepper, J.M., Creese, I., and Schwartz, D.H. (1991) Stimulus-evoked changes in neostriatal dopamine levels in awake and anesthetized rats as measured by microdialysis. *Brain Res* 559:283-292.
- Wang, K., van Meer, M.P., van der Marel, K., van der Toorn, A., Xu, L., Liu, Y., Viergever, M.A., Jiang, T., and Dijkhuizen, R.M. (2011) Temporal scaling properties and spatial synchronization of spontaneous blood oxygenation level-dependent (BOLD) signal fluctuations in rat sensorimotor network at different levels of isoflurane anesthesia. *NMR Biomed* 24:61-67.
- Witten, I.B., Steinberg, E.E., Lee, S.Y., Davidson, T.J., Zalocusky, K.A., Brodsky, M., Yizhar, O., Cho, S.L., Gong, S., Ramakrishnan, C., *et al.* (2011) Recombinase-driver rat lines: tools, techniques, and optogenetic application to dopamine-mediated reinforcement. *Neuron* 72:721-733.

Chapter 3

Dissociable processing of rewarding and aversive stimuli in rats

The text of this chapter was written by Sarah Bricault and Alan Jasanoff. I contributed to the collection of all data except the MFB imaging data (collected by Ana Fiallos) and a few of the dlPAG imaging datasets (collected by Mitul Desai and Tehya Johnson). All analyses presented here were performed by me, and I directly supervised the behavioral and surgical work of undergrads Jiyoung Lee, Elizabeth DeTienne, Cortni Dick, Hermoon Worku, and Jean Chow.

Dissociable processing of rewarding and aversive stimuli in rats

Sarah Bricault¹, Mitul Desai², Tehya Johnson², Jiyoung Lee³, Elizabeth DeTienne⁴, Cortni Dick², Hermoon Worku¹,
Jean Chow⁵, Ana Fiallos⁵, & Alan Jasanoff^{2,5,6*}

¹ Department of Biology, Massachusetts Institute of Technology

² Department of Biological Engineering, Massachusetts Institute of Technology

³ Department of Neuroscience, Wellesley College

⁴ Department of Electrical Engineering & Computer Science,
Massachusetts Institute of Technology

⁵ Department of Brain & Cognitive Sciences, Massachusetts
Institute of Technology

⁶ Department of Nuclear Science & Engineering, Massachusetts Institute of
Technology

* Address correspondence to AJ

phone: 617-452-2538

e-mail: jasanoff@mit.edu

Principal abbreviations: Dorsolateral Periaqueductal Gray (dlPAG), Functional Magnetic Resonance Imaging (fMRI), Insular Cortex (ICx), Medial Forebrain Bundle (MFB), Nucleus Accumbens (NAc), Region of Interest (ROI), Ventral Tegmental Area (VTA)

Abstract

Classical psychological and economic theories posit that we choose actions to maximize rewards and minimize penalties, without a fundamental distinction between opposite valences. This would require neural mechanisms to integrate appetitive and aversive stimuli into a shared representation of value in the brain. Here we characterize a pair of rewarding and aversive stimuli that fail strikingly to combine in this way. Electrical microstimulation of the medial forebrain bundle (MFB) and dorsolateral periaqueductal gray (dlPAG) produce robust approach and avoidance behaviors, respectively. We show however that concurrent delivery of the aversive dlPAG input produces no change in the psychometric value of operant responses to rewarding MFB stimulation in a simple decision making task. Conversely, co-delivery of rewarding stimulation fails to modulate quantitative assessments of avoidance behavior evoked by the aversive input. To examine the neural basis for this dissociation, we performed functional magnetic resonance imaging on animals undergoing dlPAG or MFB stimulation. We found that dlPAG input evokes sparse peaks of activity, notably in insular cortex, but that overlap between structures activated by rewarding and aversive stimulation are minimal. The lack of shared neural responses provides a plausible explanation for the behavioral dissociability of dlPAG and MFB stimuli and challenges the idea that reward and aversion must provide a common currency for guiding decisions.

Significance statement

This work demonstrates that rewarding and aversive stimuli can alter behavior through dissociable mechanisms that do not yield combined estimates of action value. Our results also

reveal distinct brain structures activated by stimuli of opposite valence. These findings counter the prevailing view of reward and aversion as two sides of the same coin, and suggest a distinction between forms of aversive input that can elicit avoidance versus those that alter motivation. In addition to its significance for scientific understanding of the neural mechanisms of motivated behavior, this study has implications for the treatment of affective disorders in the clinic.

Introduction

Actions are often motivated by rewarding or aversive stimuli. Rewards positively reinforce behavior, increasing the likelihood of future performance and usually eliciting hedonic pleasure in the process. Aversive stimuli evoke avoidance behavior and generally induce affective responses associated with displeasure or disgust. Traditional conceptions of optimal decision making dictate that agents should choose actions that maximize the predicted net value of the consequences (von Neumann and Morgenstern, 1944; Kahneman and Tversky, 1979; Sutton and Barto, 1998). In order to implement such strategies, animals must possess neural mechanisms that evaluate stimuli of arbitrary valence and associate them with antecedent actions (Levy and Glimcher, 2012). This requires that information about rewards and penalties converge on distinct neural structures or cell populations in such a manner that the two stimulus modalities can exert competing effects on the probabilities of subsequent behavioral patterns (Bissonette et al., 2014; Hayes et al., 2015).

Possible sites for convergence of rewarding and aversive input have been defined by previous studies (Carlezon and Thomas, 2009; Nieh et al., 2013; Hu, 2016). Considerable attention has focused on the mesocorticolimbic dopamine system, which transmits information about predicted and unexpected rewards to corticostriatal circuitry involved in action selection (Lammel et al., 2014). Aversive stimuli also affect dopamine signaling in striatal targets such as the nucleus

accumbens (NAc), but the significance of these responses is not yet understood. Although aversive input can suppress dopamine neuron firing in the ventral tegmental area (VTA) (Mirenowicz and Schultz, 1996; Lammel et al., 2012), several reports have also documented aversion-related elevations of dopamine release, possibly arising from the rewarding consequences of terminating unpleasant stimuli (Lammel et al., 2014). Additional sites where responses to both rewarding and aversive stimuli have been documented prominently include regions of the amygdala (Amyg) (Maren, 2016), whose role in fear and aversion is best characterized, and the medial prefrontal cortex (Weele et al., 2019), whose function has been associated with pleasure and satiety. Whether any or all of these sites are involved in integration of rewarding and aversive stimuli to yield effective action values is unclear, however.

One way to screen the brain for neural populations involved in value computation is to apply brain-wide functional imaging in conjunction with behavioral measures of net reward magnitude. Such approaches have been applied to identify reward and punishment-sensitive regions of the human brain (Delgado et al., 2000; O'Doherty et al., 2001; Basten et al., 2010; Aupperle et al., 2015), as well as reward-tracking neural populations in the rodent brain (Fiallos et al., 2017). Although human studies offer the obvious advantages of facile behavioral control and the possibility of obtaining subjective reports, the appetitive and aversive elements used in human studies are usually conditioned stimuli with indirect relevance to innate motivational drives. More direct intervention into motivational systems is possible in animals, where centrally acting rewarding and aversive stimuli may be rigorously assessed in behavioral tests and imaging-based findings subsequently evaluated using invasive measures or perturbations.

To exploit these advantages while exploring the integration of aversive and rewarding inputs, we applied fMRI in rats during application of stimuli whose effects could be psychometrically

quantified in parallel behavioral assessments. For this study, we chose to combine electrical microstimulation of two targets—the medial forebrain bundle (MFB) and dorsolateral periaqueductal gray (dlPAG)—shown previously to underlie robust approach and avoidance behavior, respectively (Olds and Milner, 1954; Vianna et al., 2001). The use of electrical stimuli facilitates parametric variation of input intensity in awake behaving animals, as well as during fMRI experiments that require sedation. In implementing this design, we observed that the positive and negative stimuli we chose show no evidence of interaction in quantitative behavioral assessments, and that they also fail to co-activate common neural structures. Our results therefore describe a dissociation of reward and aversion processing on both behavioral and neurophysiological levels.

Materials and Methods

Animals

All animal procedures were performed in strict compliance with US Federal guidelines, with oversight by the MIT Committee on Animal Care. Male Sprague-Dawley rats (250-400g), purchased from Charles River Laboratories (Wilmington, MA) were used for the data presented in this paper. The animals were housed and maintained on a 12 h light/dark cycle with ad libitum access to food and water.

Surgical procedures

In preparation for imaging or behavioral experiments, rats were implanted with bipolar stimulation electrodes targeted at MFB and/or dlPAG. Animals were anaesthetized with 2%

isoflurane, shaved, and mounted in a rodent stereotaxic device (David Kopf Instruments, Tujunga, CA). Heart rates and blood oxygenation levels were monitored by a pulse oximeter (Nonin Medical, Plymouth, MN). The scalp was retracted and 28G holes were drilled into the skull at the appropriate coordinates relative to bregma (MFB -3.9 AP, -1.7 ML, -8.6 DV; dlPAG -7.2 AP, -2.2 ML, -4.7 DV, with the electrode oriented at a 16 degree angle from vertical). These coordinates were based on a standard rat brain atlas (Paxinos and Watson, 1997). The stimulation electrodes were implanted and secured using C&B Metabond dental cement (Parkell, Edgewood, NY). Small plastic head-posts were implanted to facilitate head fixation during the MRI experiments. Each rat was given a subcutaneous injection of buprenorphine (MIT pharmacy) at a dose of 0.01 mg/kg for analgesia at the end of surgery, and once a day for two days following surgery. Rats were allowed to recover from surgery for at least three days before behavioral testing began.

Establishing dlPAG behavioral thresholds

Historically, dlPAG freezing and escape thresholds have been established by slowly increasing the stimulation current until the relevant behavior is observed. However, this is problematic for several reasons. First, the thresholds vary by animal as a result of electrode placement and individual animal variability. The amount of tissue activated by stimulation is directly related to the amount of current injected. As we were specifically interested in the brain structures activated by the stimulation, we didn't want the confound of differing stimulation volumes as we increased the strength of the stimulation. Furthermore, with our setup it was substantially easier to programmatically control stimulation frequency than it was to control the current. Thus, we established the following protocol. We termed this the *increasing frequency* method to distinguish it from the standard *increasing current* method.

First, we performed the standard increasing current method on day 1 to establish freezing and escape thresholds (with the frequency set to the standard 60 Hz). Then, we set the current to the freezing threshold established on day 1 and slowly increased the frequency until freezing and then escape behaviors were observed. There were no visible differences in the behaviors induced by the increasing frequency method and those induced by the increasing current method. We performed this behavioral testing every day until we obtained consistent thresholds (within 5 Hz) over two consecutive days.

For a subset of animals, we established thresholds in this way for four days, and then retested the thresholds using the standard increasing current method to verify that they had remained unchanged. Indeed, we found that the current thresholds did not exhibit much variance from their day 1 values.

Constant sub-threshold dlPAG stimulation

Six rats were monitored during two 13-minute periods on different days. For both sessions, the animals had their dlPAG electrodes hooked up to a commutator that allowed them to rotate freely and were placed within a behavioral box (8"x10"x7") that was itself placed in a dimly lit, soundproof chamber. The animals were allowed to acclimate for five minutes before the official monitoring period began. During one of the experiments, current was constantly injected into the dlPAG electrodes at 60 Hz and 90% of the given animal's freezing threshold. During the other, control experiment no current was injected. Video was collected during both sessions, and the videos were later manually scored for three behaviors. A rearing action was defined as any time both forepaws left the floor of the chamber without grooming behavior being present. A cage crossing was defined as any time the animal's haunches fully crossed from one side of the chamber

to the other, along the axis captured by the camera. Both the length of grooming sessions and the total number of grooming sessions were recorded.

MFB self-stimulation behavior

All animals implanted with MFB electrodes underwent testing to determine the threshold for current stimulation that would induce reward-seeking behavior. Animals were placed in a two-choice behavioral box (8"x10"x7") within an unlit, soundproofed container. The behavioral box contained two holes with infrared sensors at approximately face height for the rats, termed nosepoke holes. The animal was given a minimum of five minutes to acclimate to the box. At that point, a green LED was activated, indicating that the nosepoke holes were active. During an active period, the animal could poke in either hole to receive a rewarding stimulation of the MFB at 150 Hz for 3 s with a 0.1 ms pulse width. The current was slowly raised from .01 mA until the animal exhibited reliable poking behavior without severe motor artifacts caused by the stimulation. Once the animal began poking reliably (>2 pokes/min), a training session was initiated in which the animal was left in the behavioral box for a 30 min active period during which poking in either hole resulted in a 150 Hz reward.

On the day following the training session, the animal was placed back in the box and its ability to discriminate between rewards of different values was assessed. Poking in one hole resulted in a stimulation at the reference frequency of 150 Hz. Poking in the other resulted in stimulation at the variable frequency (25, 50, 100, or 150 Hz). Each trial lasted 10 minutes and the mapping of the holes swapped halfway through the session to prevent spatial bias, resulting in a total test time of 40 min.

Combined dIPAG and MFB behavioral tests

Once the dIPAG and MFB electrodes were tested independently and the stimulation thresholds were established, the combined behavioral tasks were performed. The animal was placed in a behavioral box containing two nosepoke holes (X and Y) and was allowed to acclimate for 5 minutes. Once the acclimation was completed, a green LED was activated to indicate the nosepoke holes were active. Only one behavioral test was performed on any given day. All trials were presented in pseudorandom order. All stimuli were presented for 3 seconds, and had a pulse width of 0.1 milliseconds. A variety of different stimulus combinations were applied:

(1) *SIDE X: 150Hz MFB, SIDE Y: 150Hz MFB & variable dIPAG.* Poking in one hole resulted in a stimulation of MFB at the reference frequency of 150 Hz. Poking in the other resulted in stimulation of MFB at the reference frequency 150 Hz and stimulation of dIPAG at a variable frequency. Each trial lasted 10 minutes and the mapping of the holes was swapped halfway through the session to prevent spatial bias, resulting in a total test time of 40 min. The dIPAG frequency was calculated individually based on each animal's freezing (F) and escape (E) thresholds. The dIPAG stimulation values were F , $F+0.25*(E-F)$, $F+0.5*(E-F)$, and $F+0.75*(E-F)$.

(2) *SIDE X: 100Hz MFB, SIDE Y: 100Hz MFB & variable dIPAG.* This was identical to the experiment described above, except that the MFB stimulation was 100 Hz.

(3) *SIDE X: variable MFB, SIDE Y: variable MFB & F dIPAG.* Poking in one nosepoke hole resulted in stimulation of the MFB at 50, 100, or 150 Hz. Poking in the other resulted in an identical MFB stimulation accompanied by dIPAG stimulation at the freezing threshold.

(4) *SIDE X: 150Hz MFB with var. delay, SIDE Y: 150Hz MFB with var. delay & $F + 0.5*(E-F)$ dlPAG.* Poking in one nosepoke hole resulted in stimulation of the MFB at 150 Hz with a delay that varied between 0, 200, and 400 ms. Poking in the other resulted in an identical MFB stimulation plus a dlPAG stimulation halfway between the freezing and escape thresholds.

(5) *SIDE X: 150Hz MFB, SIDE Y: 150Hz MFB & $F + 0.5*(E-F)$ dlPAG with var. delay*

Poking in one nosepoke hole resulted in stimulation of the MFB at 150 Hz. Poking in the other resulted in an identical MFB stimulation plus a dlPAG stimulation halfway between the freezing and escape thresholds with a delay that varied between 0, 200, and 400 ms.

(6) *dlPAG escape threshold determination with contingent MFB stimulation.* Animals were placed in the same behavioral box that was used to determine the dlPAG escape thresholds initially (a different apparatus from the two-choice box). The escape thresholds were established as described earlier, except that when the current was delivered to the dlPAG, the MFB was also stimulated at 150 Hz for 3 s.

fMRI data acquisition

Immediately prior to imaging experiments, rats were anesthetized using 3% isoflurane and maintained at 2% isoflurane during preparation. Animals were intubated and ventilated, and an intraperitoneal catheter was established for drug delivery. Animals were then placed onto a cradle and secured in place via screws that attached to the implanted headpost. Isoflurane was reduced to 0.75% and 1 mg/kg pancuronium (Sigma-Aldrich) was administered, followed by continuous delivery of 2 mg/kg/h pancuronium thereafter. Respiration, heart rate, and blood oxygen saturation

were monitored, and temperature was maintained with a circulating warm water pad (Gaymar, Orchard Park, NY) for the remainder of the procedure.

In vivo imaging in conjunction with stimulation of dlPAG was performed using a 7 Tesla Biospec MRI scanner (Bruker) scanner operating with a cross coil volume transmit, surface receive configuration. A rapid acquisition with refocused echoes (RARE) pulse sequence were used to acquire T_2 -weighted anatomical images, with number of averages (NA) = 4, matrix size = 256×192 , FOV = $2.5 \text{ cm} \times 2.5 \text{ cm}$, slice thickness = 1 mm, effective TR = 5000 ms, effective TE = 30 ms, and RARE factor = 8. For functional imaging, echo planar imaging (EPI) image series were acquired during alternating blocks of intracranial stimulation and rest. EPI scan parameters were NA = 1, matrix size = 64×64 , FOV = $2.5 \text{ cm} \times 2.5 \text{ cm}$, slice thickness = 1 mm, TR = 2000 ms, and effective TE = 15 ms. Intracranial stimulation of the dlPAG was performed using 60 Hz pulse trains with 0.2 ms pulse width and current set to 90% of the behaviorally-established freezing threshold. dlPAG stimulation blocks were 16 s long, and were delivered in 28 cycles with 10 s rest periods in between.

Functional neuroimaging experiments performed with MFB stimulation have been previously described (Fiallos et al., 2017). MRI scans were obtained using a 4.7 T 40 cm horizontal-bore magnet interfaced to a Bruker (Billerica, MA) Avance console and equipped with a 12 cm gradient set (26 G/cm). A transmit-only 10 cm inner diameter volume coil and a customized ~ 2 cm diameter receive-only surface coil (Ekam Imaging), both integrated into the animal positioning device, were used for excitation and detection. Pulse sequences were controlled through the Para-vision 3.0 software (Bruker). For functional imaging with blood oxygenation level dependent (BOLD) contrast, a single-shot gradient echo echo planar imaging (EPI) pulse sequence was used with an echo time (TE) of 20 ms, recycle time (TR) of 2 s, slice thickness of 1

mm (14-16 slices centered over bregma), in-plane field of view 3.2 x 2.4 cm, and matrix size 64 x 48 points.

fMRI data analysis

Images were reconstructed with Paravision software (Bruker) or MATLAB and analyzed using AFNI (Cox, 1996) and custom MATLAB (Mathworks) routines. Preprocessing steps for the EPI data included removal of signal outside the brain, alignment to the anatomical scans using AFNI's 3dAllineate, motion correction using AFNI's 3dvolreg, spatial smoothing to 1.5 mm full width at half maximum using AFNI's 3dBlurToFWHM, voxel-wise signal detrending and intensity normalization, and temporal smoothing using a sliding window of width 6s (3 scans).

To generate the map of signal change as a result of the stimulus in Fig. 2a and Fig. 5a, the impulse response function (IRF) was generated for the concatenated dataset using AFNI's 3dDeconvolve, with six motion regressors. The signal from three timepoints (6 s) of the IRF starting approximately six seconds after the stimulus onset were averaged together for each voxel and defined to be the stimulus "ON" condition. The signal from three baseline timepoints of the IRF were averaged together for each voxel and defined to be the stimulus "OFF" condition. The stimulus OFF was subtracted from the stimulus ON to get the percent signal change per voxel. This analysis was done and statistics generated using the jackknife method. All voxels that passed the $p < 0.05$ threshold (student's t-test) are displayed. There were eleven animals used in the dIPAG analysis and eight used in the MFB analysis.

Graphs of fMRI responses as a function of time were generated similarly. Instead of generating the map per voxel, the IRF from all voxels that fell into the relevant region of interest

(ROI) as defined with respect to the brain atlas and were present in all individual animal datasets were averaged together to produce an average ROI IRF. To get the standard error (gray shaded region around the curves), the jackknife procedure was used. To generate ROI averages, IRFs were calculated for each region, and then the percent signal change was calculated as for the maps. The error bars represent the standard error of the mean, calculated using the jackknife method.

Results

Rats were implanted with bipolar electrodes targeting dlPAG and aversive responses to stimulation were evaluated using a variety of behavioral measures. Stimulus effects were quantified by determining the minimum currents required to induce stereotypical avoidance behaviors (Fig. 1b) (Brandao et al., 1982). In each of 10 animals, a threshold current of 0.133 ± 0.042 mA was sufficient to induce defensive freezing, while the threshold current of 0.166 ± 0.047 mA induced vigorous escape efforts. Stimulation at 90% of the freezing threshold for each animal also produced measurable depressive effects. In an open cage test, we observed reductions by over 50% in the number of cage crossings, the number of rearings, and the number of grooming sessions and time spent grooming (Fig. 1c,d). The effects on cage crossing and grooming were statistically significant with *t*-tests $p \leq 0.005$ and $p \leq 0.05$, respectively.

To determine which brain regions are most strongly engaged by aversive input delivered via the dlPAG, eleven animals were sedated after behavioral testing and stimulated using 90% of their individually-determined freezing thresholds during acquisition of fMRI scan series. This protocol reveals stimulus-associated blood oxygen level-dependent (BOLD) responses in a sparse set of structures (Fig. 2a). When averaged across anatomically defined regions of interest (ROIs), the only statistically significant effects were observed in the insular cortex (ICx) (Fig. 2b-e), an area

recently identified by another study as a site of aversive stimulus processing (Gehrlach et al., 2019). Lack of consistent activation of other brain regions previously implicated in processing aversive input (Carlezon and Thomas, 2009; Nieh et al., 2013; Hu, 2016) suggests that robust activation of these structures is not required for avoidance behavior evoked by dlPAG stimulation.

Rewarding electrical microstimulation of the MFB provides a well-characterized counterpoint to the aversive input provided by dlPAG stimulation. To examine potential interactions between these two stimuli, six rats were doubly implanted with electrodes targeting both regions. Animals were initially assessed for their ability to distinguish rewards of different magnitudes in a simple two-choice decision task (Fig. 3a) (Gallistel and Leon, 1991). Each animal was placed in a box with two nose-poke holes; poking in one hole elicited a fixed 150 Hz MFB stimulus, while poking in the other hole elicited a stimulus that ranged in frequency from 25 to 150 Hz across trials (Fig. 3b). All animals reliably apportioned nose-pokes between the two holes such that more responses were delivered to the operant associated with greater frequency (*t*-test $p \leq 0.005$ for 25 Hz, $p \leq 0.0001$ for 50 Hz, and $p \leq 0.001$ for 100 Hz) and equal response rates were observed when the two stimulation intensities were equal (52.56 ± 1.96 %, *t*-test $p = 0.249$ when compared to 50%).

We reasoned that a reward delivered simultaneously with an aversive stimulus would have lesser psychometric value than the same reward delivered by itself; if this were true, the two-choice behavioral test should be able to measure this effect. To evaluate this hypothesis, we paired 150 Hz MFB stimulation with dlPAG stimulation offered at four frequency levels ranging from the freezing threshold to 75% of the difference between the freezing and escape threshold. We then compared responses at a nose-poke hole associated with these stimulus combinations to responses at a hole associated with 150 Hz MFB stimulation alone (Fig. 3c). Remarkably, the rates of

responses at the two operants were identical (49.65 +/- 2.38 %, *t*-test *p* = 0.89 for A1; 48.05 +/- 1.33 %, *t*-test *p* = 0.20 for A2; 50.08 +/- 3.04 %, *t*-test *p* = 0.98 for A3; 48.07 +/- 2.13 %, *t*-test *p* = 0.42 for A4; all *t*-tests with respect to 50 %), regardless of the amplitude of concurrent dIPAG stimulation. We performed the same test using 100 Hz MFB stimulation delivered alone versus in combination with dIPAG stimuli and observed the same result. We also compared rewards offered at three frequencies alone versus in combination with dIPAG stimulation at the freezing threshold and again found that rats did not distinguish between operants associated with the two outcomes (*t*-test *p* = 0.89 for 150 Hz MFB; *t*-test *p* = 0.42 for 100 Hz MFB; *t*-test *p* = 0.74 for 50 Hz MFB; anecdotally the same result holds for 25 Hz MFB stimulation, but poking rates were negligible). Finally, we investigated whether concurrent delivery of rewarding MFB stimulation alters the current threshold for active avoidance of aversive dIPAG input (Fig. 3d). In six tested animals, no consistent effect was found (*t*-test *p* = 0.94), showing that behavioral effects of dIPAG and MFB stimulation are quantitatively independent.

The failure of aversive dIPAG stimulation to alter the relative operant response rates of animals receiving MFB stimulation could reflect differences in the time course with which MFB and dIPAG stimuli affect neural circuitry and behavior. To probe this possibility, we varied the relative onset time of MFB *vs.* dIPAG stimulation following instrumental responses at nose-poke holes in the two-choice test (Fig. 4). Even with staggered presentation of the two stimuli by delays of up to 400 ms, however, performance remained consistent in two tested animals, with aversive dIPAG stimulation having negligible effect on the apparent value of the operants.

The striking dissociation between effects of MFB and dIPAG stimulation shows that appetitive and aversive stimuli do not necessarily interact to influence approach and avoidance propensities. A possible mechanistic explanation for this result is that the two stimuli engage

separate, non-interacting components of neural circuitry, each of which mediates behavioral responses specific to the respective stimulus. To examine this possibility, we compared the profile of brain activity evoked by dlPAG stimulation to analogous fMRI responses elicited by MFB stimulation across a range of intensities (Fig. 5a) (Fiallos et al., 2017). Unlike the aversive stimulus, rewarding microstimulation evokes strong responses across many regions (Fig. 5b,c), prominently including VTA (0.763 ± 0.244 %) and NAc (0.729 ± 0.251 %), where the error bars represent standard error of the mean. A direct comparison of BOLD response amplitudes observed in the aversive and rewarding stimulation experiments indicates that ROIs most reliably activated by dlPAG input are among those least influenced by MFB stimulation.

Discussion

Our results thus characterize a pair of rewarding and aversive stimuli that produce dissociable effects on behavior and underlying neurophysiology. We verify that electrical microstimulation of dlPAG induces robust avoidance, but that it fails to alter psychometric reward values measured in a two-choice operant task. We also find that rewarding MFB stimulation fails to increase the current threshold for aversive effects of dlPAG input. The fact that the two stimuli fail to coactivate structures in the brain provides a possible explanation for their inability to yield a combined representation of net value that guides the behaviors we examined. Although our experiments were undertaken using electrical stimuli that artificially engage neural circuitry, the results are informative in several respects that generalize to naturalistic paradigms.

The failure of rewarding and aversive stimuli to exert integrated effects on the apparent value of choices in the decision task we applied contrasts with a number of previous findings. Studies of human decision making have found that subjects discount rewarding choices when they are

coupled to the threat of punishment (Sierra-Mercado et al., 2015; Bublatzky et al., 2017). In animal studies, pairing or alternating rewards with penalties has also been shown to decrease appetitive responses (Carelli and West, 2014; Piantadosi et al., 2017), although a previous study that applied MFB and dlPAG microstimulation together also observed dominance of individual modalities in approach/avoidance conflict tasks (Valenstein, 1965). The inability of these stimuli to interact suggests that they probe orthogonal psychological components. MFB stimulation reward has long been thought to manipulate motivation without eliciting hedonic aspects of reward (Berridge and Valenstein, 1991). Stimulation of dlPAG produces unambiguous avoidance responses, and has previously been shown to promote conditioned fear (Di Scala et al., 1987), but our experiments show that these effects are not sufficient to alter preferences in a decision task. Although dlPAG input “motivates” escape behavior, this may constitute a reflexive effect that does not enable arbitrary actions to be reinforced. In this light, our findings provide further support for distinctions among different forms of aversion (Rudebeck et al., 2006) and between emotional and motivational processes (Berridge, 2018).

At a neurophysiological level, an obvious difference between prior studies of conflicting stimuli and our own is that our experiments employed invasive brain perturbations to induce rewarding and aversive effects. It is possible that electrical dlPAG and MFB stimuli bypass or override the neural mechanisms that enable natural or conditioned positive and negative stimuli to modulate one another. On the other hand, both stimuli induce responses characteristic of natural reinforcers in conditioning tests (Di Scala et al., 1987; Wise, 2005), and MFB input in particular has been shown to substitute for food and water rewards in operant tasks (Green and Rachlin, 1991). This indicates that the stimuli interact substantially with the neural circuitry that supports ethologically relevant reward and aversion.

The neuroimaging experiments we performed demonstrate that the two stimuli differ sharply in the patterns of brain activation they elicit, however. While dlPAG stimulation induces focal responses in a small number of areas, most prominently including ICx, MFB stimulation activated a broad range of structures including NAc and VTA. Notably, we did not observe shared activation of mesolimbic structures previously shown to receive both appetitive and aversive input in some contexts (Carlezon and Thomas, 2009; Nieh et al., 2013; Hu, 2016). The absence of shared activation of NAc is particularly striking, given recent evidence for convergence of stimuli with opposite valence to this area (de Jong et al., 2019). Although it is possible that anesthesia used in our imaging experiments contributed to these results, the absence of areas of co-activation is consistent with our behavioral findings, and seems to rule out the possibility that specific brain regions are involved in computing a unified representation of net value under our conditions. Our results may also be consistent with the hypothesis that engagement of mesolimbic structures in both reward and aversion may have more to do with the salience of the stimuli involved than with the representation of value *per se* (Berridge, 2018).

Results of our study have a number of broader implications. Disorders of reward and aversion processing affect millions of patients worldwide, and potential therapies include pharmacological treatments (VanElzakker et al., 2014; Volkow et al., 2019) and deep brain stimulation methods targeting some of the structures that figure in our fMRI analysis (Denys et al., 2010; Luigjes et al., 2012; Nauczyciel et al., 2013; Ibrahim et al., 2019). Our findings suggest a basis for distinct affective responses obtained through intervention in neural structures engaged by the rewarding and aversive stimuli we applied. At the same time, our study highlights the need for nuance in interpreting the nature of rewards and punishments themselves. The dissociable rewarding and aversive stimuli we used clearly operate differently from positive and negative reinforcers that

genuinely do interact in behavior. Such distinctions may apply to the variety of natural and artificial therapeutic approaches used for instance in treatment of drug abuse and post-traumatic stress disorders (VanElzakker et al., 2014; Volkow et al., 2019). At the most general level, the discovery of non-interacting responses to rewards and punishments in our experiments hints at restrictions in the ability of stimuli of opposite valence to compensate for one another. The concept that gains offset losses, regardless of their qualitative nature, is widely embraced across society. Our results indicate biological limits to the validity of this idea.

References

- Aupperle RL, Melrose AJ, Francisco A, Paulus MP, Stein MB (2015) Neural substrates of approach-avoidance conflict decision-making. *Hum Brain Mapp* 36:449-462.
- Basten U, Biele G, Heekeren HR, Fiebach CJ (2010) How the brain integrates costs and benefits during decision making. *Proc Natl Acad Sci U S A* 107:21767-21772.
- Berridge KC (2018) Evolving Concepts of Emotion and Motivation. *Front Psychol* 9:1647.
- Berridge KC, Valenstein ES (1991) What psychological process mediates feeding evoked by electrical stimulation of the lateral hypothalamus? *Behav Neurosci* 105:3-14.
- Bissonette GB, Gentry RN, Padmala S, Pessoa L, Roesch MR (2014) Impact of appetitive and aversive outcomes on brain responses: linking the animal and human literatures. *Front Syst Neurosci* 8:24.
- Brandao ML, de Aguiar JC, Graeff FG (1982) GABA mediation of the anti-aversive action of minor tranquilizers. *Pharmacol Biochem Behav* 16:397-402.
- Bublitzky F, Alpers GW, Pittig A (2017) From avoidance to approach: The influence of threat-of-shock on reward-based decision making. *Behav Res Ther* 96:47-56.
- Carelli RM, West EA (2014) When a good taste turns bad: Neural mechanisms underlying the emergence of negative affect and associated natural reward devaluation by cocaine. *Neuropharmacology* 76 Pt B:360-369.
- Carlezon WA, Jr., Thomas MJ (2009) Biological substrates of reward and aversion: a nucleus accumbens activity hypothesis. *Neuropharmacology* 56 Suppl 1:122-132.

- Cox RW (1996) AFNI: software for analysis and visualization of functional magnetic resonance neuroimages. *Comput Biomed Res* 29:162-173.
- de Jong JW, Afjei SA, Pollak Dorocic I, Peck JR, Liu C, Kim CK, Tian L, Deisseroth K, Lammel S (2019) A Neural Circuit Mechanism for Encoding Aversive Stimuli in the Mesolimbic Dopamine System. *Neuron* 101:133-151 e137.
- Delgado MR, Nystrom LE, Fissell C, Noll DC, Fiez JA (2000) Tracking the hemodynamic responses to reward and punishment in the striatum. *J Neurophysiol* 84:3072-3077.
- Denys D, Mantione M, Figee M, van den Munckhof P, Koerselman F, Westenberg H, Bosch A, Schuurman R (2010) Deep brain stimulation of the nucleus accumbens for treatment-refractory obsessive-compulsive disorder. *Arch Gen Psychiatry* 67:1061-1068.
- Di Scala G, Mana MJ, Jacobs WJ, Phillips AG (1987) Evidence of Pavlovian conditioned fear following electrical stimulation of the periaqueductal grey in the rat. *Physiol Behav* 40:55-63.
- Fiallos AM, Bricault SJ, Cai LX, Worku HA, Colonnese MT, Westmeyer GG, Jasanoff A (2017) Reward magnitude tracking by neural populations in ventral striatum. *Neuroimage* 146:1003-1015.
- Gallistel CR, Leon M (1991) Measuring the subjective magnitude of brain stimulation reward by titration with rate of reward. *Behav Neurosci* 105:913-925.
- Gehrlach DA, Dolensek N, Klein AS, Roy Chowdhury R, Matthys A, Junghanel M, Gaitanos TN, Podgornik A, Black TD, Reddy Vaka N, Conzelmann KK, Gogolla N (2019) Aversive state processing in the posterior insular cortex. *Nat Neurosci* 22:1424-1437.
- Green L, Rachlin H (1991) Economic substitutability of electrical brain stimulation, food, and water. *J Exp Anal Behav* 55:133-143.
- Hayes DJ, Northoff G, Greenshaw AJ (2015) Editorial: Reward- and aversion-related processing in the brain: translational evidence for separate and shared circuits. *Front Syst Neurosci* 9:147.
- Hu H (2016) Reward and Aversion. *Annu Rev Neurosci* 39:297-324.
- Ibrahim C, Rubin-Kahana DS, Pushparaj A, Musiol M, Blumberger DM, Daskalakis ZJ, Zangen A, Le Foll B (2019) The Insula: A Brain Stimulation Target for the Treatment of Addiction. *Front Pharmacol* 10:720.
- Kahneman D, Tversky A (1979) Prospect theory: An analysis of decision under risk. *Econometrica* 47:263-291.
- Lammel S, Lim BK, Malenka RC (2014) Reward and aversion in a heterogeneous midbrain dopamine system. *Neuropharmacology* 76 Pt B:351-359.

- Lammel S, Lim BK, Ran C, Huang KW, Betley MJ, Tye KM, Deisseroth K, Malenka RC (2012) Input-specific control of reward and aversion in the ventral tegmental area. *Nature* 491:212-217.
- Levy DJ, Glimcher PW (2012) The root of all value: a neural common currency for choice. *Curr Opin Neurobiol* 22:1027-1038.
- Luigjes J, van den Brink W, Feenstra M, van den Munckhof P, Schuurman PR, Schippers R, Mazaheri A, De Vries TJ, Denys D (2012) Deep brain stimulation in addiction: a review of potential brain targets. *Mol Psychiatry* 17:572-583.
- Maren S (2016) Parsing Reward and Aversion in the Amygdala. *Neuron* 90:209-211.
- Mirenowicz J, Schultz W (1996) Preferential activation of midbrain dopamine neurons by appetitive rather than aversive stimuli. *Nature* 379:449-451.
- Nauczyciel C, Robic S, Dondaine T, Verin M, Robert G, Drapier D, Naudet F, Millet B (2013) The nucleus accumbens: a target for deep brain stimulation in resistant major depressive disorder. *J Mol Psychiatry* 1:17.
- Nieh EH, Kim SY, Namburi P, Tye KM (2013) Optogenetic dissection of neural circuits underlying emotional valence and motivated behaviors. *Brain Res* 1511:73-92.
- O'Doherty J, Kringelbach ML, Rolls ET, Hornak J, Andrews C (2001) Abstract reward and punishment representations in the human orbitofrontal cortex. *Nat Neurosci* 4:95-102.
- Olds J, Milner P (1954) Positive reinforcement produced by electrical stimulation of septal area and other regions of rat brain. *J Comp Physiol Psychol* 47:419-427.
- Paxinos G, Watson C (1997) *The Rat Brain in Stereotaxic Coordinates, Compact 3rd Ed.* San Diego: Academic Press.
- Piantadosi PT, Yeates DCM, Wilkins M, Floresco SB (2017) Contributions of basolateral amygdala and nucleus accumbens subregions to mediating motivational conflict during punished reward-seeking. *Neurobiol Learn Mem* 140:92-105.
- Rudebeck PH, Walton ME, Smyth AN, Bannerman DM, Rushworth MF (2006) Separate neural pathways process different decision costs. *Nat Neurosci* 9:1161-1168.
- Sierra-Mercado D, Deckersbach T, Arulpragasam AR, Chou T, Rodman AM, Duffy A, McDonald EJ, Eckhardt CA, Corse AK, Kaur N, Eskandar EN, Dougherty DD (2015) Decision making in avoidance-reward conflict: a paradigm for non-human primates and humans. *Brain Struct Funct* 220:2509-2517.
- Sutton RS, Barto AG (1998) *Reinforcement Learning.* Cambridge, MA: MIT Press.
- Valenstein ES (1965) Independence of Approach and Escape Reactions to Electrical Stimulation of the Brain. *J Comp Physiol Psychol* 60:20-30.

- VanElzakker MB, Dahlgren MK, Davis FC, Dubois S, Shin LM (2014) From Pavlov to PTSD: the extinction of conditioned fear in rodents, humans, and anxiety disorders. *Neurobiol Learn Mem* 113:3-18.
- Vianna DM, Landeira-Fernandez J, Brandao ML (2001) Dorsolateral and ventral regions of the periaqueductal gray matter are involved in distinct types of fear. *Neurosci Biobehav Rev* 25:711-719.
- Volkow ND, Michaelides M, Baler R (2019) The Neuroscience of Drug Reward and Addiction. *Physiol Rev* 99:2115-2140.
- von Neumann J, Morgenstern O (1944) *Theory of Games and Economic Behavior*. Princeton, NJ: Princeton University Press.
- Weele CMV, Siciliano CA, Tye KM (2019) Dopamine tunes prefrontal outputs to orchestrate aversive processing. *Brain Res* 1713:16-31.
- Wise RA (2005) Forebrain substrates of reward and motivation. *J Comp Neurol* 493:115-121.

Figures

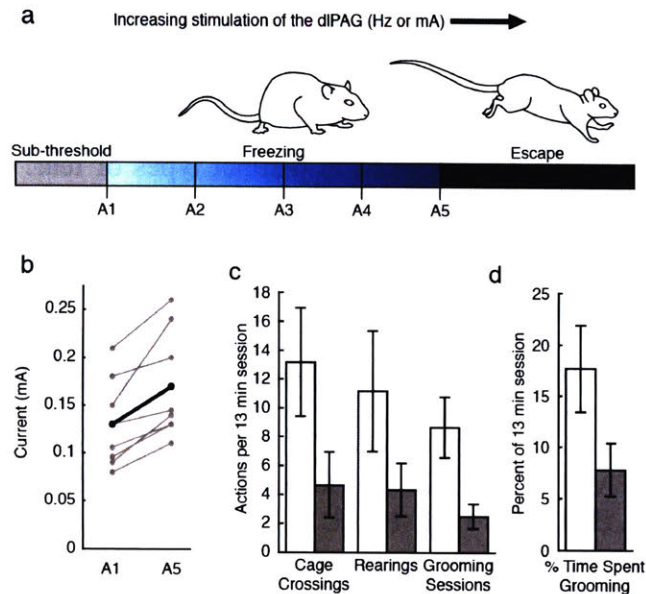


Figure 1. Stimulation of the dIPAG induces aversive behaviors. (a) A diagram of the different behavioral epochs observed when stimulating the dIPAG. A1 represents the freezing threshold and A5 represents the escape threshold. $A2 = 0.25 \cdot (A5 - A1)$, $A3 = 0.5 \cdot (A5 - A1)$, and $A4 = 0.75 \cdot (A5 - A1)$ when these thresholds are established using the increasing frequency method. (b) A summary of the mean behavioral thresholds established using the increasing current method for freezing (A1) and escape (A5) for the animals used in figures 1 and 2. (c) Behavioral effects of constant stimulation of the dIPAG at 90% of the freezing threshold current. White bars represent the prevalence of the behavior under control conditions. Gray bars represent the prevalence of the behavior while the animals were receiving continuous dIPAG stimulation. Cage crossings refers to horizontal movement from one edge of the cage to the other, and showed a significant decrease (students paired t-test; $p = 0.0023$; $n = 6$). A rearing referred to any time both front feet were off the floor of the cage, and showed a decrease that did not reach significance (students paired t-test; $p = 0.106$; $n = 6$). The number of initiated grooming sessions also showed a significant decrease (students paired t-test; $p < 0.01$; $n = 6$). (d) The percentage of time the animals spent grooming during a control session (white bar) was significantly higher than during constant stimulation of the dIPAG (gray bar), (Students paired t-test; $p = 0.0208$; $n = 6$).

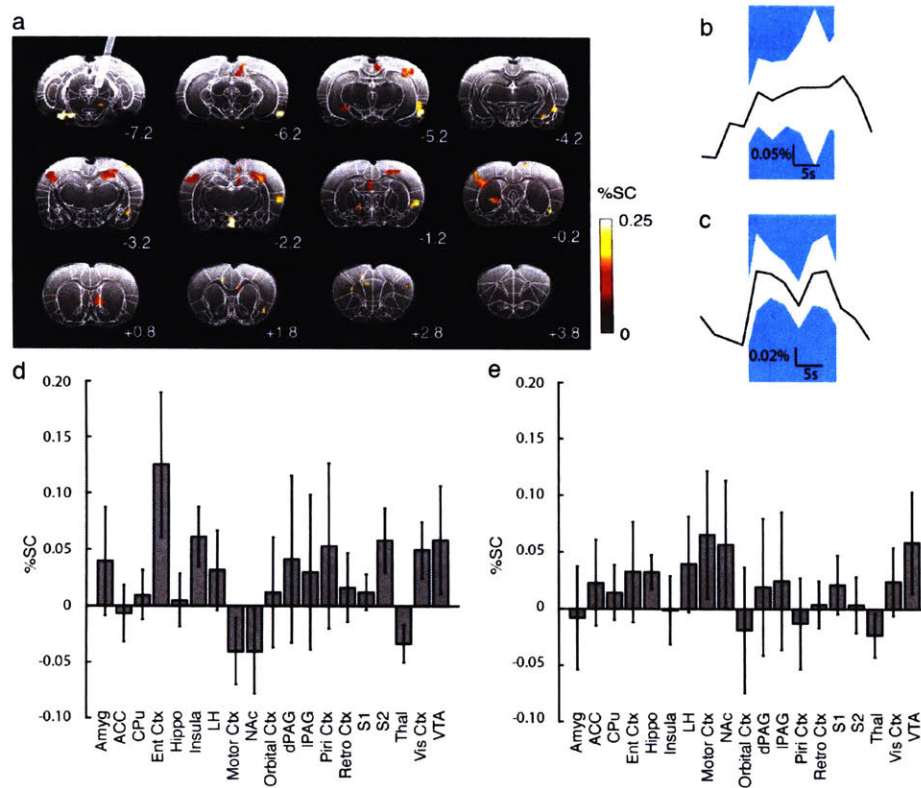


Figure 2. Stimulation of the dIPAG activates the brain only sparsely. (a) fMRI data was collected from eleven rats during electrical stimulation of the dIPAG at 60 Hz and 90% of the freezing threshold current. Each animal underwent 28 consecutive stimulation blocks, where a block consisted of 16 s of stim on and 10 s of stim off. Gray underlay shows an anatomical image of the rat brain. Color overlay shows the percent signal change for all voxels that passed the $p < 0.05$ threshold for activation during the stimulation block. Statistics from a jackknife analysis of the concatenated dataset. Transparent white bar indicates the electrode position. (b) Average percent signal change in the entorhinal cortex ipsilateral to the electrode over time. Blue bar indicates the time during which the stimulus was on. Gray shading represents the SEM computed for each timepoint as part of the jackknife analysis. (c) Average percent signal change in the insular cortex ipsilateral to the electrode over time. Blue bar indicates the time during which the stimulus was on. Gray shading represents the SEM computed for each timepoint as part of the jackknife analysis. (d) The average activation of regions ipsilateral to the electrode in response to the stimulus was calculated. Error bars represent the SEM computed for each region as part of the jackknife analysis. (e) The average activation of regions contralateral to the electrode in response to the stimulus was calculated. Error bars represent the SEM computed for each region as part of the jackknife analysis. Abbreviations: amyg, amygdala; cing, cingulate; ctx, cortex; CPu, caudate putamen; ent, entorhinal; hippo, hippocampus; LH, lateral hypothalamus; NAc, nucleus accumbens; dPAG, dorsal periaqueductal gray (includes the dorsomedial and dorsolateral subregions); IPAG, lateral

periaqueductal gray; retro, retrosplenial; S1, primary somatosensory cortex; S2, secondary somatosensory cortex; thal, thalamus; vis, visual; VTA, ventral tegmental area

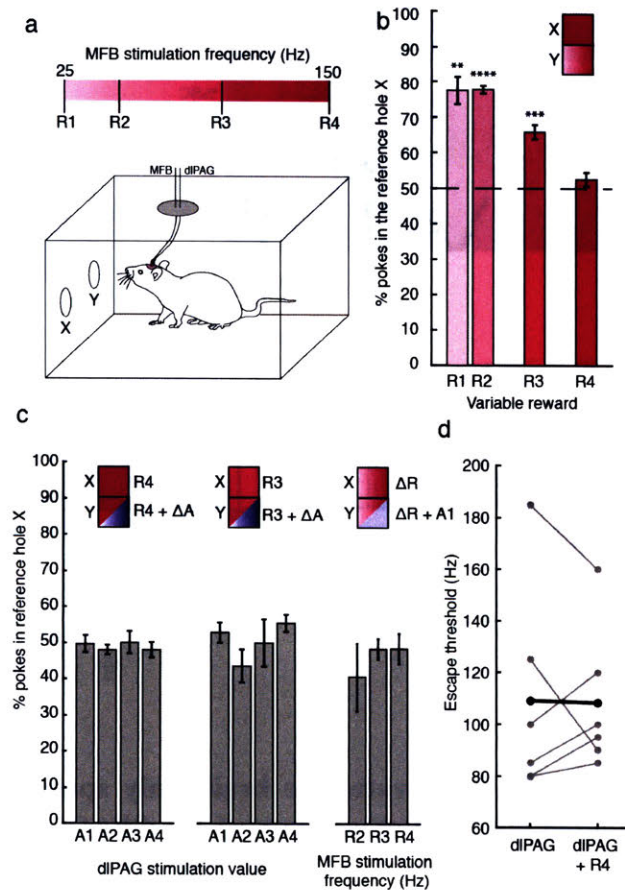


Figure 3. Stimulation of the dIPAG does not affect reward-seeking behavior. (a) A diagram of the two-choice experimental setup. The animal has electrodes placed in both MFB and dIPAG. For most tests, poking in the reference hole (X) would deliver MFB stimulation alone, while poking in the other hole (Y) would result in stimulation of both the MFB and dIPAG electrodes. (b) Frequency test used to verify each animal was capable of discriminating between rewards (MFB stimuli) of different frequencies. Summary results for all animals are presented in this graph. The reference frequency was 150 Hz (R4). Animals significantly preferred receiving the reference frequency reward over the variable frequency when the variable frequency was 25 Hz (R1), 50 Hz (R2), or 100 Hz (R3), but there was no difference when both holes produced a reward of 150 Hz (R4). (n = 6). (c, left) Poking in one hole resulted in R4 MFB stimulation alone. Poking in the other hole resulted in R4 MFB stimulation accompanied by dIPAG stimulation that varied between the freezing (A1) and escape (A5) thresholds for the given animal (n = 6). (c, center) The experiment shown in (c) was repeated, but with a lower MFB stimulation value of 100 Hz (n = 3). (c, right) Poking in one hole resulted in MFB stimulation at 50, 100, or 150 Hz, while poking in the other hole resulted in MFB stimulation at 50, 100, or 150 Hz in addition to dIPAG stimulation

at the freezing threshold (A1). (d) The escape threshold was established both without and with simultaneous MFB stimulation at R4 (150 Hz). Gray lines are individual animals, while the thick black line shows the average. (* $p < 0.05$; ** $p < 0.01$; *** $p < 0.001$; **** $p < 0.0001$)

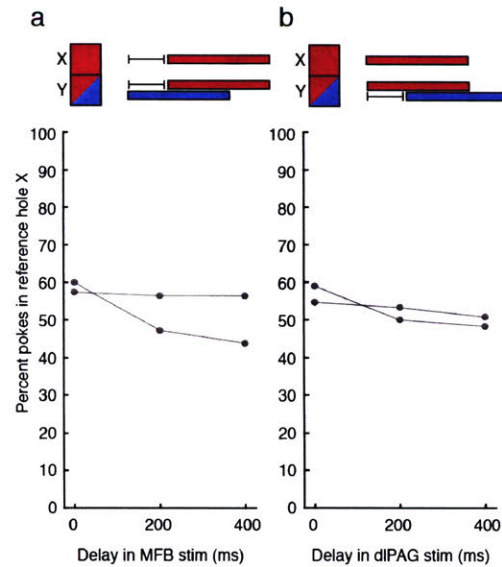


Figure 4. There is no clear effect of stimulus delay on the combined rewarding and aversive behavioral paradigm. The experiment described in Fig. 3c was repeated for two animals with the rewarding stimulus set to R4 and the aversive stimulus set to A3. However, one of the two stimuli was delayed by the specified amount relative to the nosepoke event. (a) Top panels shows a diagram of the MFB delay experiment, where the pink bars denote the rewarding (MFB) stimuli and the blue bar denotes the aversive (dIPAG) stimulus. Bottom panel shows a graph of the results as a function of the MFB delay. (b) Top panels shows a diagram of the dIPAG delay experiment, where the pink bars denote the rewarding (MFB) stimuli and the blue bar denotes the aversive (dIPAG) stimulus. Bottom panel shows a graph of the results as a function of the dIPAG delay.

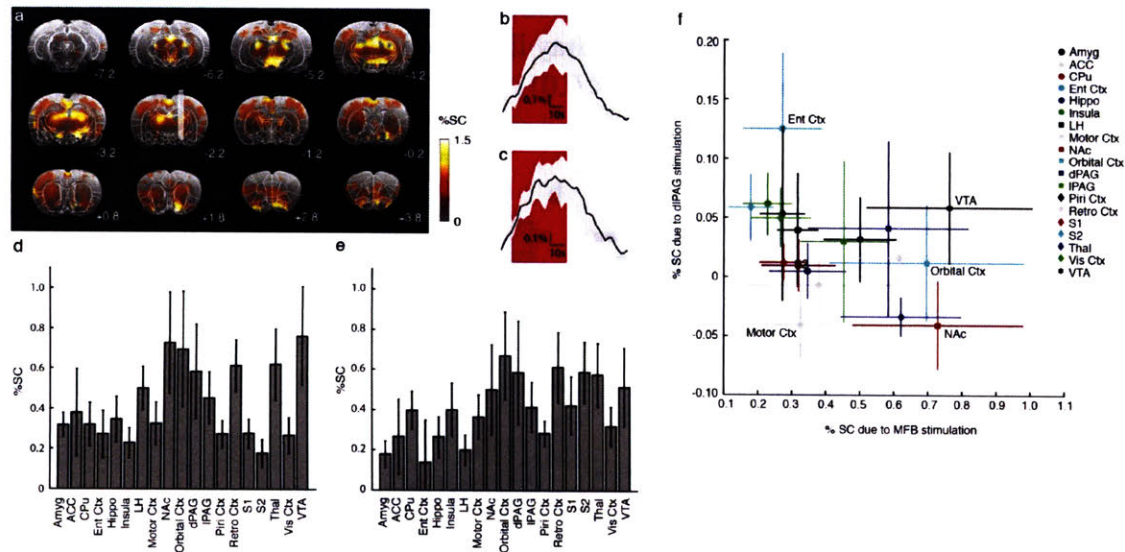


Figure 5. Stimulation of the MFB activates reward-related structures. (a) Functional imaging data was collected from rats during electrical stimulation of the MFB (Fiallos et al., 2017). Each animal underwent 30 consecutive stimulation blocks, where a block consisted of eight repetitions of a 1s stimulus train at a given frequency followed by 4s of rest. Frequencies ranged from 44 to 232 Hz. In the source paper frequencies were analyzed separately, but for this analysis all stimuli were binned together. Gray underlay shows an anatomical image of the rat brain. Color overlay shows the percent signal change for all voxels that passed the $p < 0.05$ threshold for activation during the stimulation block. Statistics from a jackknife analysis of the concatenated dataset. Transparent white bar indicates the electrode position. (b) Average percent signal change in the nucleus accumbens ipsilateral to the electrode over time. Red bar indicates the time during which the stimulus was on. Gray shading represents the SEM computed for each timepoint as part of the jackknife analysis. (c) Average percent signal change in the VTA ipsilateral to the electrode over time. Red bar indicates the time during which the stimulus was on. Gray shading represents the SEM computed for each timepoint as part of the jackknife analysis. (d) The average activation of regions ipsilateral to the electrode in response to the stimulus was calculated. Error bars represent the SEM computed for each region as part of the jackknife analysis. (e) The average activation of regions contralateral to the electrode in response to the stimulus was calculated. Error bars represent the SEM computed for each region as part of the jackknife analysis. Abbreviations: amyg, amygdala; cing, cingulate; ctx, cortex; CPU, caudate putamen; hippo, hippocampus; LH, lateral hypothalamus; NAc, nucleus accumbens; dPAG, dorsal periaqueductal gray (includes the dorsomedial and dorsolateral subregions); IPAG, lateral periaqueductal gray; retro, retrosplenial; S1, primary somatosensory cortex; S2, secondary somatosensory cortex; thal, thalamus; vis, visual; VTA, ventral tegmental area

Chapter 4

Brain-wide functional imaging in awake rodents

The contents of this chapter were written by Sarah Bricault with feedback from Alan Jasanoff. Experiments were performed by Sarah Bricault, Mitul Desai, and Jiyoung Lee. I performed all analyses.

Brain-wide functional imaging in awake rodents

Sarah Bricault¹, Mitul Desai², Jiyoung Lee³, and Alan Jasanoff^{2,4,5}

¹ Department of Biology, Massachusetts Institute of Technology

² Department of Biological Engineering, Massachusetts Institute of Technology

³ Department of Neurobiology, Wellesley College

⁴ Department of Brain and Cognitive Sciences, Massachusetts Institute of Technology

⁵ Department of Nuclear Science and Engineering, Massachusetts Institute of Technology

Abstract

It is difficult to get rodents to voluntarily remain motionless during a functional MRI (fMRI) experiment. The most common method for preventing motion is to use anesthesia, for example isoflurane, in combination with a paralytic agent and image the animals in that state. The other method is to physically restrain the animal. However, even with optimal restraints and multiple days of acclimation, animal motion levels (from struggling or simple twitching of facial muscles) are high when using this technique. Here, we present a prep designed to overcome the tradeoff between image quality and applicability to the awake brain. We describe here a novel technique for fMRI data acquisition that retains the applicability to the awake brain and produces high-quality imaging data through the use of paralysis without accompanying anesthesia. We demonstrate that animals can be acclimated to this condition, such that their stress hormone levels decline precipitously after several days. We also validate the utility of the preparation by showing that resting-state functional connectivity data obtained from these animals is similar to that observed in awake animals and dissimilar to that observed in anesthetized animals. Overall, this approach provides a potentially powerful path to imaging behaviorally-relevant neural dynamics on a brain-wide scale. There may be particular utility of the unanesthetized paralyzed

preparation for analysis of resting-state activity dynamics, which are often subtle and particularly sensitive to motion artifacts.

Introduction

One key goal of MRI neurobiological research is to image awake, behaving animals during the acquisition of functional data. Humans are typically imaged in an awake state and often perform behavioral tasks during fMRI for research or diagnostic purposes (e.g. Kirk et al., 2016). Macaques (Goense et al., 2010) and marmosets (Hung et al., 2015) can also be trained to remain still enough for combined fMRI and behavioral testing to take place. However, even in macaques the reduced brain size and increased motion artifacts (from voluntary movement, blinking, etc.) make scan quality quite low (Goense et al., 2010). There are only a couple of studies that have performed fMRI on behaving rodents. Tabuchi et al. performed fMRI on rats during drinking behavior (2002), and Han et al., used licking behavior as an output in a Go/No-Go task (2019). The sparsity of such behaving rodent studies is a testament to both the difficulty of acclimating and training the animal and the relatively poor quality of the fMRI data obtained.

It is well known (and demonstrated here) that motion artifacts caused by physically restrained rodents are large and disrupt the quality of the functional imaging data. Acclimating animals to the physical restraint does reduce the motion somewhat, but it is mostly useful in preventing large struggling movements and has little effect on minute motions such as whisker twitching. Some studies have demonstrated awake imaging in minimally restrained animals but even aside from the minute muscle motion issue, the acclimation can take as long as ten days (Chang et al., 2016).

The alternative to physical restraint is to apply a combination of anesthesia and paralysis. However, anesthesia induces poorly-understood changes in the brain. The brain states associated with anesthesia regimens are different from those observed in either awake or asleep subjects (Akeju and Brown, 2017; Murphey et al., 2011), though anesthetics may access some of the same neural systems as sleep (Tung et al., 2004). Thus, any experiments performed under the influence of anesthesia must be considered in the context of that confound.

Unlike anesthesia, the paralytic pancuronium bromide does not appreciably alter the state of the brain (Perry, 1985; Kimball et al., 1985). Humans who have received paralysis using this agent without accompanying anesthesia report that they were conscious and experiencing sensations including pain during the procedure (Perry, 1985). Humans have historically (and sometimes repeatedly) undergone paralysis without anesthesia for a variety of scientific purposes (Kimball et al., 1985).

In rodents, pancuronium bromide (or another paralytic) is typically used in conjunction with an anesthetic. We describe here a novel preparation for fMRI data acquisition that retains the applicability to the awake brain and produces high-quality imaging data through the use of paralysis without accompanying anesthesia. We find that our preparation is no more stressful than physical restraint, and verify that it produces high-quality imaging data.

Methods

Animals

All animal procedures were performed in strict compliance with US Federal guidelines, with oversight by the MIT Committee on Animal Care. Male Sprague-Dawley rats (250-400g), purchased from Charles River Laboratories (Wilmington, MA) were used for the data presented

in this paper. The animals were housed and maintained on a 12 h light/dark cycle with ad libitum access to food and water.

Surgical procedures

In preparation for imaging, rats were implanted with custom-made PEEK headposts so that their heads could be fixed in place during imaging. Animals were anaesthetized with 2% isoflurane, shaved, and mounted in a rodent stereotaxic device (David Kopf Instruments, Tujunga, CA). Heart rates and blood oxygenation levels were monitored by a pulse oximeter (Nonin Medical, Plymouth, MN). The scalp was retracted and the headpost was placed approximately over bregma. In animals undergoing physical restraint acclimation, four copper beryllium screws were inserted such that they penetrated the skull but not the dura to provide additional support to the headpost. The headpost (and screws, if applicable) was secured using C&B Metabond dental cement (Parkell, Edgewood, NY). Each rat was given a subcutaneous injection of buprenorphine (MIT pharmacy) at a dose of 0.01 mg/kg for analgesia at the end of surgery, and once a day for two days following surgery. Rats were allowed to recover from surgery for at least three days before acclimation began.

Unanesthetized, paralyzed acclimation

All animals that were imaged in a state of unanesthetized paralysis underwent the following acclimation. The acclimation period lasted approximately one week, consisting of two consecutive days, one break day, and two final consecutive days. On the final day of acclimation, EPI scan noises were played to the animal to simulate the auditory environment of the scanner. For a subset of animals, corticosterone measurements were being taken at the beginning and end

of the procedure each day. For these animals, the acclimation was performed at the same time of day +/- 30 min throughout the acclimation week.

Each individual day of acclimation began with the animal being weighed, then anesthetized with 3% isoflurane. Either a tail vein catheter was established or, for animals with a chronically implanted jugular vein catheter, the catheter was briefly flushed with heparinized saline. If corticosterone measurements were being taken, the animal was quickly placed in a tube restraint that allowed for access to the chronically implanted jugular vein catheter. These animals were allowed to recover from the isoflurane anesthesia and as soon as they displayed active motor behavior or a substantial motor response to a tail pinch, a control (pre-experiment) blood sample was drawn. The animals were then re-anesthetized with 3% isoflurane and removed from the tube restraint.

Animals were then intubated and ventilated, and placed on a heating pad to maintain their body temperature. Heart rate, expired CO₂, breathing rate, and SpO₂ (peripheral capillary oxygen saturation) were monitored and recorded starting at this point, and isoflurane was reduced to 1%. Midazolam (1.25 mg/kg) and a bolus dose of pancuronium at 1.25 mg/kg were administered via the catheter. Pancuronium was delivered continuously at 1.5 mg/kg/h for the remainder of the acclimation. Five minutes after the bolus dose of pancuronium, the isoflurane flow was stopped and animals were allowed to recover for 15 min. During this period, animals were monitored closely, and in the case of incomplete paralysis (due to catheter failure), the acclimation was immediately terminated, the pancuronium reversal agent neostigmine was administered, and the animal was allowed to recover.

After the 15 min recovery from isoflurane, the experimentally defined 30 min acclimation period began. Animals were covered with an opaque box to simulate the darkness of

the scanner environment and, if it was the final day of acclimation, recorded scanner noises were played. At the end of this 30 min period, blood was drawn in animals for which corticosterone was being measured. The pancuronium reversal agent neostigmine (0.25 mg/kg) was administered at this time, sometimes in conjunction with atropine (0.135 mg/kg), which we found aided the recovery of the respiratory system. Isoflurane was reintroduced at 1% to prevent the animals from extubating themselves prior to regaining the ability to regulate their breathing.

Animals recovered from the paralysis at different rates, and the full recovery could take as little as 20 min or as long as 90 min. For animals whose recovery took longer than approximately 45 min, a second dose of neostigmine (0.25 mg/kg) and sometimes atropine (0.135 mg/kg) were administered. Once animals demonstrated the ability to regulate respiration, they were taken off the ventilator and the isoflurane was turned off. Oxygen was delivered until the animals began to move, at which point they were gently extubated and returned to their home cage. Animals were monitored for at least an hour after the procedure to ensure successful recovery.

fMRI of unanesthetized, paralyzed animals

Immediately prior to imaging experiments, rats were anesthetized using 3% isoflurane and maintained at 2% isoflurane during preparation. Animals were intubated and ventilated, and a tail vein catheter was established for drug delivery (or the chronically implanted jugular vein catheter was flushed with heparinized saline). Animals were then placed onto an imaging cradle and secured in place via screws that attached to the implanted headpost. Isoflurane was reduced to 0.75% and 1 mg/kg pancuronium (Sigma-Aldrich) was administered, followed by continuous delivery of 1.5 mg/kg/h pancuronium thereafter. Respiration, heart rate, and blood oxygen

saturation were monitored, and temperature was maintained with a circulating warm water pad (Gaymar, Orchard Park, NY) for the remainder of the procedure. At the end of the imaging procedure, isoflurane was reintroduced at 3%. A minimum of ten minutes later, the animals were euthanized.

fMRI data acquisition

For the unanesthetized, paralyzed control imaging, the following parameters were used. Imaging was performed using a 7 T Biospec MRI scanner (Bruker) scanner operating with a cross coil volume transmit, surface receive configuration. A rapid acquisition with refocused echoes (RARE) pulse sequence were used to acquire T2-weighted anatomical images, with number of averages (NA) = 16, matrix size = 256×256 , FOV = 2.2 cm \times 2.2 cm, slice thickness = 1 mm, effective TR = 2500 ms, effective TE = 44 ms, and RARE factor = 8. For functional imaging, echo planar imaging (EPI) image series were acquired. EPI scan parameters were NA = 1, matrix size = 53×53 , FOV = 2.2 cm \times 2.2 cm, slice thickness = 1 mm, TR = 2500 ms, and effective TE = 5.8805 ms.

For the awake restrained imaging, the following parameters were used. Imaging was performed using a 9.4 T Biospec MRI scanner (Bruker) scanner operating with a volume coil transmit and receive configuration. A rapid acquisition with refocused echoes (RARE) pulse sequence were used to acquire T2-weighted anatomical images, with number of averages (NA) = 4, matrix size = 256×256 , FOV = 2.5 cm \times 2.5 cm, slice thickness = 1 mm, effective TR = 2540.718 ms, effective TE = 56 ms, and RARE factor = 8. For functional imaging, echo planar imaging (EPI) image series were acquired. EPI scan parameters were NA = 1, matrix size = 100

× 100, FOV = 2.5 cm × 2.5 cm, slice thickness = 1 mm, TR = 2000 ms, and effective TE = 30.096 ms.

fMRI data analysis

Images were reconstructed with Paravision software (Bruker) and analyzed using AFNI (Gold et al., 1998; Cox, 1996) and custom MATLAB (Mathworks) routines. Preprocessing steps for the EPI data included removal of signal outside the brain, alignment to the anatomical scans using AFNI's 3dAllineate, motion correction using AFNI's 3dvolreg, spatial smoothing to 1 mm full width at half maximum using AFNI's 3dBlurToFWHM, voxel-wise signal detrending and intensity normalization, and temporal smoothing using a sliding window of width equal to three scans. For group analysis, the motion and global signal were regressed out of the concatenated dataset.

To generate the graphs of motion shown in Fig 1*a*, we calculated the maximum motion in each of the six orientations for each animal and each condition.

To generate the seed-based maps shown in Fig 1*d*, *e*, and *f*, the timecourse for the seed ROI was extracted using the Paxinos atlas and averaged over all voxels within the given ROI. Then, regression analysis was performed on a voxel-by-voxel basis to determine the beta-coefficient for each voxel relative to the seed. To get a p-value for each voxel, we used jackknife analysis.

Corticosterone measurements

To measure corticosterone levels, we collected blood at two timepoints as described in the acclimation section. Immediately after the ~0.5 mL of blood was drawn, it was placed into

treated tubes to prevent clotting and refrigerated. Once all blood samples had been collected, we used an ELISA kit to measure the concentration of corticosterone for each animal at each timepoint.

Results and discussion

In primate fMRI, it is possible to gather data while subjects are performing a variety of tasks. This provides more direct information about the neural circuitry underlying the behaviors than in rodent studies. It is extremely difficult to tell a rat to “stay still” while also performing a behavioral task. There is some precedence for acclimating rats to remain still during experimental procedures, including fMRI (Chang et al., 2016). However, few studies have managed to perform fMRI during behavior (Tabuchi et al., 2002) given the length of time the animal would need to remain still, the inability of scientists to monitor animals for signs of distress or motion, and the sensitivity of fMRI to motion artifacts. Thus, the best solution until now has been to determine behaviorally relevant stimuli for awake animals and to apply those same stimuli to anesthetized, paralyzed animals or to physically restrained animals during fMRI to study behavior.

We have validated the utility of our unanesthetized, paralyzed technique as demonstrated in Fig 1*a* and *b*. In these panels, you see the maximum extent of rotational and translational motion, respectively, in rats acclimated to physical restraint compared to rats acclimated to unanesthetized or anesthetized paralysis. The latter two conditions are not significantly different from one another, but in every case physically restrained animals displayed significantly larger motion artifacts than unanesthetized, paralyzed animals (*t*-tests for roll, $p < 0.001$; pitch, $p < 0.05$; yaw, $p < 0.01$; x-axis motion, $p < 0.05$; y-axis motion, $p < 0.001$; z-axis motion, $p < 0.01$).

Importantly, we have also verified that it is humane to utilize this technique. We measured animal corticosterone levels at the end of each day of acclimation to both physical restraint (red bars) and unanesthetized paralysis (blue bars) as shown in Fig 1c. If we compare the third day of acclimation to both preparations, there is no significant elevation in corticosterone levels for unanaesthetized paralyzed animals over awake, restrained animals (t -test, $p > 0.05$).

Resting-state functional connectivity has been studied extensively in rodents, both awake and anesthetized. One of the hallmarks of high-quality resting-state data from awake rodents is the ability to observe bilateral connectivity in the primary somatosensory cortex (S1) (Liu et al., 2013). Indeed, in the data we collected from awake, physically restrained rats we were able to observe this connectivity (Fig. 1f). Here, the seed was placed in the right S1 and regions of correlation are observed both around the seed and in S1 on the left (contralateral) side of the brain. However, this bilateral connectivity of S1 is absent in animals anesthetized with isoflurane anesthesia (Fig. 1e). In our unanesthetized paralysis condition, however, we again see bilateral connectivity within S1 (Fig. 1d). (Note that the global signal has been regressed out of all functional datasets.) This further demonstrates that our preparation preserves the applicability to the awake brain.

Our ultimate goal with this technique is to use it to gain further insight into the neural circuits that underlie behavioral processes. Although paralyzed animals are incapable of behaving in a standard, physical sense, they are conscious and therefore capable of responding internally. It is well-known, for example, that humans and other animals can learn to modulate the activity of specific brain regions and even individual neurons (Sitaram et al., 2017). It should be possible to employ this sort of neurofeedback in conjunction with direct rewarding brain

stimulation to teach rodents to make decisions during fMRI scans. Such a system would open up a new model for studying decision-making in rodents.

References

- Akeju, Oluwaseun, and Emery N. Brown. "Neural oscillations demonstrate that general anesthesia and sedative states are neurophysiologically distinct from sleep." *Current opinion in neurobiology* 44 (2017): 178-185.
- Chang, Pei-Ching, et al. "Novel method for functional brain imaging in awake minimally restrained rats." *Journal of neurophysiology* 116.1 (2016): 61-80.
- Cox, Robert W. "AFNI: software for analysis and visualization of functional magnetic resonance neuroimages." *Computers and Biomedical research* 29.3 (1996): 162-173.
- Goense, Jozien BM, Kevin Whittingstall, and Nikos K. Logothetis. "Functional magnetic resonance imaging of awake behaving macaques." *Methods* 50.3 (2010): 178-188.
- Gold, Sherri, et al. "Functional MRI statistical software packages: a comparative analysis." *Human brain mapping* 6.2 (1998): 73-84.
- Han, Zhe, et al. "Awake and behaving mouse fMRI during Go/No-Go task." *Neuroimage* 188 (2019): 733-742.
- Hung, Chia-Chun, et al. "Functional MRI of visual responses in the awake, behaving marmoset." *Neuroimage* 120 (2015): 1-11.
- Kimball, William R., et al. "Effects of paralysis with pancuronium on chest wall statics in awake humans." *Journal of Applied Physiology* 58.5 (1985): 1638-1645.
- Kirk, Ulrich, et al. "Mindfulness training increases cooperative decision making in economic exchanges: Evidence from fMRI." *NeuroImage* 138 (2016): 274-283.
- Liu, Xiao, et al. "The change of functional connectivity specificity in rats under various anesthesia levels and its neural origin." *Brain topography* 26.3 (2013): 363-377.
- Murphy, Michael, et al. "Propofol anesthesia and sleep: a high-density EEG study." *Sleep* 34.3 (2011): 283-291.
- Paasonen, Jaakko, et al. "Functional connectivity under six anesthesia protocols and the awake condition in rat brain." *Neuroimage* 172 (2018): 9-20.

- Perry, Samuel W. "Psychological reactions to pancuronium bromide." *American Journal of Psychiatry* 142.11 (1985): 1390-a.
- Sitaram, Ranganatha, et al. "Closed-loop brain training: the science of neurofeedback." *Nature Reviews Neuroscience* 18.2 (2017): 86.
- Tabuchi, Eiichi, et al. "Spatio-temporal dynamics of brain activated regions during drinking behavior in rats." *Brain research* 951.2 (2002): 270-279.
- Tung, Avery, and Wallace B. Mendelson. "Anesthesia and sleep." *Sleep medicine reviews* 8.3 (2004): 213-225.

Figures

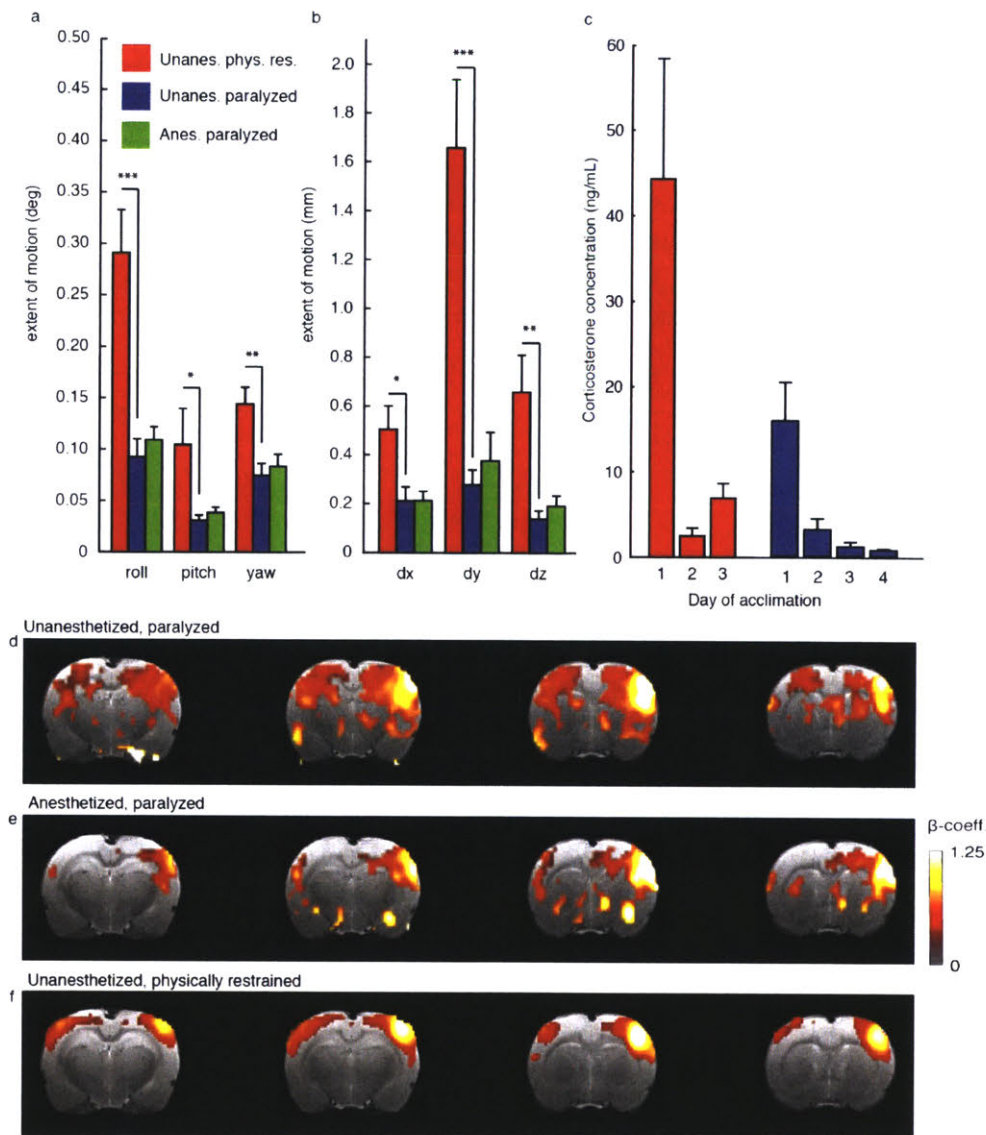


Figure 1: Unanesthetized, paralytic technique. a. Comparing the extent of motion in roll, pitch, and yaw between unanesthetized, physically restrained (red), unanesthetized, paralyzed (blue), and anesthetized, paralyzed (green). b. Comparing the extent of motion in dx, dy, and dz between unanesthetized, physically restrained (red), unanesthetized, paralyzed (blue), and anesthetized, paralyzed (green). c. Corticosterone measurements made over three days of acclimation to physical restraint (red) and four days of acclimation to unanesthetized paralysis (blue). d. Seed-based functional connectivity with the left S1BF in unanesthetized, paralyzed animals. e. Seed-based functional connectivity with the left S1BF in anesthetized, paralyzed animals. f. Seed-based functional connectivity with the left S1BF in unanesthetized, physically restrained animals. (S1BF, primary somatosensory barrel field cortex; * $p < 0.05$; ** $p < 0.01$; *** $p < 0.001$; **** $p < 0.0001$; all p -values calculated using the student's t-test)

Chapter 5

Image-guided neural activity manipulation with a paramagnetic drug

The contents of this chapter are from a paper recently published in Nature Communications with the same title. The text was written by Ali Barandov, Sarah Bricault, and Alan Jasanoff. I performed all in vivo experiments with assistance from Ali Barandov, Nan Li, and Elizabeth DeTienne and analyzed the resulting fMRI data. I also supervised all of Elizabeth DeTienne's work in the lab.

Bricault, Sarah, and Ali Barandov et al. "Image-guided neural activity manipulation with a paramagnetic drug." *Nature Communications* 11.1 (2020): 1-6.

Image-guided neural activity manipulation with a paramagnetic drug

Sarah Bricault^{1†}, Ali Barandov^{2†}, Peter Harvey², Elizabeth DeTienne³,
Aviad Hai², & Alan Jasanoff^{2,4,5*}

- ¹ Department of Biology,
- ² Department of Biological Engineering,
- ³ Department of Electrical Engineering & Computer Science,
- ⁴ Department of Brain & Cognitive Sciences, and
- ⁵ Department of Nuclear Science & Engineering
Massachusetts Institute of Technology
77 Massachusetts Ave.
Rm. 16-561
Cambridge, MA 02139

* Address correspondence to AJ
phone: 617-452-2538
e-mail: jasanoff@mit.edu

† SB and AB contributed equally.

Submission date: 11/22/19

Key abbreviations: 1,4,7,10-Tetraazacyclododecane-1,4,7,10-Tetraacetic Acid (DOTA), Echo Planar Imaging (EPI), Field Of View (FOV), Functional Magnetic Resonance Imaging (fMRI), γ -Aminobutyric Acid (GABA), 4-(2-Hydroxyethyl)-1-Piperazineethanesulfonic Acid (HEPES), Longitudinal Relaxation Time (T_1), Magnetic Resonance Imaging (MRI), Paramagnetic Muscimol

(ParaMus), Primary Somatosensory Cortex (S1FL), Secondary Somatosensory Cortex (S2), Longitudinal Relaxivity (r_1), Ventral Posterolateral Nucleus (VPL).

Abstract

Targeted manipulations of neural activity are essential approaches in neuroscience and neurology, but monitoring such procedures in the living brain remains a significant challenge. Here we introduce a paramagnetic analog of the drug muscimol that enables targeted neural inactivation to be performed with feedback from magnetic resonance imaging. We validate pharmacological properties of the compound *in vitro*, and show that its distribution *in vivo* reliably predicts perturbations to brain activity.

Introduction

Neuromodulation methods are widely used for perturbations of neural activity in both basic science and clinical practice, but monitoring the time course and spatial extent of modulatory tools in living subjects is challenging. Even with modern optogenetic and chemogenetic approaches^{1,2}, measurement of actuator expression profiles is usually only possible postmortem, and the efficacy of these tools depends on light or drug level profiles that are rarely characterized. Traditional neuropharmacological perturbations are easier to apply in many species, but are also hard to monitor *in vivo*. Although fluorescent drug conjugates can be mapped histologically after death³, the resulting profiles may not reflect the distribution or dose that produced experimental neural activity perturbations of interest. Radiolabeled drugs can be mapped using nuclear imaging methods in living subjects⁴, but the tomographic instrumentation applied in such approaches typically provides poor spatiotemporal resolution, and synthesis and handling of the radiopharmaceuticals themselves is complex.

Here we describe an approach to image-guided manipulation of brain activity based on paramagnetic drugs that can be visualized noninvasively by magnetic resonance imaging (MRI). We apply the principle to muscimol, an agonist of γ -aminobutyric acid (GABA) A receptors that is widely used for targeted inactivation of neural structures, and that has previously been

applied as a fluorescent conjugate for postmortem histological imaging⁵. By chemically conjugating muscimol to a gadolinium chelate, we sought to create a paramagnetic muscimol analog (ParaMus) whose distribution could be imaged in real time *in vivo*, while offering pharmacological properties comparable to muscimol itself.

Results

Synthesis and characterization of ParaMus

The synthesis of ParaMus is diagrammed in **Fig. 1a**. The metal-free precursor to ParaMus (**6**) is prepared through cross-coupling of muscimol with the gadolinium binding ligand 1,4,7,10-tetraazacyclododecane-1,4,7,10-tetraacetic acid (DOTA), using a bifunctional triethylene glycol linker. ParaMus (**7**) is then formed by reacting **6** with excess of GdCl₃ at pH 5. Integrity and purity of the final compound is indicated by mass spectrometry and liquid chromatography (**Supplementary Fig. 1**). The MRI potency of ParaMus is reflected by the slope of its effect on the reciprocal of the longitudinal relaxation time (T_1) versus concentration, known as longitudinal relaxivity (r_1). MRI measurements at 7 T and room temperature indicate that the r_1 of ParaMus is $5.0 \pm 0.2 \text{ mM}^{-1}\text{s}^{-1}$ (error margins reflect SEM with $n = 3$, unless otherwise noted); this value is somewhat larger than the r_1 value of $3.6 \pm 0.3 \text{ mM}^{-1}\text{s}^{-1}$ for gadoteridol⁶, a contrast agent that approximates the Gd-DOTA moiety of ParaMus, and indicates that conjugation to muscimol does not compromise contrast-inducing properties of the gadolinium complex (**Supplementary Fig. 2**). Like Gd-DOTA, ParaMus also displays a weak transverse relaxivity of $7.3 \pm 0.6 \text{ mM}^{-1}\text{s}^{-1}$ (**Supplementary Fig. 3**), which is unlikely to substantially alter image contrast except at high concentrations.

To assess the efficacy of ParaMus as an inhibitor of neuronal excitability, we examined its pharmacological activity in vitro. We subjected primary rat cortical neurons to intracellular current clamp (**Fig. 1b**), and measured current thresholds for action potential initiation under test and control conditions (**Fig. 1c,d**). We found that untreated neurons exhibit a current threshold of 0.9 ± 0.2 nA ($n = 4$), compared with 2.1 ± 0.6 nA following bath application of 10 μ M ParaMus ($n = 4$). ParaMus also causes a decrease of $77 \pm 17\%$ in input resistance. Neurons treated with 10 μ M muscimol also display an increase in current threshold, from 0.6 ± 0.1 to 1.4 ± 0.2 nA ($n = 2$), as well as a $71 \pm 6\%$ decrease in input resistance, similar to ParaMus. By contrast, gadoteridol elicits virtually no change in current threshold or input resistance when tested in the same assay. This indicates that the pharmacological effects of ParaMus arise from its muscimol component.

Image-guided neural inactivation using ParaMus in vivo

To demonstrate image-guided manipulation of a neural system in vivo, we examined the ability of ParaMus to perturb brain responses to a sensory stimulus in anesthetized rats. We used functional MRI (fMRI) contrast to monitor brain-wide responses to electrical stimulation of the forepaw⁷ before, during, and after delivery of ParaMus to the ventral posterolateral nucleus of the thalamus (VPL), a relay point in the transmission of somatosensory input from the body to the cortex. The distribution of ParaMus infused via a cannula targeted to VPL could be visualized by T₁-weighted MRI (**Fig. 2a**). Before this treatment, forepaw stimulation produced strong fMRI responses in the forelimb field of primary somatosensory cortex (S1FL), and weak responses in secondary somatosensory cortex (S2). After infusion of 1.5 μ L ParaMus (1 mM) into the VPL region, responses were sharply reduced, as discernable from both activity maps

(**Fig. 2b**) and response time courses (**Fig. 2c**). Group results (**Fig. 2d,e**) show that consistent decreases in the S1FL response to forepaw stimulation can be observed following VPL-targeted ParaMus treatment (n = 5), but not following control treatment with gadoteridol (n = 4). Mean response amplitudes are $69 \pm 22\%$ lower after ParaMus (significant with paired t-test $p = 0.04$, n = 5), but an average of only $3 \pm 43\%$ lower after gadoteridol (paired t-test $p = 0.5$, n = 4). These results indicate efficacy and specificity of ParaMus-dependent neural inactivation consistent with the neurophysiology of the somatosensory system.

The quintessential functionality afforded by ParaMus is an ability to relate differences in neuromodulator infusion profiles to resulting neurophysiological outcomes. In the experiments of **Fig. 2d,e**, ParaMus infusion covered a distribution of areas in and around VPL (**Fig. 2f** and **Supplementary Fig. 4**). Variations in the infusion profile among individuals could be detected by T_1 -weighted imaging, revealing the extent to which apparently equivalent injection procedures lead to different results. For instance, a failed infusion could be detected by the absence of T_1 enhancement, as well as corresponding fMRI response changes (**Fig. 2g**). Premature infusion of ParaMus could be detected as T_1 contrast or relaxation changes prior to purposeful injection (**Fig. 2h** and **Supplementary Fig. 5**). Anomalous infusion profiles arising from subtle differences in cannula placement or convection dynamics could also be recognized (**Fig. 2i**). T_1 -weighted MRI readouts therefore provide instant feedback on the characteristics of neuromodulatory drug delivery, with the potential to guide experimental strategies. Quantitative analysis of ParaMus-mediated T_1 changes and corresponding effects in fMRI reveals a significant (correlation coefficient = 0.70, $p = 0.04$, n = 9) and approximately linear relationship between the extent of fMRI responses in S1FL and the percentage of sensory thalamus infused with ParaMus (**Supplementary Fig. 6**).

Another key capability ParaMus provides is the possibility of relating drug distribution profiles at multiple time points to responses observed during and after infusion. In a representative animal, a decrease in fMRI responses to forepaw stimulation can be detected progressively throughout ParaMus infusion, followed by a partial recovery as the drug begins to wash out (**Fig. 3a**). Evaluation of T_1 relaxation rate time courses in such experiments also enables in vivo estimation of the half-life for elimination of ParaMus from the brain (**Fig. 3b** and **Supplementary Fig. 7**), a value of approximately 30 minutes. Postmortem analysis of brain tissue after an imaging experiment permits identification of ParaMus by mass spectrometry and reveals that the contrast agent remains intact during the experimental period (**Supplementary Fig. 8**).

Discussion

These results demonstrate that ParaMus combines the pharmacological properties of muscimol with the MRI properties of commercial contrast agents, enabling imaging-based assessment and control over neural manipulations in the living brain. The reagent is straightforward to produce and apply, and could immediately be used in a range of biomedical contexts and in species ranging from rodents to primates, possibly including human subjects. In addition to fMRI responses like those examined here, other physiological and behavioral measures could also be investigated in conjunction with ParaMus-mediated perturbations, as long as MRI mapping of the drug distribution is performed soon before or after the relevant experiments. Non-MRI activity measurements are most feasible in the immediate vicinity of ParaMus infusion, where fMRI signal might be distorted by the contrast agent's magnetic susceptibility. The closest alternative to ParaMus-based procedures introduced here is afforded

by mixing muscimol with conventional MRI contrast agents like gadoteridol⁸, but the properties of such admixtures are considerably inferior. Muscimol and gadoteridol differ in molecular weight by a factor of five, and while muscimol is positively charged at pH 7, gadoteridol is neutral. Diffusion, molecular adhesion, cell uptake, and pharmacokinetics of the two compounds are likely to differ substantially, raising interpretive questions that are avoided when using ParaMus.

In future work, the idea of conjugating paramagnetic moieties to neuromodulatory agents could be extended to create additional MRI-detectable drugs. Construction of ParaMus exploits the fact that modification of the muscimol amine does not compromise pharmacological activity, but additional neurotransmitter receptor ligands also possess sites where modification is possible without abrogating receptor affinity⁹⁻¹¹. A toolkit of imageable drugs could potentially be multiplexed by attaching different types of contrast agent—for instance employing T_1 vs. transverse relaxation (T_2) or chemical exchange saturation transfer (CEST) contrast-inducing moieties—to different neuromodulatory substances. The approach presented here may therefore promote an unprecedented level of informed, multimodal control over neural function in deep tissue.

Methods

Reagents and general chemical methods

All solvents were of reagent grade and all other materials were purchased and used as received. Chemicals were procured from Sigma Aldrich (St. Louis, MO) unless otherwise noted. Compound **5** was procured from Macrocyclics (Plano, TX). Silica gel (230-400 mesh, VWR, Radnor, PA) and octadecyl-functionalized silica gel (RP-18, Waters, Milford, MA) were used for

column chromatography. Analytical thin layer chromatography was performed by using Merck 60 F254 silica gel (precoated aluminum sheets, 0.25 mm thick). Reverse phase preparative high-performance liquid chromatography (HPLC) traces were recorded at 298 K using a Waters (Milford, MA) HPLC system equipped with a semi-preparative C18 column. A gradient elution with a solvent system composed of water/acetonitrile with 0.1% trifluoroacetic acid (TFA) was applied for a total run time of 33 min.

Mass spectrometry

Both standard and high-resolution electrospray mass spectrometry were recorded on an Agilent Technologies (Santa Clara, CA) HP 8453 spectrometer, operating in positive or negative ion mode as stated, with MeOH as the carrier solvent. Matrix-assisted laser desorption ionization time of flight (MALDI-TOF) mass spectra were recorded on a Bruker Instruments (Ettlingen, Germany) MicroFlex instrument with α -cyano-4-hydroxycinnamic acid employed as the matrix and 50/50 water/acetonitrile + 0.1% TFA used to prepare all samples.

Elemental analysis

Absolute concentrations of final purified complexes for *in vitro* and *in vivo* studies were calculated by gadolinium content using inductively coupled plasma mass spectrometry on a Agilent 7900 ICP-MS instrument. Complexes were digested in concentrated nitric acid at 70 °C for 2 hours, before being diluted into 2% nitric acid at a working gadolinium concentration of 10-100 ppb. Gadolinium concentration was calibrated with 9 data points across the range of 1-500 ppb using known stock concentrations. 10 ppb erbium was used in all samples as an internal standard. Each sample was prepared in triplicate and each data point was measured in duplicate.

NMR spectroscopy

^1H and ^{13}C NMR spectra of each compound were recorded in commercially available deuterated solvents on a Bruker Avance III DPX 400 (^1H at 400 MHz, ^{13}C at 101 MHz). All chemical shifts are given in ppm and coupling constants are in Hz.

Synthetic methods

Further detailed information regarding the synthesis and characterization of Paramus (7) and related compounds are reported as Supplementary Information.

In vitro MRI

MRI data were acquired in a 12 cm outer diameter birdcage transceiver for imaging at room temperature in a 20 cm bore Bruker 7 T Avance III MRI scanner. Samples at varying concentrations in 20 mM 4-(2-hydroxyethyl)-1-piperazineethanesulfonic acid (HEPES) buffer, pH 7.4, were loaded into a 384-well clear polystyrene plate (Thermo Fisher Scientific, Waltham, MA), which had been pre-cut in half to optimally fit the coil. Unused wells were filled with buffer. 2 mm slices were imaged through the samples with a field of view (FOV) of 5×5 cm and data matrix of 256×256 points. Data for longitudinal (r_1) and transverse (r_2) relaxivity measurements were acquired using a multi-slice multi-echo pulse sequence (echo time, $TE = 12\text{-}360$ ms, repetition time, $TR = 100, 200, 300, 400, 500, 600, 700, 800, 900, 1000, 1200, 1500, 3000, 5000$ ms). Custom routines written in MATLAB (Mathworks, Natick, MA) were used to reconstruct the images and compute relaxation time constants by fitting image intensity data to exponential decay curves. Relaxivity values were then computed from the slope of T_1 and T_2 relaxation rates versus

contrast agent concentration, as determined by ICP-MS. Values of $r_1 = 5.0 \pm 0.2 \text{ mM}^{-1}\text{s}^{-1}$ and $r_2 = 7.3 \pm 0.6 \text{ mM}^{-1}\text{s}^{-1}$ were obtained for ParaMus, where the error margins represent SEM of $n = 3$ measurements.

Animals

All animal procedures were performed in strict compliance with US Federal guidelines, with oversight by the MIT Committee on Animal Care. A total of nine male Sprague-Dawley rats (300-400 g), purchased from Charles River Laboratories (Wilmington, MA), were used for the *in vivo* data presented in this paper. The animals were housed and maintained on a 12 h light/dark cycle with *ad libitum* access to food and water. Sample sizes for animal experiments were chosen to ensure reproducibility and quantify observed effects, rather than to guarantee recognition of pre-specified effect sizes with a given level of power. Experiments were not randomized or blinded.

Electrophysiology

Cortical neurons from E18 Sprague-Dawley rat embryos were kindly provided by the laboratory of Elly Nedivi (Picower Institute for Learning and Memory). The cells were seeded at 1.5×10^5 cells per 18 mm on #1 round coverslips coated with laminin (Life Technologies, Woburn, MA) and poly-D-lysine (Sigma-Aldrich, St. Louis, MO). Prior to electrophysiological measurements, cells were incubated in 2% B-27 supplement and 1% GlutaMAX (Thermo Fisher Scientific) for seven days. Recordings were performed at room temperature from neurons in extracellular solution containing 145 mM NaCl, 5 mM KCl, 1 mM MgCl₂, 1 mM CaCl₂, 5 mM HEPES, 5 mM glucose, 20 mM sucrose, 0.25 mg/L phenol red, and 10 μM D-serine (all materials from Sigma-Aldrich). The pH of this solution was adjusted to 7.4 with NaOH, and its osmolarity

was adjusted to 315 mOsm with sucrose. Electrodes were pulled in two stages from borosilicate glass capillaries (A-M systems, Sequim, WA) using a horizontal pipette puller (PD-97, Sutter instruments, Novato, CA), resulting in resistances of 8-12 M Ω when filled with an internal solution containing 145 mM KCl, 10 mM HEPES, 5 mM adenosine triphosphosphate, 0.2 mM guanosine triphosphate, and 10 mM ethylene glycol-bis(β -aminoethyl ether)-*N,N,N',N'*-tetraacetic acid, adjusted to pH 7.2 with KOH. Whole-cell current-clamp recordings were performed using AxoClamp 1B amplifier (Axon Instruments, Union City, CA). Cell membrane potentials were initially set to -60 mV, and voltage response to 50 ms current pulses of increasing amplitude, in 0.1 nA steps, were used to assess action potential thresholds and input resistances. To determine the effects of pharmacological agents, this procedure was performed following bath application of 10 μ M muscimol (Sigma-Aldrich), 10 μ M gadoteridol (Sigma-Aldrich), or 10 μ M ParaMus.

Surgical methods

In preparation for imaging experiments with intracranially-infused ParaMus or control agents, rats were implanted with infusion cannulae targeting VPL. Animals were anaesthetized with 2% isoflurane, shaved, and mounted in a rodent stereotaxic device (David Kopf Instruments, Tujunga, CA). Heart rates and blood oxygenation levels were monitored by a pulse oximeter (Nonin Medical, Plymouth, MN). Each rat was given a subcutaneous injection of slow-release buprenorphine (MIT pharmacy) at a dose of 1 mg/kg for analgesia at the beginning of surgery. The scalp was retracted and 28G holes were drilled into the skull 3.2 mm posterior and 3 mm lateral to bregma, unilaterally or bilaterally, with coordinates based on a standard rat brain atlas¹². 28G cannula guides (Plastics One, Roanoke, VA) designed to project 2 mm below the surface of the skull were implanted and secured using C&B Metabond dental cement (Parkell, Edgewood, NY).

Small plastic head-posts were implanted to facilitate head fixation during the MRI experiments. Finally, 32G dummy cannulae designed to fit the guide cannulae were inserted to protect the openings when not in use. Rats were allowed to recover from surgery for at least three days before imaging.

In vivo MRI

Immediately prior to imaging experiments, cannula-implanted rats were briefly anesthetized using 3% isoflurane and maintained at 2% isoflurane during preparation. Animals were intubated and ventilated, and an intraperitoneal catheter was established for drug delivery. Animals were then placed onto a cradle and secured in place via screws that attached to the implanted head-post. Isoflurane was discontinued and intraperitoneal bolus doses of 0.1 mg/kg dexdomitor (MIT pharmacy) and 1 mg/kg pancuronium (Sigma-Aldrich) were administered, followed by continuous delivery of 0.2 mg/kg/h dexdomitor and 2 mg/kg/h pancuronium thereafter. Respiration, heart rate, and blood oxygen saturation were monitored, and temperature was maintained with a circulating warm water pad (Gaymar, Orchard Park, NY) for the remainder of the procedures. 32G internal cannula (Plastics One) preloaded with 1 mM ParaMus, 1 mM gadoteridol, or saline vehicle were inserted at this time, targeting VPL via the previously implanted guide cannulae. Internal cannulae extended 5-6 mm below the brain surface. Animals were then inserted into the MRI scanner.

In vivo imaging was performed using a 9.4 T Biospec MRI scanner (Bruker) scanner operating with a cross coil volume transmit, surface receive configuration. A rapid acquisition with refocused echoes (RARE) pulse sequence were used to acquire T_2 -weighted anatomical images, with number of averages (NA) = 4, matrix size = 256×192 , FOV = $2.56 \text{ cm} \times 1.28 \text{ cm}$, slice thickness = 1 mm, $TR = 5000 \text{ ms}$, effective $TE = 30 \text{ ms}$, and RARE factor = 8. To quantify the

extent of ParaMus infusion, T_1 -weighted RARE images were also acquired, using $NA = 6$, matrix size = 128×64 , FOV = $2.56 \text{ cm} \times 1.28 \text{ cm}$, slice thickness = 1 mm , $TR = 252 \text{ ms}$, and effective $TE = 5 \text{ ms}$. For T_1 mapping, data were acquired with additional TR values of 429, 600, 900, 1000, 1500, 2000, 2500, and 3000 ms. For functional imaging, echo planar imaging (EPI) image series were acquired during alternating blocks of forepaw stimulation and rest. EPI scan parameters were $NA = 1$, matrix size = 64×32 , FOV = $2.56 \text{ cm} \times 1.28 \text{ cm}$, slice thickness = 1 mm , $TR = 2000 \text{ ms}$, and effective $TE = 16 \text{ ms}$.

Forepaw stimulation itself was performed using 9 Hz pulse trains with 1 ms pulse width and current of 3-6 mA. Forepaw stimulation blocks were 10 s long, and were delivered in ten cycles with 40 s rest periods in between. In two animals, forepaw imaging trials were performed repeatedly, every 30 minutes, along with T_1 mapping to determine the time course of ParaMus washout and corresponding changes in fMRI responses. In seven animals, measurement of fMRI responses before vs. after ParaMus infusion was performed in parallel with measurement of fMRI responses before vs. after control treatment with saline or gadoteridol. In these cases, test and control solutions were delivered via bilateral cannulae inserted in opposite hemispheres, and corresponding contralateral forepaws were stimulated in each case. Four animals that experienced suboptimal ParaMus targeting were excluded from the group data quantifying the efficacy of VPL ParaMus delivery (Fig. 2d), but were included in Supplementary Fig. 6, which specifically relates variation in ParaMus delivery to differences in the effects on fMRI responses.

MRI Data Analysis

Images were reconstructed using Paravision software (Bruker) and further analyzed using custom routines implemented in MATLAB. Preprocessing of functional imaging data was

performed using the AFNI software package (National Institute of Mental Health, Bethesda, MD)¹³. Steps included motion correction using a rigid-body volume registration algorithm, spatial and temporal smoothing, voxel-wise intensity normalization, and segmentation of brain from non-brain voxels. To coregister images into a uniform space, a reference anatomical scan was first manually aligned to a digitized version of a standard rat atlas¹². All other anatomical scans were then aligned to the reference image using a nine-parameter affine transformation implemented in AFNI. Each animal's EPI scans were aligned to the corresponding coregistered anatomical scan. The time series data from the EPI scans were smoothed with a Gaussian spatial kernel of 1 mm full width at half-maximum prior to statistical analysis, and each voxel time course was subsequently temporally smoothed using a sliding box window of width 3.

Initial statistical analysis of preprocessed EPI scans was performed in AFNI. Regression coefficients for activation maps were computed by convolving the electrical forepaw stimulus times with a hemodynamic response model. Six motion correction parameters were included from each animal as nuisance regressors. Outlier scans detected by median absolute deviation from time series trends in each data set were censored from the analysis.

Response amplitudes and t statistics for voxels that fell within the atlas-defined somatosensory cortex¹² were used as input for further analysis of fMRI results in MATLAB. To generate response maps such as Fig. 2b, the response in units of percent signal change (%SC) was indicated for all voxels whose p value was below an uncorrected significance threshold of 0.05. To generate time courses in Fig. 2c, responses were averaged over all voxels meeting the significance criterion prior to ParaMus infusion. To generate the difference maps in Fig. 2d, the percent signal change estimated by general linear modeling to a stimulus regressor before injection was subtracted from the percent signal change observed after injection on a voxel-by-voxel basis.

To compensate for variability in the pre-treatment response amplitudes among animals, difference maps from each animal were normalized to the peak values observed before treatment and then averaged across the animals. Thus, blue corresponding to a value of -1 indicates complete abrogation of the response on average, as a result of treatment. The time courses of Fig. 2e were computed by similarly normalizing each time course to the peak value observed in the pre-injection condition, followed by averaging over voxels in S1FL and then over animals. Error margins reported in each case represent the standard error of the mean over animals ($n = 5$ for ParaMus treatment and $n = 4$ for gadoteridol control treatment).

Maps of contrast agent-dependent signal change in T_1 -weighted MRI scans, such as Fig. 2f, were computed on by applying the formula $\%SC = 100 \times (S_{post} - S_{pre})/S_{pre}$ on a voxel-wise basis, where S_{pre} and S_{post} are the signal amplitudes observed before and after infusion, respectively. These maps were averaged over animals ($n = 5$). Maps of T_1 and $R_1 (= 1/T_1)$ were computed by exponential fitting to T_1 -weighted data acquired at multiple TR values, as specified above. Values were averaged across sensory thalamus (VPL and ventroposterior thalamus, a total of 40 voxels) to obtain reported means. Correspondence of ParaMus injection spread and fMRI activation extent was examined by computing the percentage of sensory thalamus filled during ParaMus infusion, and plotting this against the percent change in the number of voxels showing significant (F -test $p < 0.05$) stimulus-dependent modulation after vs. before infusion.

Analysis of ParaMus in injected brain tissue

A rat was sacrificed and perfused with NaCl solution (0.9%) approximately 1 h after ParaMus infusion as described above. The collected brain sample was dounced in methanol (5 mL) for 5 min and centrifuged at 3000g for 10 min. The supernatant was collected and the residue was

dounced again in methanol for 1 min and centrifuged for another 10 min at 3000g. This procedure was repeated two further times. All collected methanol supernatant fractions were pooled and filtered through a 0.2 μm filter. The resulting clear solution was concentrated to dryness under vacuum, dissolved in 500 μL deionized water, and filtered through a 3 kDa cutoff filter. The filtrate was then concentrated to 250 μL under vacuum and analyzed using an Agilent 6125B mass spectrometer attached to an Agilent 1260 Infinity LC system.

Code availability statement

Scripts used for data analysis are available upon reasonable request.

Data availability statement

Raw MRI datasets generated during and/or analyzed during the current study are available from the corresponding author on reasonable request.

Acknowledgements

The authors acknowledge grants from the National Institutes of Health (R01 DA038642, UF1 NS107712, and U01 NS103470) and the Simons Center for the Social Brain to AJ. SB was also supported by the MIT Neurobiological Engineering Training Program (NIH T32 EB019940). PH was funded by a Wellcome Trust-MIT Fellowship (105932/Z/14/Z). The authors are grateful for primary neurons kindly donated by Elly Nedivi, Mette Rathje, and Hannah Waxman.

References

- Boyden, E.S., Zhang, F., Bamberg, E., Nagel, G. & Deisseroth, K. Millisecond-timescale, genetically targeted optical control of neural activity. *Nat Neurosci* 8, 1263-1268 (2005).
- Alexander, G.M. et al. Remote control of neuronal activity in transgenic mice expressing evolved G protein-coupled receptors. *Neuron* 63, 27-39 (2009).
- Daly, C.J. & McGrath, J.C. Fluorescent ligands, antibodies, and proteins for the study of receptors. *Pharmacol Ther* 100, 101-118 (2003).
- Dierckx, R.A.J.O., Otte, A., de Vries, E.F.J., van Waarde, A. & Luiten, P.G.M. (eds.) *PET and SPECT of Neurobiological Systems*. (Springer-Verlag, Berlin; 2014).
- Wang, H., Standifer, K.M. & Sherry, D.M. GABA(A) receptor binding and localization in the tiger salamander retina. *Vis Neurosci* 17, 11-21 (2000).
- Tweedle, M.F. The ProHance story: the making of a novel MRI contrast agent. *Eur Radiol* 7 Suppl 5, 225-230 (1997).
- Hyder, F., Behar, K.L., Martin, M.A., Blamire, A.M. & Shulman, R.G. Dynamic magnetic resonance imaging of the rat brain during forepaw stimulation. *J Cereb Blood Flow Metab* 14, 649-655 (1994).
- Wilke, M., Turchi, J., Smith, K., Mishkin, M. & Leopold, D.A. Pulvinar inactivation disrupts selection of movement plans. *J Neurosci* 30, 8650-8659 (2010).
- Bartels, E., Wassermann, N.H. & Erlanger, B.F. Photochromic activators of the acetylcholine receptor. *Proc Natl Acad Sci U S A* 68, 1820-1823 (1971).
- Volgraf, M. et al. Allosteric control of an ionotropic glutamate receptor with an optical switch. *Nat Chem Biol* 2, 47-52 (2006).
- Donthamsetti, P.C. et al. Optical Control of Dopamine Receptors Using a Photoswitchable Tethered Inverse Agonist. *J Am Chem Soc* 139, 18522-18535 (2017).
- Paxinos, G. & Watson, C. *The Rat Brain in Stereotaxic Coordinates*, Compact 6th Ed. (Academic Press, Boston; 2009).
- Cox, R.W. AFNI: software for analysis and visualization of functional magnetic resonance neuroimages. *Comput Biomed Res* 29, 162-173 (1996).

Figures

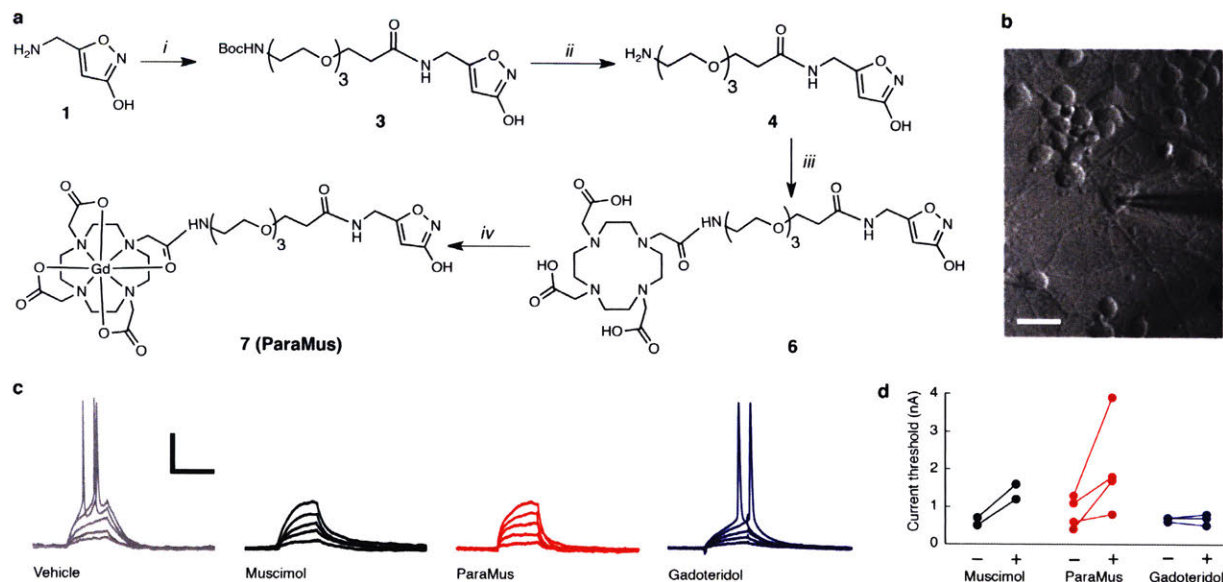


Figure 1. Synthesis and pharmacological characterization of ParaMus. (a) Chemical synthesis of ParaMus (7): *i*) HOOC-PEG3-NHBoc, EDC/NHS, MOPS (100 mM, pH 5.5), *ii*) TFA/DCM (80:20), *iii*) DOTA-NHS, MOPS (25 mM, KCl 100 mM, pH 8), *iv*) GdCl₃, H₂O, pH 5.5. (b) Setup for intracellular recording of primary rat cortical neurons (scale bar = 10 μm). (c) Representative current clamp recordings in response to injection of 0.1-0.5 nA current injection in the presence of vehicle, 10 μM muscimol, 10 μM ParaMus, and 10 μM gadoteridol. Scale bars, horizontal = 20 ms, vertical = 10 mV. (d) Current thresholds for action potential generation before (-) and after (+) application of muscimol, ParaMus, or gadoteridol. Paired measurements shown for two (muscimol), four (ParaMus), or three (gadoteridol) independent experiments.

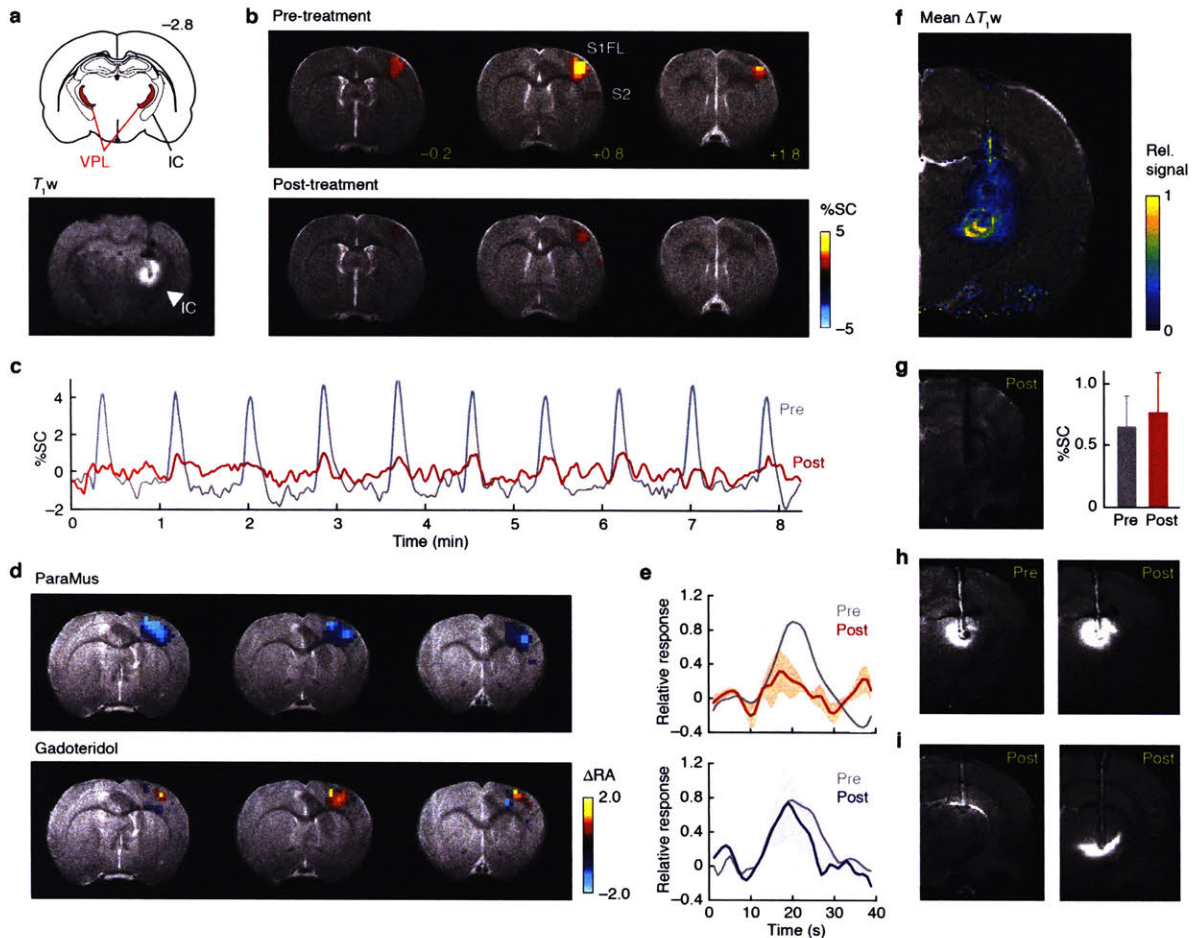


Figure 2. Image-guided manipulation of somatosensory responses in the rat brain. (a) Top: Coronal brain schematic¹² at bregma = -2.8 mm, showing the location of VPL (red) bordered on the lateral side by the internal capsule (IC). Bottom: a corresponding T_1 -weighted (T_1w) coronal image showing contrast enhancement in the VPL region following ParaMus infusion. Hypointense white matter IC signal denoted by arrowhead. (b) Forepaw stimulation-induced fMRI responses, in units of percent signal change (%SC), in a single animal before (top) and after (bottom) the ParaMus infusion shown in (a). S1FL and S2 regions labeled; bregma coordinates in yellow. (c) Time course of fMRI signal in the S1FL region pre- (gray) and post-infusion (red), corresponding to data in (b); stimulation blocks denoted by blue rectangles. (d) Change in fMRI response amplitudes (ΔRA), relative to pre-treatment responses, after VPL-targeted ParaMus infusion (top, $n = 5$) or control infusion with gadoteridol (bottom, $n = 4$). (e) Mean relative peristimulus response time courses associated with the maps in (d), pre- and post-treatment with ParaMus (top) or gadoteridol (bottom). Shading denotes SEM over 5 animals (top) or 4 animals (bottom). (f) Profile of mean relative T_1 -weighted MRI signal changes following ParaMus infusion in 5 animals. Control infusions lacking contrast agent produced no notable contrast enhancement. (g) A failed ParaMus infusion results in no enhancement in the post-treatment condition (left). Correspondingly, there is no decrease in fMRI response to forepaw stimulation after treatment (right); error bars denote SEM of responses over 10 stimulus cycles in a single animal. (h) Premature infusion of ParaMus is easily detectable by comparing pre- and post-treatment T_1 -

weighted images. **(i)** Anomalous spatial distributions of ParaMus are recognized in images of two separate animals in the post-infusion condition.

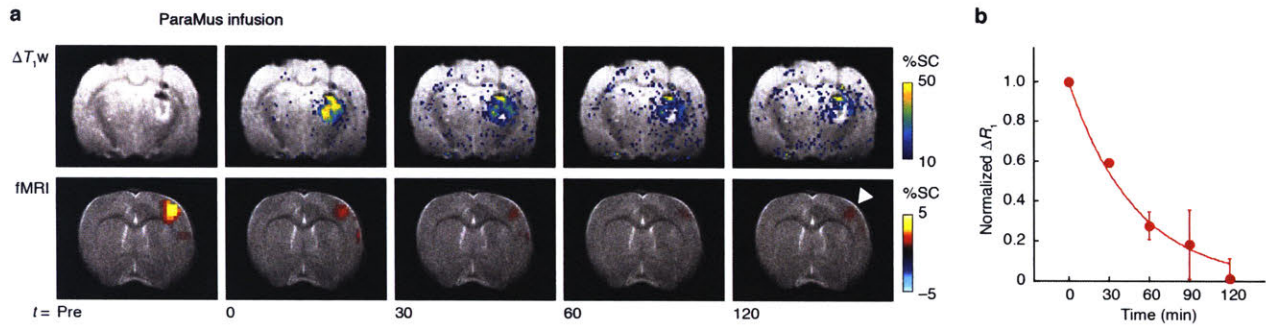
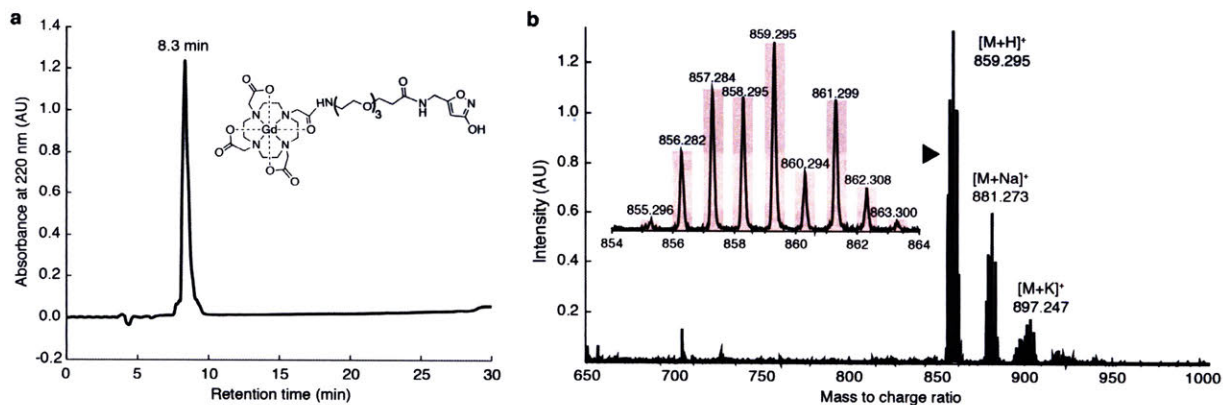
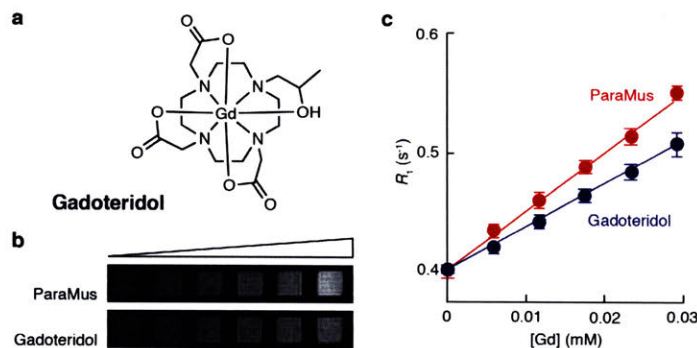


Figure 3. Time course of ParaMus-induced T_1 contrast and fMRI response changes. (a) Maps showing infusion of contrast agent (top, bregma = -2.8 mm) and fMRI responses (bottom, bregma $+0.8$ mm) as a function of time in the subject of Fig. 2b. Data are shown before (Pre) and after ParaMus infusion, as indicated by time points (t) in minutes shown below the images. The infusion maps display the change in T_1 -weighted signal (ΔT_{1w}) due to ParaMus infusion, in units of percent signal change (%SC) compared with pre-infusion contrast, overlaid on an anatomical image. The fMRI activation maps indicate mean response amplitudes induced by forepaw stimulation in 8.4-minute trials beginning at each of the designated time points. Note the slight recovery of the S1FL response peak at the 120 minute time point (arrowhead), after ParaMus contrast has largely dissipated, a result replicated also in a second animal. A small amount of ParaMus leakage is also detectable as ΔT_{1w} hyperintensity around the needle in the Pre image. **(b)** Washout of ParaMus following infusion into brain, as reflected by the normalized change in T_1 relaxation rate (R_1) with respect to pre-infusion conditions averaged over sensory thalamus. Values indicate mean and SEM (error bars) of data from two animals. The data are fit by an exponential decay curve (shown) with half life 34 min.

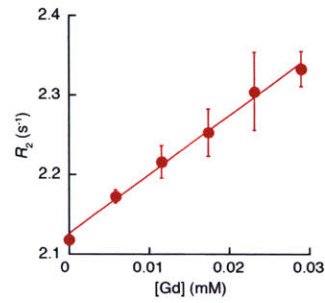
Supplementary Figures



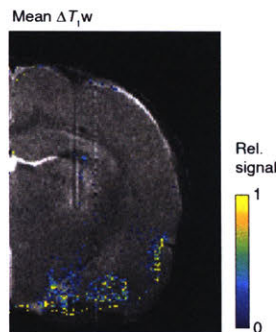
Supplementary Figure 1. Mass and purity of ParaMus. (a) HPLC trace demonstrating retention time (8.3 min) and purity of ParaMus (inset), as indicated by absorbance at 220 nm. (b) Matrix assisted laser desorption ionization time of flight (MALDI-TOF) mass spectrum of ParaMus. The inset magnifies the peak associated with the presumed $[M^{ParaMus}+H]^+$ species, and the light red boxes indicate the theoretical isotopic pattern, confirming identity of the compound.



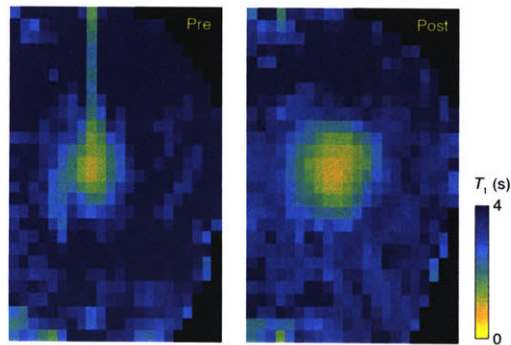
Supplementary Figure 2. Longitudinal relaxivity of ParaMus and gadoteridol. (a) Structure of gadoteridol, which approximates the neutral gadolinium DOTA moiety of ParaMus. (b) Images of successive concentrations of ParaMus and gadoteridol (0–30 μ M) imaged using T_1 -weighted MRI at 7 T and room temperature in 100 mM HEPES, pH 7.4. (c) T_1 -weighted MRI data were used to compute longitudinal relaxation rates (R_1) for ParaMus (red) and gadoteridol (blue) solutions, as a function of concentration. Error bars indicate SD of three measurements each. Slopes of these datasets give estimated r_1 values of 5.0 ± 0.2 $\text{mM}^{-1}\text{s}^{-1}$ for ParaMus and 3.6 ± 0.3 $\text{mM}^{-1}\text{s}^{-1}$ for gadoteridol.



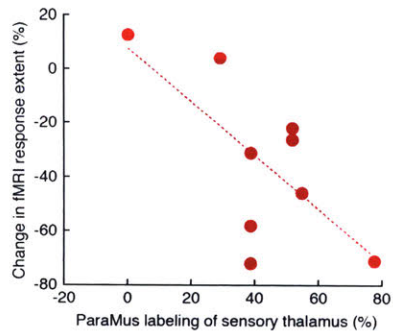
Supplementary Figure 3. Transverse relaxivity of ParaMus. Values of the transverse relaxation rate (R_2) are shown as a function of ParaMus at the gadolinium concentrations shown, measured by MRI at 7 T and room temperature in 100 mM HEPES, pH 7.4. Values indicate mean \pm SD of three measurements each.



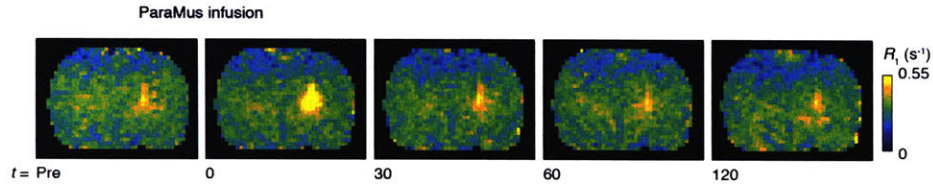
Supplementary Figure 4. Contrast enhancement due to VPL-targeted vehicle injection. A map of mean relative T_1 -weighted MRI signal changes following saline vehicle infusion in two animals, indicating that contrast changes observed in the analogous data of Fig. 2f require the presence of ParaMus.



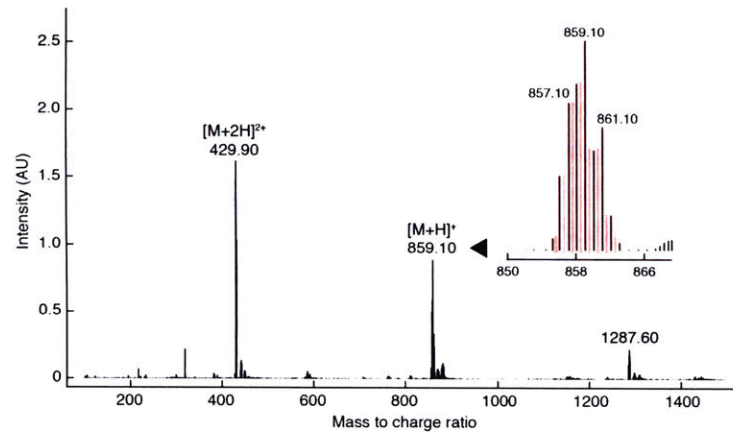
Supplementary Figure 5. T_1 maps indicating pre-infusion leakage of ParaMus. Longitudinal relaxation time (T_1) maps were obtained before (Pre, left) and after (Post, right) infusion of ParaMus in the animal subject of Fig. 2h. Low T_1 values in the center of the field of view in both Pre and Post conditions indicate the presence of contrast agent, corresponding to brightening seen in the analogous T_1 -weighted images.



Supplementary Figure 6. Correspondence between ParaMus delivery and fMRI effects. The extent of ParaMus infusion was estimated by computing the percentage of voxels in sensory thalamus that experienced an R_1 change over 20% during ParaMus infusion. The change in fMRI response was determined as the percent change in the number of voxels showing significant (F -test $p < 0.05$) stimulus-dependent modulation after vs. before ParaMus infusion. The dashed line indicates the least-squares linear fit, representing a significant correlation across nine animals with correlation coefficient = 0.70 and $p = 0.04$.

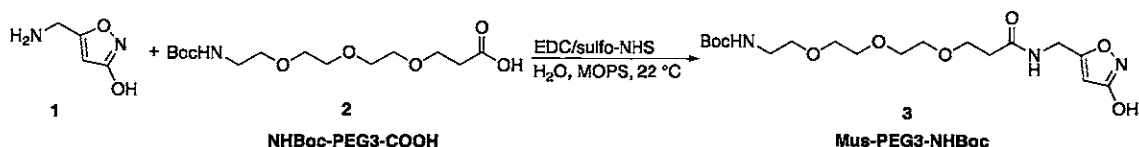


Supplementary Figure 7. Time course of ParaMus-induced T_1 relaxation changes. Coronal maps of the T_1 relaxation rate (R_1) throughout the brain slice in which ParaMus infusion was performed in the animal subject of Figure 3a (bregma = -2.8 mm). Data represent values both prior to (Pre) and at time points indicated in minutes after ParaMus infusion.

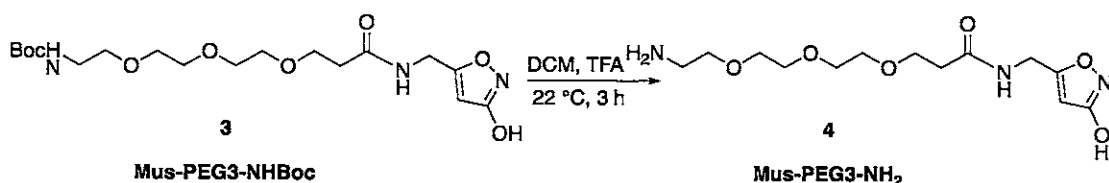


Supplementary Figure 8. Analysis of ParaMus in injected brain tissue. Brain tissue from a ParaMus-infused rat brain was homogenized and subjected to liquid chromatography mass spectroscopic analysis. Intact ParaMus was clearly recognizable from mass peaks corresponding to the $[M+H]^+$ species and $[M+2H]^{2+}$ species. Inset magnifies the peak associated with the $[M+H]^+$ species, highlighting correspondence of the theoretical isotopic pattern (pink boxes) with the observed peaks in black.

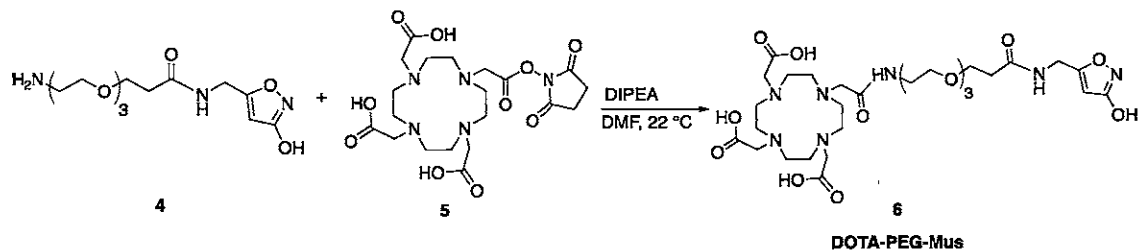
Supplementary Methods



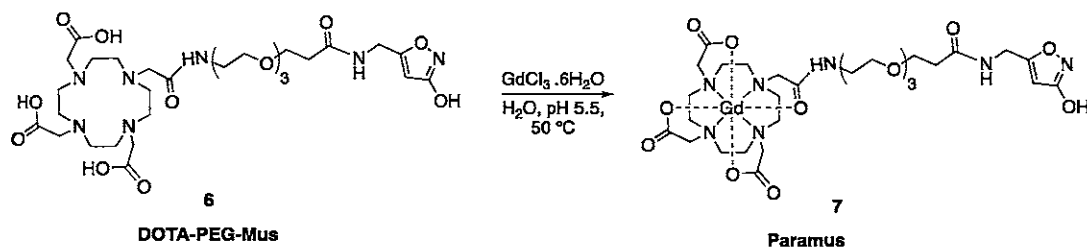
Mus-PEG3-NHBoc, 3. NHBoc-PEG3-COOH (**2**) (141 mg, 0.44 mmol) was dissolved in 3-(*N*-morpholino)propanesulfonic acid (MOPS) buffer (100 mM, pH 5.5) and 1-ethyl-3-(3-dimethylaminopropyl)carbodiimide (EDC) (168 mg, 0.88 mmol) and *N*-hydroxysulfosuccinimide (sulfo-NHS) (280 mg, 1.32 mmol) were added. The reaction solution was stirred at room temperature for 5 min and muscimol (**1**) (50 mg, 0.44 mmol) was added; the resulting clear solution was stirred at ambient temperature for 18 h. The reaction mixture was purified by preparative high performance liquid chromatography (HPLC) [silica-C18, eluent gradient H₂O:acetonitrile (MeCN) from 95:5 to 10:90]. Yield: 95 mg (68%). High resolution mass spectrometry (HRMS) with negative-mode electrospray ionization (ESI-) *m/z* calc. 416.203 for C₁₈H₃₀N₃O₈⁻ found 416.211 [M-H]⁻. ¹H nuclear magnetic resonance (NMR) (400 MHz, Methanol-*d*₄) δ 5.54 (s, 1H), 4.06 (s, 2H), 3.67 – 3.39 (m, 4H), 3.28 (d, *J* = 5.8 Hz, 4H), 3.22 – 3.15 (m, 4H), 2.91 (td, *J* = 5.6, 1.9 Hz, 4H), 2.60 (s, 1H), 2.24 (t, *J* = 6.3 Hz, 1H), 2.19 (t, *J* = 6.0 Hz, 3H), 1.12 (s, 9H). ¹³C NMR (101 MHz, Methanol-*d*₄) δ 175.23, 174.11, 171.99, 171.86, 94.51, 80.06, 70.99, 68.09, 67.75, 56.35, 43.57, 41.23, 37.46, 36.50, 35.75, 28.76.



Mus-PEG3-NH₂, 4. Compound **3** (60 mg) was suspended in dichloromethane (3 mL) and trifluoroacetic acid (3 mL) was added. The resulting solution was stirred at room temperature for 3 h. After removal of all volatiles in vacuum the resulting residue was dissolved in deionized water (3 mL) and freeze-dried to afford **4** as colorless oil. Yield: 38 mg (95%). HRMS (ESI+) *m/z* calc. 318.175 for C₁₃H₂₄N₃O₆⁺, found 318.166 [M+H]⁺. ¹H NMR (400 MHz, Methanol-*d*₄) δ 5.85 (s, 1H), 4.37 (s, 2H), 3.76 (t, *J* = 6.0 Hz, 3H), 3.70 (t, *J* = 5.0 Hz, 2H), 3.66 (s, 4H), 3.64 – 3.61 (m, 7H), 3.12 (t, *J* = 5.1 Hz, 2H), 2.51 (t, *J* = 6.0 Hz, 3H). ¹³C NMR (101 MHz, Methanol-*d*₄) δ 174.14, 172.07, 171.85, 94.56, 71.51, 71.37, 71.18, 71.17, 68.08, 67.82, 40.63, 37.30, 36.47.

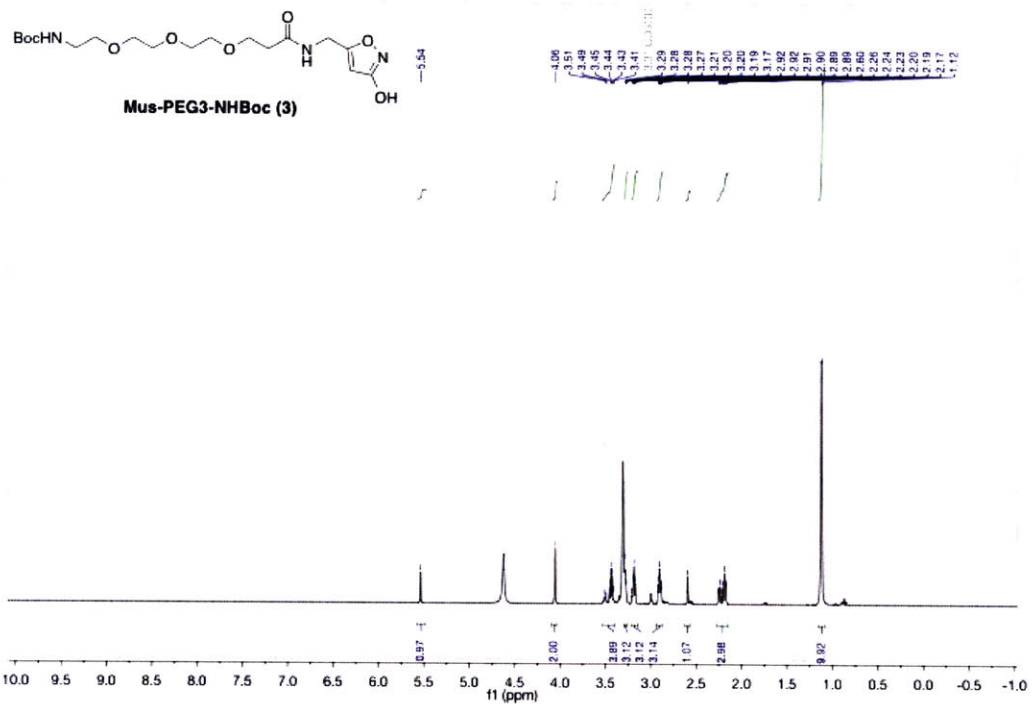


DOTA-PEG-Mus, 6. Compound **4** (30 mg, 0.09 mmol) and diisopropylethylamine (13 mg, 0.1 mmol) were dissolved in anhydrous dimethylformamide (3 mL) and **5** (68 mg, 0.09 mmol) was added. The reaction solution was stirred at room temperature for 20 h and after removal of all volatiles purified by HPLC (C18 coated silica, H₂O [0.1%v trifluoroacetic acid (TFA)]:MeCN (0.1%v TFA), 95:5 to 5:95 in 32 min, $R_t = 8.3$ min). Yield: 60 mg (85%). HRMS (ESI-) m/z calc. 702.331 for C₂₉H₄₈N₇O₁₃⁻, found 702.314 [M-H]⁻. ¹H NMR (400 MHz, Methanol-*d*⁴) δ 7.92-7.76 (m, 1H), 7.6-7.5 (m, 1H), 4.39 (s, 2H), 3.88-3.76 (m, 10H), 3.64 (s, 8H), 3.58 (t, 2H, $J_{\text{HH}} = 4$ Hz), 2.52 (t, 2H, $J_{\text{HH}} = 4$ Hz). ¹³C NMR (101 MHz, Methanol-*d*⁴) δ 172.72, 170.68, 170.56, 127.00, 125.85, 117.25, 110.02, 93.16, 70.14, 70.02, 69.84, 69.68, 68.90, 66.68, 54.43, 42.38, 38.97, 36.00, 35.14, 27.02, 17.30, 15.86.

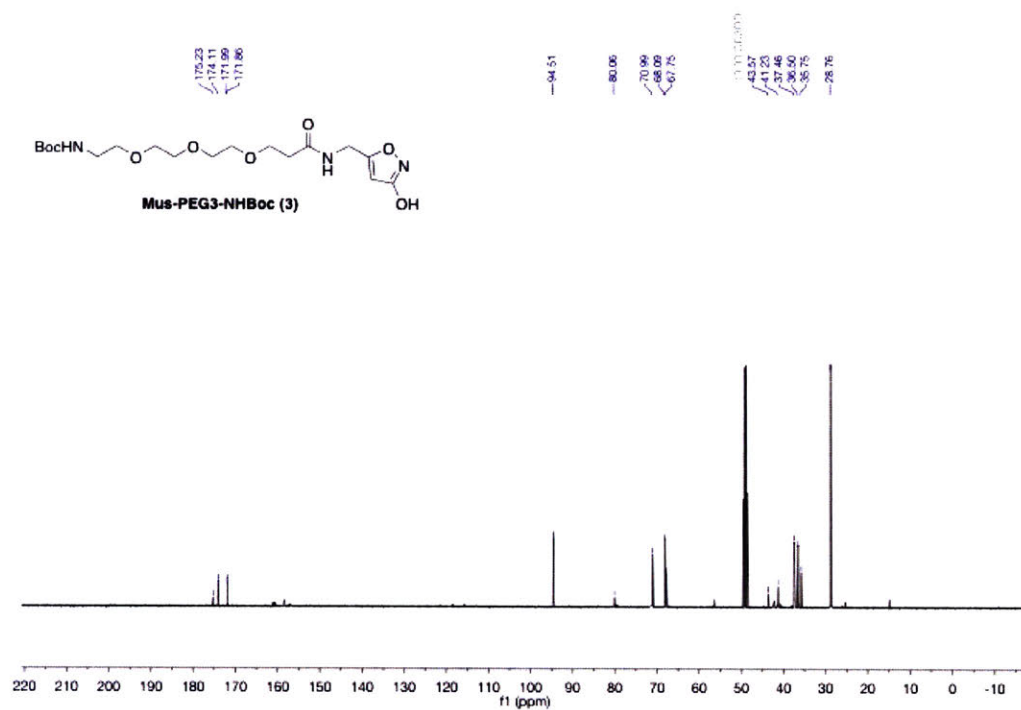


Paramus, 6. Gd(III)Cl₃·6H₂O (6.3 mg, 0.017 mmol) was added to a stirred solution of **5** (10.0 mg, 0.014 mmol) in water (2 mL) and the pH was adjusted to 5.5 using NaOH_(aq). The reaction was left stirring overnight at 50 °C. After cooling to rt, the pH was increased to 10 and the precipitated excess metal hydroxide was removed by centrifugation. The solution was adjusted back to pH 7 with HCl_(aq) and lyophilized overnight. The resulting white solid was purified by preparative HPLC (C18 coated silica, H₂O (0.1%v TFA):MeCN (0.1%v TFA), 95:5 to 5:95 in 32 min, retention time = 8.4 min). Yield: 6.5 mg (54%). MALDI-TOF m/z calc. 859.24729 for C₂₉H₄₇GdN₇O₁₃, found 859.29536 [M+H]⁺.

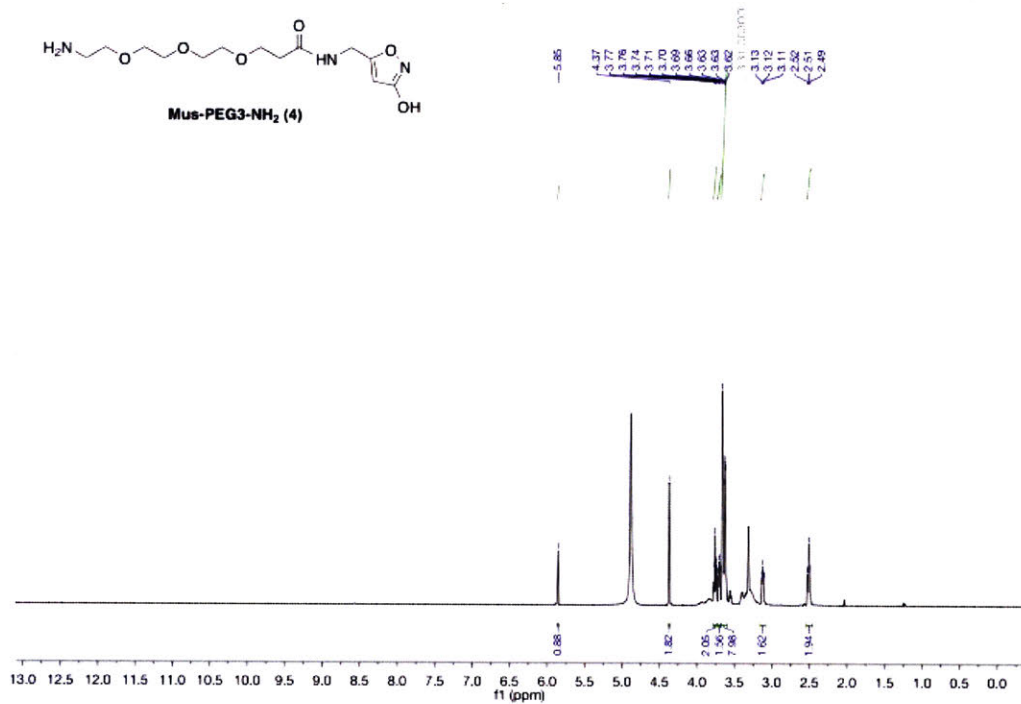
¹H NMR spectrum of Mus-PEG3-NHBoc



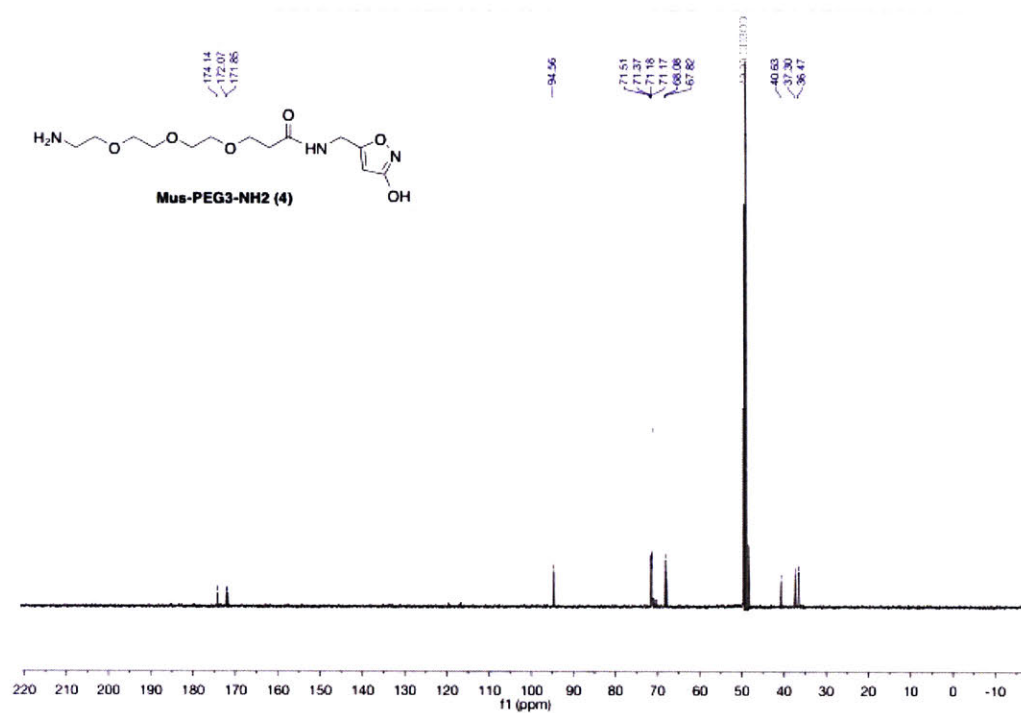
¹³C NMR spectrum of Mus-PEG3-NHBoc



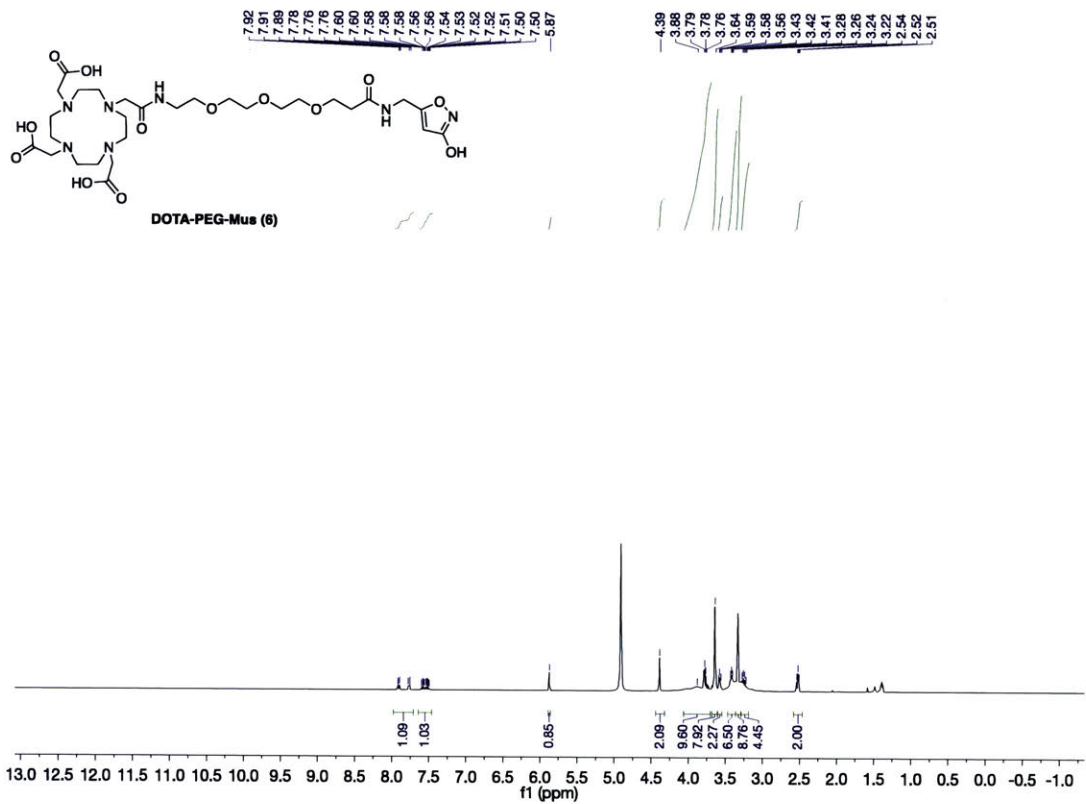
¹H NMR spectrum of Mus-PEG3-NH₂



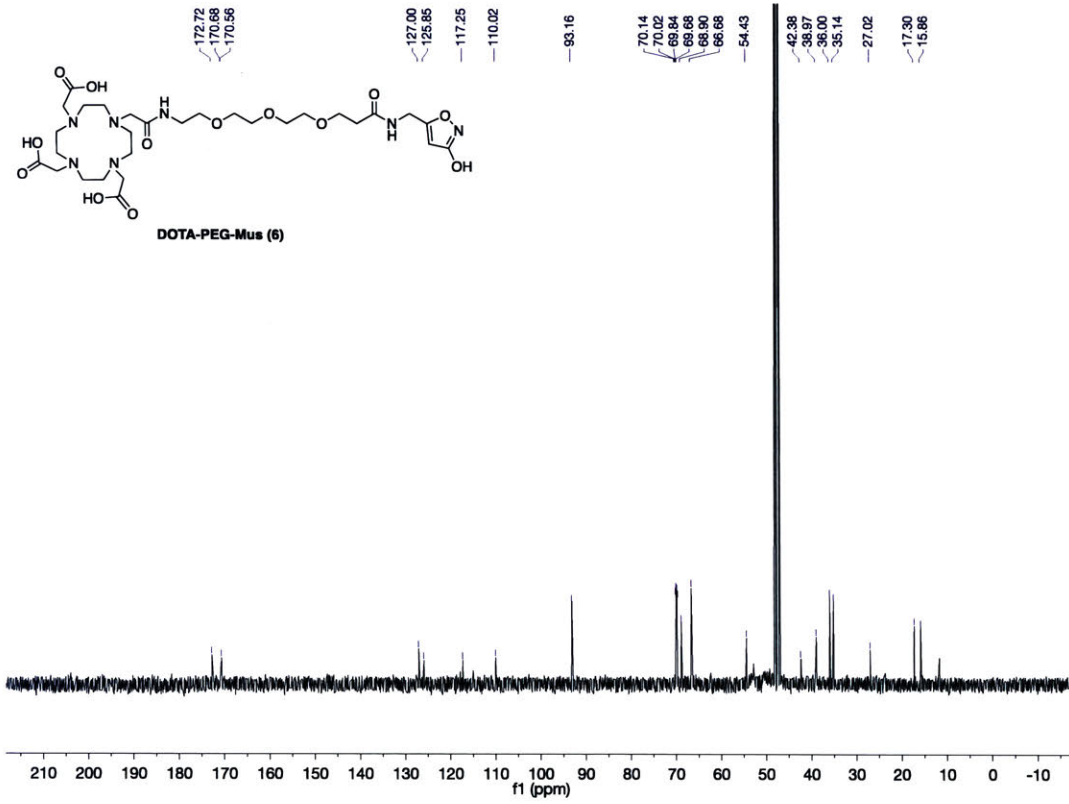
¹³C NMR spectrum of Mus-PEG3-NH₂



¹H NMR spectrum of DOTA-PEG-Mus



¹³C NMR spectrum of DOTA-PEG-Mus



Chapter 6

Summary and Future Directions

This chapter was written by Sarah Bricault with feedback from Alan Jasanoff.

Summary

Understanding how the brain as a whole processes inputs and uses that information to produce behaviors is the core, unifying goal of this thesis. Many experimental techniques require some degree of spatial selection that limits the regions of interest to one or a few that have been preselected based on prior studies. This makes it impossible to discover effects outside of this limited field of view. However, functional MRI (fMRI) enables the simultaneous study of whole-brain dynamics. This thesis takes advantage of that property to study behaviors and brain states in rats. Furthermore, new techniques and tools were developed which facilitate such studies.

Motivated behavior & decision making

One classic and well-defined behavior in experimental animals is intracranial self-stimulation (ICSS). Rats will repeatedly press a lever or poke in a nosepoke hole to receive electrical stimulation of the medial forebrain bundle (MFB). Rats are capable of discriminating between rewards of different values (i.e. stimuli of different frequencies or intensities) up to a threshold value. After that threshold value there is a plateau and animals will no longer prefer more intense stimuli over stimuli at the threshold value. In Chapter 2 of this thesis, we used fMRI to demonstrate that certain brain regions (most notably the nucleus accumbens) show activity profiles that mimic this threshold effect rather than showing monotonically increasing activity as the stimulus frequency is increased. Furthermore, inactivating the nucleus accumbens disrupts the threshold effect behaviorally. Animals whose nucleus accumbens has been inactivated are able to discriminate between rewards of arbitrarily large magnitudes.

From there, we progressed to examine a more complex form of decision-making behavior. Although some forms of decision-making do require an animal to select between rewards of different magnitudes, it is more common for one or both of the rewards in question to be accompanied by an aversive stimulus such as fear or pain. For example, an animal might need to decide between a high-value food item that incurs a risk of predation and a low-value food item in a comparably safer environment. Ultimately, much of decision-making behavior can be described as the weighted evaluation of positive and negative stimuli.

To model this complex behavior in a tractable way, we chose our rewarding and aversive stimuli carefully. We used intracranial stimuli that both produced a robust behavioral response in awake animals and could be delivered to anesthetized animals during functional MRI. The rewarding stimulus used was MFB stimulation, as described above. The aversive stimulus was dorsolateral periaqueductal gray (dlPAG) stimulation. The dlPAG is an important component of the descending pain modulatory pathway, and current stimulation of the dlPAG evokes well-defined behavioral responses.

The initial goal of the study was to have the animal select between a reward of value X_1 and a combined reward of value X_2 and aversive stimulus of value Y . We would then look for a ‘balance point’ where the animal did not discriminate between X_1 and $X_2 + Y$. For example, perhaps stimulating the MFB at 100 Hz would be equivalent to stimulating the MFB at 150 Hz and the dlPAG at the freezing threshold. This would provide us with three regimens to image—the rewarding stimulus alone, the aversive stimulus alone, and the ‘balance point’ where both rewarding and aversive circuitry were presumably engaged.

We started by answering what we thought would be a trivial question: does adding an aversive stimulus to a rewarding one make the reward less valuable? In nature, the answer is of

course yes. We performed this experiment by setting $X1 = X2$, so that the animal had to choose between $X1$ and $X1 + Y$, where Y varied between behaviorally relevant values. However, to our great surprise we found that the answer was in fact no for these specific stimuli. No matter how much we increased the aversive stimulus Y in this experiment, the animal had no apparent preference for one option or the other.

Although this derailed our initial plans to image the interaction of reward and aversion- since we found no such interaction- it also provided a fascinating result. Our behavioral results demonstrated that there were non-overlapping circuits governing reward and aversion that we had inadvertently tapped into in our selection of stimuli.

To further examine this phenomenon, we performed fMRI on animals receiving dlPAG or MFB stimulation alone and examined the maps for overlap. Again, we were surprised by the result. Instead of finding completely non-overlapping activation maps, there was in fact some overlap. In particular, the nucleus accumbens was activated by both stimuli. This indicates that the circuits mediating reward and aversion within the nucleus accumbens do not interact in a behaviorally relevant way.

Technique & tool development

One limitation of the aforementioned two studies is that the fMRI results were performed under isoflurane anesthesia. This was necessary because to image rats via fMRI one must prevent them from moving, which is typically accomplished by utilizing one of several anesthesia regimens. Unfortunately, the brain reacts differently under anesthesia and thus any results obtained under these conditions have reduced applicability to the awake brain. It is also

possible to physically restrain animals during fMRI, but even under optimal conditions this results in large motion artifacts, for example from the twitching of facial muscles.

To move past this tradeoff, we developed a procedure for performing fMRI of unanesthetized animals, under chemically-induced immobilization conditions that remove motion-related confounds. This permits acquisition of high-quality imaging data and maintains the applicability to the awake brain. We validated that that this technique indeed reduces motion artifacts, and demonstrated that after 3 days of acclimation animal stress hormones returned to baseline levels.

Finally, we applied this technique in two ways, both of which involved resting-state functional connectivity. When an animal is not performing any particular task or receiving specific inputs, we define the animal as being “at rest.” Resting state functional connectivity is disrupted in a number of neurological conditions. In rats, we assessed functional connectivity primarily by selecting a specific voxel to be a “seed” and examining how correlated the BOLD signal in that seed was to that of other voxels in the brain. Specifically, we looked at bilateral connectivity of the primary somatosensory barrel field cortex (S1BF), which is by far the easiest resting-state “network” to observe in rats.

Our first proof of concept was to compare seed-based functional connectivity of S1BF in awake versus anesthetized animals. We showed that there is reduced bilateral connectivity in S1BF under isoflurane anesthesia when the global signal is regressed out, which is consistent with prior studies.

The first application of this technique was in *Fmr1*KO animals. Humans who lack the *Fmr1* gene have a specific condition that includes often severe autistic phenotypes. One of the common phenotypes of autism is abnormal sensory processing. We thus hypothesized to see a

difference in S1BF bilateral connectivity in these animals when we performed resting-state scans. Indeed, we observed a marked decrease in S1BF bilateral connectivity.

A common reason for using animal models is the ability to perturb the system in ways that are not possible with human subjects. One standard neurobiological perturbation is the inactivation of brain regions of interest. For example, muscimol is a GABA-A agonist that inactivates brain structures when it is infused into them. However, as with many such agents, until now the distribution of the agent could only be determined post-mortem using brain slicing and staining techniques. Furthermore, the distortion of the brain tissue during histology and imperfect fixation techniques make it impossible to get a true representation of the distribution of the agent.

We came up with a novel solution to this problem. Conjugating an agent (in this case, muscimol) to a contrast agent visible by MRI would allow for real-time imaging of the distribution of the agent as it was injected. Using paramagnetic muscimol (ParaMus) as our test case, we created such an agent and verified that it retained its inactivating properties both in vitro and in vivo.

Thus, we utilized fMRI and behavioral analyses to further our understanding of motivated behavior and decision-making processes. Furthermore, we developed novel tools and techniques to make future studies of those processes easier to pursue.

Future Directions

Decision-making behavioral studies

In our study of decision-making behaviors, we found evidence for behaviorally distinct circuits controlling reward and aversion. However, we do not have any cell-specific information about these circuits.

One future direction would be to make use of optogenetic techniques. First, we would need to duplicate the behavioral findings using this alternate stimulation method. Then, we could study how information was traveling upstream from the dIPAG to the nucleus accumbens by differentially stimulating neurons that project from the dIPAG to different structures in the brain (whether the accumbens directly or one of several intermediate regions).

Another path forward would be to reattempt our initial goal of finding rewarding and aversive brain circuits that do overlap. We have made some initial attempts to identify alternate aversive-related structures in the brain, with limited success. In particular, only the dIPAG seems to have such a robust behavioral output. Thus, the next logical step would be to examine these putative aversive regions using a behavioral test that does not rely on dIPAG-specific behaviors. Conditioned place avoidance (CPA) with stimulation of the region as the aversive stimulus or active escape behavior (pressing a lever to terminate stimulation of the region) would be two excellent methods of assessment

Unanesthetized paralysis technique

One useful experiment would be to determine what being “at rest” really means for unanesthetized animals, whether they are paralyzed or not. In humans, we can at the very least tell if they have fallen asleep during the scan. It is more difficult to make this determination in

rodents, but it is possible using EEG recordings. By recording from animals either in the MRI machine or in mock-MRI environments, we can establish the frequency of various brain frequency patterns, for example those that characterize slumber.

This also has the possibility of providing a regressor for future analyses. For example, if rats do fall asleep in the scanner we can exclude (or differentially analyze) those periods of time when the animal is asleep by recording EEG during the fMRI scan.

In addition to the data presented in this thesis, we have conducted several experiments using the unanesthetized paralyzed rat preparation to collect resting state fMRI data. Resting state activity is currently treated as something of a “black box” that can be used to differentiate between different conditions. However, the true origin of the resting state signals are not understood. This represents a profound shortcoming in the field, one which we aim to utilize our new experimental approach to overcome. These studies are important not only for basic science, but also for interpretation of results from all translational and putative diagnostic resting state experiments. For example, if we discover a difference between control population A and experimental condition B in brain region X, it is currently common to assume that the defect or difference is inherent to region X. However, it could alternatively be the observable phenotype of a difference in brain region Y that projects to X, or even external sensory system Z that projects to Y. We are currently working to differentiate between these possibilities using the rat’s somatosensory system.

Contrast agent conjugates

As mentioned above, we developed paramagnetic muscimol (ParaMus) as a proof of concept that one could conjugate a contrast agent to a pharmacologically active chemical

commonly used in neurobiology studies without affecting that agent's pharmacological activity. We hope that this technique can be expanded to other agents of interest, ultimately creating a library of such agents ideal for use in fMRI experiments.

With regard to ParaMus itself, we hope that it can replace muscimol or fluorescent muscimol in studies that use MRI techniques. Notably, the inhibitory effects of ParaMus are reversible on the timescale of hours (or perhaps days for full tissue clearance). This makes ParaMus especially useful when it comes to studies of more individually valuable organisms for which post-mortem brain sectioning to determine the spread of the injection is not feasible. We propose a use case for monkeys in particular.

Towards real-time behavioral experiments during fMRI

Our unanesthetized, paralyzed preparation allows for the animals undergoing fMRI to be awake and thereby preserves applicability to the awake brain. However, the animals are in fact paralyzed and thus cannot perform standard behavioral tasks.

One way to circumvent this issue is to make use of biofeedback techniques. It has been demonstrated that humans are capable of deliberately altering the activity of brain regions or even individual neurons. For example, if the activity of a brain region (measured using fMRI in real-time) is represented by a red ball on a computer screen, subjects can learn to keep the red ball "in the air." In other words, they can learn to deliberately increase activity in that brain region. This same principle applies in rodents, as one can train rats to manipulate the activity of individual neurons when that activity is recorded using electrophysiology.

It is unknown at this time if BOLD fMRI-based biofeedback is possible in rodents, and testing this is the next major step in this project. In order to reinforce behaviors, a positive

stimulus is typically used. Since these animals will be paralyzed and in the MRI machine, we will use electrical stimulation of the MFB as the reward. We will start by monitoring activity in the chosen brain region and rewarding the animal anytime the signal exceeds some threshold value (relative to the average signal in that region). As the animal learns the task, we will increase the threshold until we fail to see further improvements in performance. Training the animal to modulate their own brain activity may take some number of days.

However, there are a number of confounds that may make such training impossible or infeasible. One primary limitation is the speed at which scans can be acquired. We typically collect functional scans every two seconds, which means there is up to a two-second delay between when the animal performs the action (i.e. elevates their brain activity in the region) and receives a reward for that action. Another confound is that the BOLD signal in the region may remain elevated, and it may be difficult to train animals to wait before repeating the action.

If training rats in BOLD biofeedback proves intractable, we will switch to using electrophysiological signals as the readout. As mentioned previously, it has already been demonstrated that rats can control the activity of neurons when that activity is measured by electrophysiology. Given the superior temporal resolution of EEG, this removes the temporal confounds mentioned above.

Once we have completed a proof-of-concept biofeedback training session, we can progress to performing more in-depth experiments. Ultimately, we hope to have animals performing more complex, decision-making tasks in the scanner by altering their brain activity in one of several regions.